BRIDGING ENVIRONMENTAL MAGNETISM WITH BIOGEOPHYSICS TO STUDY BIOGEOCHEMICAL PROCESSES OF TODAY

EDITED BY: Luigi Jovane, Andrea Teixeira Ustra, Dimitrios Ntarlagiannis and Leonardo Sagnotti

PUBLISHED IN: Frontiers in Earth Science

frontiers Research Topics

frontiers

ISSN 1664-8714
ISBN 978-2-88971-529-9
DOI 10.3389/978-2-88971-529-9

About Frontiers

Frontiers is more than just an open-access publisher of scholarly articles: it is a pioneering approach to the world of academia, radically improving the way scholarly research is managed. The grand vision of Frontiers is a world where all people have an equal opportunity to seek, share and generate knowledge. Frontiers provides immediate and permanent online open access to all its publications, but this alone is not enough to realize our grand goals.

Frontiers Journal Series

The Frontiers Journal Series is a multi-tier and interdisciplinary set of open-access, online journals, promising a paradigm shift from the current review, selection and dissemination processes in academic publishing. All Frontiers journals are driven by researchers for researchers; therefore, they constitute a service to the scholarly community. At the same time, the Frontiers Journal Series operates on a revolutionary invention, the tiered publishing system, initially addressing specific communities of scholars, and gradually climbing up to broader public understanding, thus serving the interests of the lay society, too.

Dedication to Quality

Each Frontiers article is a landmark of the highest quality, thanks to genuinely collaborative interactions between authors and review editors, who include some of the world's best academicians. Research must be certified by peers before entering a stream of knowledge that may eventually reach the public - and shape society; therefore, Frontiers only applies the most rigorous and unbiased reviews.
Frontiers revolutionizes research publishing by freely delivering the most outstanding research, evaluated with no bias from both the academic and social point of view. By applying the most advanced information technologies, Frontiers is catapulting scholarly publishing into a new generation.

What are Frontiers Research Topics?

Frontiers Research Topics are very popular trademarks of the Frontiers Journals Series: they are collections of at least ten articles, all centered on a particular subject. With their unique mix of varied contributions from Original Research to Review Articles, Frontiers Research Topics unify the most influential researchers, the latest key findings and historical advances in a hot research area! Find out more on how to host your own Frontiers Research Topic or contribute to one as an author by contacting the Frontiers Editorial Office: frontiersin.org/about/contact

BRIDGING ENVIRONMENTAL MAGNETISM WITH BIOGEOPHYSICS TO STUDY BIOGEOCHEMICAL PROCESSES OF TODAY

Topic Editors:
Luigi Jovane, University of São Paulo, Brazil
Andrea Teixeira Ustra, University of São Paulo, Brazil
Dimitrios Ntarlagiannis, Rutgers University, Newark, United States
Leonardo Sagnotti, Istituto Nazionale di Geofisica e Vulcanologia (INGV), Italy

Cover Image credit: Topic Editor Dr. Andrea Teixeira Ustra

Citation: Jovane, L., Ustra, A. T., Ntarlagiannis, D., Sagnotti, L., eds. (2021). Bridging Environmental Magnetism with Biogeophysics to Study Biogeochemical Processes of Today. Lausanne: Frontiers Media SA.
doi: 10.3389/978-2-88971-529-9

Table of Contents

frontiers in Earth Science

EDITORIAL
published: 07 September 2021
doi: 10.3389/feart.2021.757171

Editorial: Bridging Environmental Magnetism With Biogeophysics to Study Biogeochemical Processes of Today

Andrea Teixeira Ustra[1]*, *Dimitrios Ntarlagiannis*[2], *Leonardo Sagnotti*[3] and *Luigi Jovane*[1]

[1]Department of Geophysics, University of São Paulo, São Paulo, Brazil, [2]Department of Earth and Environmental Sciences, Rutgers University, Newark, NJ, United States, [3]Istituto Nazionale di Geofisica e Vulcanologia (INGV), Rome, Italy

Keywords: magnetic properities, biogeophysics, biogeochemical processes, environment, environmental magnetism

Editorial on the Research Topic

Bridging Environmental Magnetism With Biogeophysics to Study Biogeochemical Processes of Today

Since the first studies on biogeophysics in the early 2000s our understanding of how biogeochemical processes affect geophysical signatures has significantly improved. This interdisciplinary field now incorporates and integrates environmental and rock magnetism with traditional biological and geochemical methods to interpret geophysical signatures in highly dynamic environments (e.g., biogeochemical hotspots, contamination plumes). Environmental magnetism, in particular, can trace environmental changes by identifying magnetic mineral transformations induced from several biogeochemical processes. This Special Issue includes papers that present applications of environmental and rock magnetism in biogeophysics and discuss their impact on Earth Sciences.

(Bio) geochemical processes are often investigated with environmental magnetism methods in sediments and soils, aiming at identifying changes in the magnetic grain size distribution and stability. For example, microbial magnetite lies in the superparamagnetic (SP) to stable single domain (SSD) size range and variations in the size distribution can trace microbial activities. Ultrafine (SP) magnetic particles in human or animal tissues are also a subject of growing research interest, especially for their environmental significance, and the potential for medical applications. Fine magnetic particles are often observed in the anthropogenic fraction of atmospheric particulate matter, associated with toxic heavy metals, and may be a potential hazard for human health. Information on magnetic grain size distribution is of great value for all these applications.

Hirt and Liu synthesized mixtures of SP and SSD magnetite aiming to estimate their relative contribution in a variety of geological, biological and synthetic samples. The authors showed that both the Day-Dunlop plot and principal component analysis (PCA) analysis of first order reversal curves (FORC) measurements are effective methodologies to detect and quantify changes in the relative proportion of magnetic particles in the SP - SDD state in natural materials and in synthesized particles.

Jaqueto et al. explore the variations of magnetic mineralogy throughout different biomes in South America using a large speleothem rock magnetic database. The authors compare magnetic signals from speleothems, the soil above the cave and the host carbonate rocks to constrain the source and paths of magnetic minerals inside karst systems under different climatic conditions. They recognize that ultrafine ferrimagnetic minerals are the dominant magnetic phase in the speleothems that were studied, with a

OPEN ACCESS

Edited and reviewed by:
Kenneth Philip Kodama, Lehigh University, United States

***Correspondence:**
Andrea Teixeira Ustra
andrea.ustra@iag.usp.br

Specialty section:
This article was submitted to Geomagnetism and Paleomagnetism, a section of the journal Frontiers in Earth Science

Received: *11 August 2021*
Accepted: *19 August 2021*
Published: *07 September 2021*

Citation:
Ustra AT, Ntarlagiannis D, Sagnotti L and Jovane L (2021) Editorial: Bridging Environmental Magnetism With Biogeophysics to Study Biogeochemical Processes of Today. Front. Earth Sci. 9:757171. doi: 10.3389/feart.2021.757171

strong correlation between different concentration-dependent magnetic parameters, and that biomes play an important role in the definition of the magnetic content in speleothems.

In a much more dynamic scenario of ongoing hydrocarbon natural degradation, Beaver et al. investigate the microbial community contribution to the observed magnetic susceptibility changes at the National Crude Oil Spill Research Site in Bemidji, Minnesota. The multi-year analysis represents a rich record of microbiology and magnetic changes in hydrocarbon contaminated sediments undergoing biodegradation. The authors show that the highest magnetic susceptibility values were measured in the free-phase petroleum zone, where a methanogenic community was predominant, and not in the overlying iron-reducing zone. They hypothesized that this magnetic signature is evidence of the metabolic potential of methanogens to switch their metabolism from methanogenesis to iron reduction with concomitant magnetite precipitation.

Transformations of iron bearing minerals in a trapped gas pocket formed in Quaternary organic sediments is explored by Ustra et al., by tracking specific mineral changes that can be associated to biogeochemical processes. Their investigation is focused on changes regarding the magnetic carrier mineralogy, abundance, and grain size. In addition to classic techniques used in environmental magnetism, the authors utilize quantitative interpretation techniques to characterize the SP mineral content - in terms of variations in volume and concentration - along a cored section that intercepts a methane pocket trapped within organic-rich sediments. The authors point out that the association between iron-reducing bacteria and SP minerals in a region where both iron reduction and methane accumulation occur could reveal a direct interspecies electron transfer (DIET) scheme.

This Special Issue stems from an engaging session on the topic of biogeophysics and environmental magnetism during American Geophysical Union's Fall Meeting in 2019.

AUTHOR CONTRIBUTIONS

AU was a guest associate editor of the Research Topic and wrote the editorial text. DN was a guest associate editor of the Research Topic and edited the text. LS was a guest associate editor and acted as editor for two papers in the Research Topic and edited the text. LJ is an associate editor for the Geomagnetism and Paleomagnetism section and edited the text.

Conflict of Interest: The authors declare that the research was conducted in the absence of any commercial or financial relationships that could be construed as a potential conflict of interest.

The handling Editor declared a past co-authorship with one of the authors LJ.

frontiers in Earth Science

ORIGINAL RESEARCH
published: 16 February 2021
doi: 10.3389/feart.2020.586913

Estimating the Relative Concentration of Superparamagnetic and Stable Single Domain Particles in Geological, Biological, and Synthetic Materials

Ann M. Hirt[1]* *and Pengfei Liu*[1,2]

[1]Institute of Geophysics, ETH Zürich, Zürich, Switzerland, [2]State Key Laboratory of Lunar and Planetary Sciences, Macau University of Science and Technology, Macau, China

Obtaining an estimate of the relative proportion of superparamagnetic (SP) to stable single-domain (SSD) particle sizes in a material can be useful in evaluating environmental conditions in natural materials, or in understanding the homogeneity of particle size and the degree of agglomeration in synthesized particles. Frequency dependent magnetic susceptibility is one of the most common methods used to identify SP particles in a material. The ability to detect SP particles, however, will be dependent on the field frequencies that can be applied. This study is concerned with evaluating three methods to estimate the SP content in a mixture of SSD and SP magnetite. We examine the use of the Day-Dunlop plot, first-order reversal curves (FORC) and principal component analysis (PCA), and the relationship between the reversible and irreversible magnetization as methods to evaluate qualitatively the relative contributions of SSD and SP magnetite in a material. Two series of mixtures of coated nanoparticles with a mean diameter of 20 and 11 nm are used as the SP end member and magnetosomes or intact magnetotactic bacterium of *Magnetospirillum gryphiswaldense* as the SSD end member. The Day-Dunlop plot tracks the progressive change in hysteresis properties with growing SP concentration. PCA of FORC data is sensitive in detecting differences in the SP component, when the SP particle size are not too small; otherwise the ratio between the reversible and irreversible magnetization can better assess differences. The results from the series are used to evaluate the relative SP content in three further sets of samples: biological tissue, synthetic nanoparticles, and samples from natural environments, to assess the strengths and weaknesses in each approach.

Keywords: magnetite, superparamagnetic-single domain mixtures, Day-Dunlop plot, FORC- PCA analysis, reversible-irreversible magnetization

OPEN ACCESS

Edited by:
Leonardo Sagnotti, Istituto Nazionale di Geofisica e Vulcanologia (INGV), Italy

Reviewed by:
David Heslop, Australian National University, Australia
Ramom Egli, Central Institution for Meteorology and Geodynamics (ZAMG), Austria

***Correspondence:**
Ann M. Hirt
ann.hirt@erdw.ethz.ch

Specialty section:
This article was submitted to Geomagnetism and Paleomagnetism, a section of the journal Frontiers in Earth Science

Received: *24 July 2020*
Accepted: *24 December 2020*
Published: *16 February 2021*

Citation:
Hirt AM and Liu P (2021) Estimating the Relative Concentration of Superparamagnetic and Stable Single Domain Particles in Geological, Biological, and Synthetic Materials. Front. Earth Sci. 8:586913. doi: 10.3389/feart.2020.586913

INTRODUCTION

Hysteresis properties are often the most common parameters that are used for assessing composition, domain state, or particles size of ferromagnetic minerals in geological materials (Day et al., 1977; Dekkers, 1988; Heider, 1988; Geiss et al., 1996; Heider et al., 1996; Dunlop, 2002; Roberts et al., 2018), biological samples (Moskowitz et al., 1993; Brem et al., 2006), and synthesized magnetic particles (Sotiriou et al., 2011; Widdrat et al., 2014; Starsich et al., 2016; Crippa et al., 2017). Geological materials, in particular, can contain varying proportions of different ferromagnetic minerals, or in

the case of only a single magnetic phase, a spectrum of particle sizes. Further aggregation of synthetic nanoparticles can also produce a spectrum of effective or apparent particle sizes (Hirt et al., 2017).

In this study we are interested specifically in mixtures of stable single domain (SSD) and superparamagnetic (SP) magnetite. Mixtures of SSD and SP magnetite are of particular interest in environmental, biological and material studies. The ability to estimate the size distribution of magnetite can be important in environmental studies, because it is indicative of geochemical processes that can lead to authigenic growth of new magnetite from a precursor phase or chemical reduction of an existing magnetite. Biological magnetite in bacteria often consists of a range of particle sizes in the SP to SSD range (Faivre and Schuler, 2008; Katzmann et al., 2013; Jacob and Suthindhiran, 2016), and understanding variations in size distribution can provide insight into the provenance or fate after the bacteria die and magnetosomes are deposited in a sediment. A further biological application is associated with magnetite nanoparticles that are either introduced into human or animal tissue through inhalation (Maher et al., 2016; Calderon-Garciduenas et al., 2019), or through biochemical processes associated with an imbalance of iron in the body (Dobson, 2004; Beyhum et al., 2005; Hosking et al., 2018). In these cases the particle size of iron oxides may be important in assessing potential health hazards. Information on particle size spectrum is particularly important in the application of magnetic nanoparticles for medical therapeutics, because the magnetic properties need to be tailored to provide the best response for a specific application. For example, in hyperthermia treatment of cancer cells, the heating response of magnetic nanoparticles will be related to their ability to respond to an alternating field to generate heat (Crippa et al., 2017; Starsich et al., 2018).

Different magnetic methods are available to assess whether a material contains SP ferromagnetic particles. The most definitive methods involve measuring induced magnetization, particularly AC susceptibility, as a function of temperature, which indicates at what temperature the particles undergo blocking. If, however, one is limited to instruments that only measure at room temperature, then one of the most common methods, which is used to indicate the presence of SP ferromagnetic particles, is frequency dependent susceptibility. The method became popular in environmental magnetic studies with the introduction of the Bartington Instruments MS2 susceptibility meter, which offers application of two different AC fields, i.e., 470 and 4,700 Hz (Dearing et al., 1996). Later AGICO introduced a susceptibility bridge that offered measurement in three different frequencies, 976, 3,904, and 15,606 Hz. Hrouda (2011) has provided a detailed discussion of the many factors that will influence whether a significant frequency dependence in susceptibility can be measured. This includes the strength of the contribution from diamagnetic, paramagnetic and even multi-domain (MD) ferrimagnetic fractions to the bulk susceptibility, and the particle size distribution of the SP fraction. Anisotropy factors and saturation magnetization, however, can also play a role in modeling the degree of frequency dependence as a function of particle size. Hrouda (2011) demonstrates that in the case of magnetite or maghaemite only a relatively narrow range of particle sizes contribute to the frequency dependent susceptibility, i.e., only magnetite particles with a diameter between 16.05–16.73 nm when using F1 (976 Hz) and F3 (15,616 Hz) on an Agico susceptibility bridge, or 16.64–17.68 nm when using the Bartington susceptibility meter with frequencies of 470–4,700 Hz. This means that frequency dependent susceptibility may not detect a significant portion of SP particles, if the particle diameters lie outside these ranges.

Other methods to detect the presence of SP particles include measurement of hysteresis loops or first-order reversal curves. Tauxe et al. (1996) simulated hysteresis loops for mixtures of SSD and SP magnetite, using a Langevin function. They showed that models predict wasp-waisted hysteresis curves and pot-bellied loops in such mixtures depending on their relative contributions to magnetization. Dunlop (2002) illustrated how hysteresis parameters will be influenced by mixtures of SP magnetite of different sizes and SSD magnetite. Later studies demonstrated that the thermal relaxation of the SP particles was not considered in this study and that SSD-SP mixtures would lead to mixing curves that have lower than predicted coercivity ratios (Lanci and Kent, 2003; Heslop, 2005). Two studies on artificial mixtures of SSD and SP magnetite illustrated that the ratio between saturation remanent magnetization and saturation magnetization (M_{RS}/M_S) decreases significantly with the addition of SP material and coercivity ratios lower than predicted by Dunlop (2002), which would be expected because SP particles do not carry a remanent magnetization (Dunlop and Carter-Stiglitz, 2006; Kumari et al., 2015). In the past several years, Lascu et al. (2015) and later Harrison et al. (2018) introduced a method to perform principal component analysis (PCA) on first order reversal curves (FORC) data (FORCem) to unravel mixtures of phases with contrasting magnetic properties, including domain state, and/or composition. The method was applied to different combinations of synthetic binary mixtures of multi-domain (MD), vortex state (V), SSD and SP magnetite, or SSD and SP greigite. Liu et al. (2019) demonstrated how PCA of FORC data could be used to unravel mixtures of SSD magnetite and hematite.

We evaluate methods that can be used to obtain a qualitative estimate for the concentration of SP and SSD particles of magnetite in a mixed system at room temperature. For this purpose, we focus on the Day-Dunlop plot, FORC-PCA, and the relative contributions of the reversible and irreversible magnetizations (Kumari et al., 2014). Two SSD-SP mixing series are compared, in which the SP component of one series has 20 nm average particle size and the second series has ca. 11 nm. Results from three further data sets are compared to these mixtures series. They include geological samples, brain tissue samples, and synthetic SP magnetite. This evaluation should provide insight into which methods are most suitable for discerning relative concentration of SP in mixtures with SSD ferrimagnetic phases. We further highlight the limitations of the methods, particularly when analyzing natural samples that may not meet the assumptions of non-interacting, pure magnetite.

MATERIALS AND METHODS

SSD-SP Sample Mixtures

The SSD end member of the first mixing series uses the magnetosomes from *M. gryphiswaldense*, which have been described by Lohsse et al. (2016). The magnetosomes are covered with a lipid shell, which prevents oxidation, and have an average particle size of 37.8 ± 11.0 nm. The SP end member is a synthetically produced magnetite with an average particle size of 20.2 ± 1.6 nm that was coated with PVA-catechol (Crippa et al., 2019). When preparing the SP end member, the colloid sample was first placed into an ultrasound cleaner for 1 min to distribute the particles evenly in the water base before pipetting. For the pure SP end member sample, 20 µl was pipetted onto a small piece of sterile cotton wool within a quartz glass cylinder with 5 mm diameter (3 mm inner diameter) and ca. 10 mm length; one end was sealed with non-magnetic epoxy. The sample was left to dry 24 h in a refrigerator before it was measured. The SSD end member was pipetted from the magnetosome colloid into a quartz glass cylinder with a 5 mm diameter (3 mm inner diameter) and 11 mm length. The sample holder was placed on a magnet and excess water was pipetted from the sample. This process was repeated several times before the samples were left for 24 h in a refrigerator. The starting mass of the SSD end member was 0.46 mg. This SSD sample was then used for the mixing series. Initially one drop of SP colloid, which contains a 0.047 mg of the pure SP particles, was pipetted into the holder. N.B., the mass includes the PVA coating, but its contribution to the total mass will be very small. A small piece of sterile cotton wool was added to adsorb the liquid and fix the particles before measurement. Subsequently nine further increments of SP magnetite were added to the holder, following the same procedure. This gave a total of 10 mixtures with the SP contribution varying between 9 and 91 wt%, in addition to the 0 and 100% end members.

The second mixing series consists of samples that were used in a study of SSD-SP mixtures with respect to the Day-Dunlop plot (Kumari et al., 2015). This study reported on the change in M_{RS}/M_S against the ratio of remanent coercivity to coercivity (B_{CR}/B_C) with an increase in the concentration of the SP end member. The SSD end member is the same as in the first series, *M. gryphiswaldense*, except that the magnetosomes are still in chain configuration within the bacteria. The average size of the magnetosomes is 35 ± 10 nm. The SP end member is a ferrofluid, FluidMAG-D (Chemicell GmbH, Art. No. 4101-1 and 4101-5). The sample is made up of small crystallites on the order of 6 nm that form clusters on the order of 10–12 nm. The end members were pipetted into quartz glass holder with a small amount of sterile cotton wool, as described above. Note that the total mass was not recorded. A small amount of the SP samples was added incrementally to the SSD end member, and the sample was left to dry in a refrigerator after each addition for at least 5 h.

Other Samples

A selection of samples was chosen, in which magnetite/maghaemite are the only magnetic phases, to compare with the results from the synthetic mixing series, in order to have a qualitative evaluation of the content of SP magnetite. The samples can be divided into three groups. The first set consists of geological samples and include a sample from the Tiva Canyon Tuff (55 m above base), which is predominantly SP (Till et al., 2011), and three samples from lakes. The lake samples include a sample from the Schwarzsee ob Solden (SOS-P1-059) (Ilyashuk et al., 2011), one sample from Lake Merlingsdals from Southern Norway (OP18) (Storen et al., 2016), and a sediment sample from Lake Baldegg, Switzerland (BA10-05), which is above the redox boundary (Egli, 2003; Egli, 2004a; Egli, 2004b). The second set of samples are biological tissues. Samples GS, HH, HM, SC, and LH are human brain tissue, which were resected from humans who suffer from epilepsy. GS and HH are from the hippocampus, HA and HM are from meningioma (Brem, 2006; Brem et al., 2006), SC is from an oligodendroglioma, and LH from a glioblastoma (Blaser, 2008). The third set of samples are magnetic nanoparticles. AF23 was fabricated by A. Finke and FCA35 was synthesized by F. Crippa at the Adolphe Merkel Institute, Fribourg, Switzerland (Crippa et al., 2019). Sample XL is from FeraSpinXL, which is the large particle fraction of FeraSpin R (NanoPet, Berlin, Germany) (Hirt et al., 2017). VR4 and VR 8 are mesocrystals of magnetite (Reichel et al., 2017). We note that the condition of non-interaction is not met in all of these samples, and the effect that this has will be discussed.

Magnetic Methods

Magnetic susceptibility was measured with an AGICO MFK-1A susceptibility bridge in two frequencies, 976 and 15,616 Hz to determine the frequency dependent susceptibility. The percentage of frequency dependent susceptibility is defined as:

$$\chi_{FD} = \frac{\chi_{976\ Hz} - \chi_{15616\ Hz}}{\chi_{976\ Hz}}\ 100\%.$$

A Princeton Measurements Corporation (PMC) vibrating sample magnetometer (VSM), with a sensitivity level of 4×10^{-9} Am^2 (standard deviation) was used for measurement of magnetization as a function of field (hysteresis loops) and FORC analysis. For the SSD-SP mixing series the magnetization was measured using 100 ms averaging time to obtain M_S, M_{RS}, and B_C. A multi-segment measurement scheme was used for field application with 0.5 mT steps in fields ≤ ±98, 2 mT between ±100 to ±200 and 5 mT in fields between ±205 to ±1,000 mT. The magnetization curve was measured for all holders with any fixing material, such as sterile cotton, before adding the sample, in order to remove its contribution to the total magnetization. All holder signals were diamagnetic. Back-field demagnetization was used to obtain B_{CR}. Samples were first magnetized in 1,000 mT in one direction so that the samples acquire an isothermal remanent magnetization (IRM) and then incrementally remagnetized in the opposite direction, using 6 mT field increment in the first series and a 10 mT increment in the second series; 100 ms averaging time was employed in both series. FORC measurements of both mixing series used a

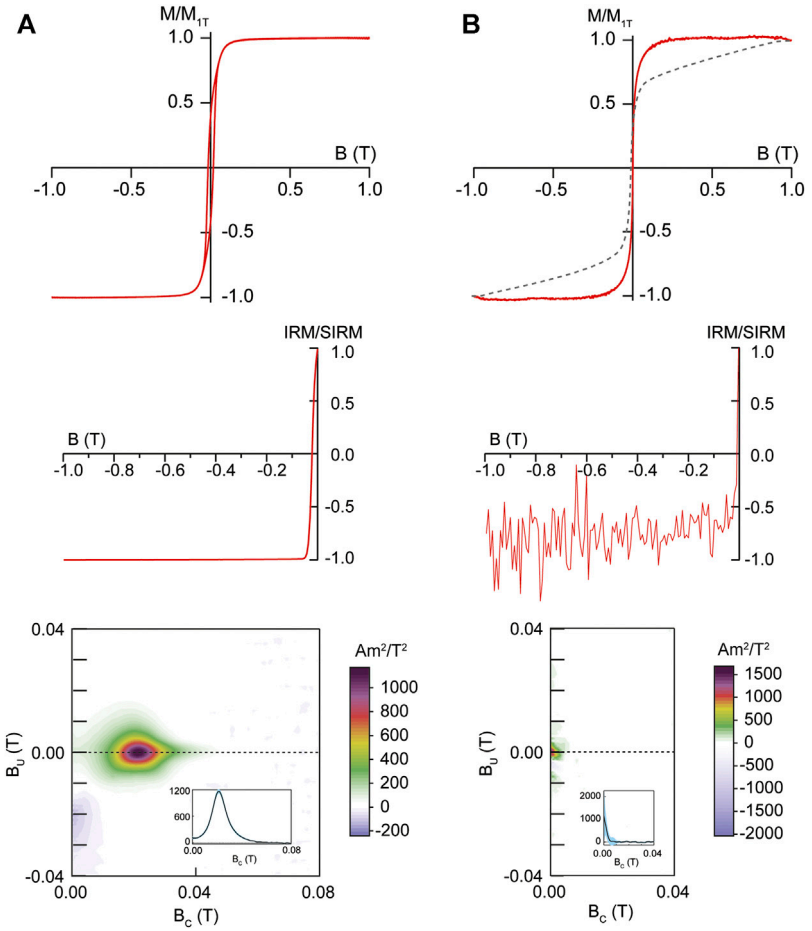

FIGURE 1 | Hysteresis loop **(top)**, back-field demagnetization **(middle)**, and FORC distribution with an inset illustrating the coercivity spectrum **(bottom)** for **(A)** SD magnetosomes from *M. gryphiswaldense* (N.B., no correction for high-field slope is required); and **(B)** the SP synthetic magnetite (20 nm). Note dotted line shows hysteresis loop before correcting for high-field slope.

saturation field of 1,000 mT. For the first series a measurement increment of 1.54 mT, B_{Cmax} of 100 mT, B_U of 80 mT was applied and 190 individual FORCs were measured. In the second series, a measurement increment of 1.54 mT, B_{Cmax} of 100 mT, B_U of 60 mT was applied and 180 individual FORCs were measured. The magnetic properties from the hysteresis and FORC measurements are summarized in **Supplementary Tables S1, S2** for the two SSD-SP mixing series. The parameters for the FORC measurements are variable for the geological, biological tissue, and material samples, because these samples were measured over the past 15 years; the parameters are summarized in **Supplementary Tables S3–S5** together with their magnetic properties. All measurements were made at the Laboratory of Natural Magnetism, ETH Zurich, Switzerland. FORC data were processed using FORCinel (v. 3.03) (Harrison and Feinberg, 2008; Egli, 2013; Lascu et al., 2015; Harrison et al., 2018) and principal component analysis (PCA) of the FORC data were made with FORCinel (v3.05) (Harrison et al., 2018). A smoothing factor (SF) of four and six are used for the first SSD-SP mixing series to examine the effect of the smoothing factor on the PCA scores. Note that this SF is for the smoothing of the central ridge and vertical ridge; a higher smoothing factor of seven was employed for the horizontal and vertical smoothing. In the second series, SF = 4 is used to compare with the first series. A SF = 6 is used for the other sample sets to accommodate the SP end member, and in the case of the biological samples, the very weak magnetization. These are then compared to the first mixing series that was processed with SF = 6. The projection of the PCA scores of these other data sets onto Series 1 was performed with MatLab, using the matrices that were calculated for each set of samples with the FORCem package in FORCinel, with a PCA grid of 1.54 mT (**Supplementary Data Sheet S1.1**). A MatLab code for processing the FORC data, UNIFORC (Winklhofer et al., 2008), was used to obtain the reversible and irreversible contribution to the magnetic hysteresis. This can be expressed as a ratio in the peak in $\partial M_{rev}/\partial B$ to $\partial M_{irrev}/\partial B$, which we refer to as M_{rev}/M_{irrev} in the following.

RESULTS

SSD-SP End Members

The SSD and SP end members for both series had $\chi_{FD} < 0.3\%$. This would be expected for the SSD end members, but it indicates that the two SP end members are in a size range which would not be detected.

Other magnetic properties of the end members of Series 1 are summarized in **Figure 1**. The hysteresis loop for the SSD end member is open with $B_C = 16.3$ mT and the magnetization reaching saturation by 220 mT (**Figure 1A**). M_{RS}/M_S is 0.40. The isothermal remanent magnetization (IRM) is saturated by 150 mT and $B_{CR} = 21$ mT, which gives $B_{CR}/B_C = 1.30$. The values of M_{RS}/M_S and B_{CR}/B_C are close to expected SSD behaviour, which are $M_{RS}/M_S = 0.5$ and $B_{CR}/B_C = 1.5$ (Dunlop, 2002), and the slight deviation may be due to the presence of some magnetosomes that are in the SP size range or magnetostatic interaction between magnetosomes, which would lower the magnetization ratio (Muxworthy et al., 2003). The FORC diagram shows a narrow, slightly elongated coercivity distribution with a peak around 20.3 mT and a half-width of the interaction field, $B_{U1/2} = 4.7$ mT (**Figure 1A**). The narrow distribution in interaction field indicates that magnetic interaction between the magnetosomes is minimal. This is further supported by the pronounced negative region in the negative interaction fields at low coercivity (Newell, 2005).

The hysteresis loop of the SP end member is closed and not saturated at 1 T (**Figure 1B**). The lack of saturation is due to poorly crystalline Fe phases that are in the colloid solution We correct this component for the high-field slope which will lead to an overcorrection for M_S. The overcorrection should not be large, because of the 20 nm particle size and a measurement averaging time of 100 ms. A weak IRM is detectable, but it is relaxing on the scale of the measurement as seen by the positive slope of the acquired remanence in high fields. The FORC distribution is centered at the origin of the diagram with a slight positive shift along the interaction axis (**Figure 1B**), as predicted by Pike et al. (2001).

SSD-SP Mixing Series

Because the SP end member does not carry a remanent magnetization, M_{RS} is used to monitor that the magnetic properties of the SSD end member is not changing with each addition of the SP end member. M_{RS} remains relatively constant until the SP contribution reaches 83% in the first mixing series, and its contribution dominates the overall magnetic properties, i.e., wasp-waisting of the loop becomes prominent. In the second series M_{RS} remains relatively constant for all increments, although there is no direct control over the amount of the SP material in the sample (**Supplementary Figure S1**).

The hysteresis loops for the samples in Series 1 illustrate that the magnetization is saturated by 300 mT (**Supplementary Figure S2A**). A gradual increase in wasp-waisting is seen, starting with 19% SP component that remains up to 91% (**Supplementary Figure S3**). For Series 2 only the magnetization of the SSD end member (sample one) and sample two are saturated by 300 mT (**Supplementary Figure S2B**); the other samples of the series show an approach to saturation. This will lead to an overcorrection for M_S, but the effect is on the order of a few percent (Kumari et al., 2015). Obvious wasp-waisting is not seen in Series 2, but there is a narrowing of the loop with each addition of the SP end-member (**Supplementary Figure S4**). The change in magnetic properties of both series can be compared by the change in M_{RS}/M_S and B_{CR}/B_C (**Figure 2**). There is a steady decrease in the magnetization ratio and increase in the coercivity ratio in both series. Series 1 plots left of Series 2 because of the larger size of the SP end member. The SP end member of Series 1, has a lower coercivity ratio than the second series, because the 20 nm core size allows for the measurement of B_{CR} from the magnetization that has not completely relaxed when the field is removed during the FORC measurement. Note that both series show lower coercivity ratios, i.e., lie to the left, of the theoretical curves from Dunlop (2002).

FORC diagrams show the gradual shift of the FORC distribution toward the origin with an increasing contribution of the SP component in Series 1 (**Supplementary Figure S3**). This is best seen in the coercivity profile with the growth of the peak at the origin. It is also reflected by an increase in the contribution of reversible component of the total magnetization at the expense of the irreversible contribution. Analysing the FORC data with PCA

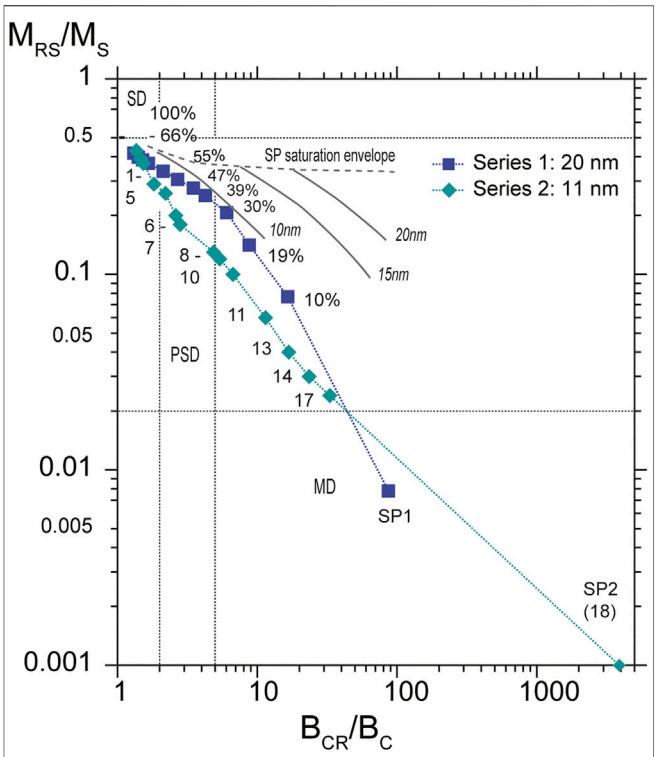

FIGURE 2 | Day-Dunlop plot for both mixing series, in which the percentage refers to the total the SD end member in terms of total weight for the mixture Series 1. Note: we take the hysteresis parameters from the FORC measurements so that we compare Series 1 with Series 2 (cf. **Supplementary Tables S1, S2**). Gray lines show the SSD-SP mixing lines for 10, 15, and 20 nm particles taken from Dunlop (2002).

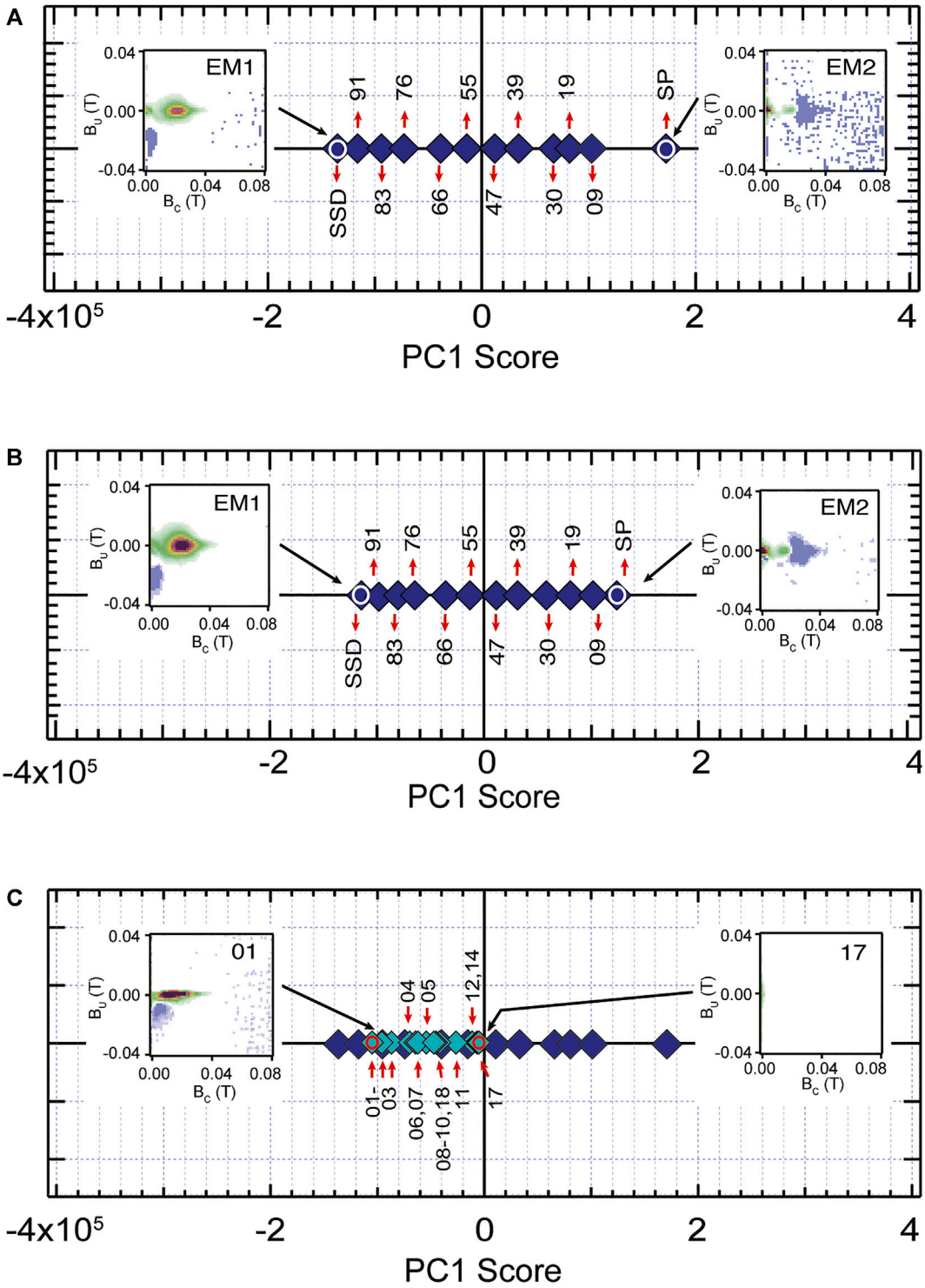

FIGURE 3 | Binary PCA analysis from FORC data for **(A)** Series 1 with SF = 4; and **(B)** Series 1 with SF = 6 with FORC diagrams for end members (white circles) **(C)** Series 2 projected onto Series 1 with SF = 4; note that the FORC diagrams illustrate the predicted FORCs from the FORCem program for the extreme samples in the MK series (red circles). PCA grid is 1.54 mT in all PCA plots. Numbers refer to percentage of SP particles in **(A)** and **(B)**, and sample number in **(C)**.

analysis using SF = 4, PC1 explains 85% of the variability, i.e., the relative concentration of the SSD and SP end members. The end members (EM) are clearly related to SSD (EM1) and SP (EM2) magnetite, and the PC1 score changes systematically with the relative change in the two end members (**Figure 3A**). The PCA approach reproduces the FORC diagram of SSD magnetite, but

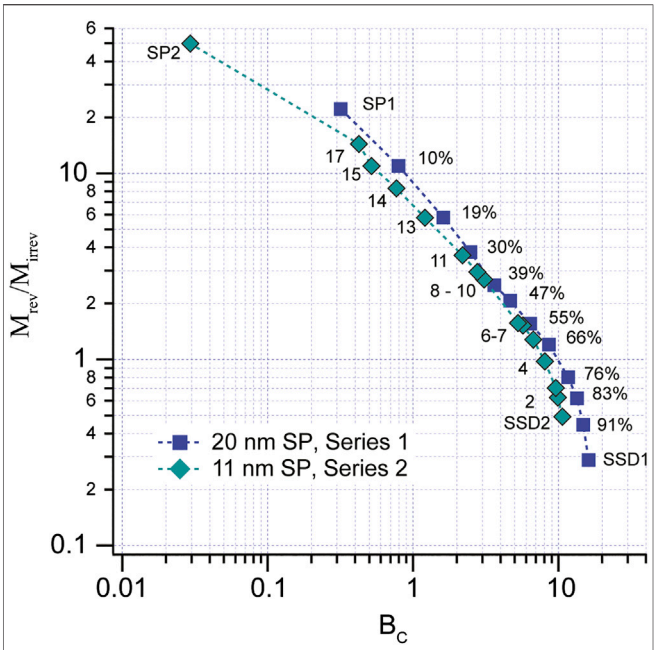

FIGURE 4 | Change in M_{rev}/M_{irrev} as a function of B_C for Series 1 and 2 illustrating the progression from the SSD end members to SP end members. Percentages refer to SP% in Series 1 and numbers refer to sample number in Series 2.

indicates a notable SP contribution, which is not as strongly expressed in the FORC diagrams (**Supplementary Figure S3A**). The FORC diagram for the SP end member also captures the main coercivity feature at the origin of the diagram, and shows the upward shift along the interaction field axis. The PCA analysis, however, also shows a very small SSD contribution (**Supplementary Table S6**). Using a higher smoothing factor leads to a narrower range in the PC1 score, which explains 92% of the variance. The PC1 score for the SP end member shifts closer to the sample with 91% SP-content (9% SSD concentration). The calculated FORC diagrams are similar to those described for SF = 4, but the SP contribution for EM1 and the SSD contribution to EM2 are more pronounced (**Figure 3B**; **Supplementary Table S6**).

Figure 3C shows the PC1 scores of the second series that are projected on the PC1 scores of the first series. There is a gradual shift in the PC1 score from the SSD end member to the SP end member of Series 2 (**Figure 3C**). The SSD end member has lies near an SSD contribution of ca. 86%, and the last SSD-SP sample, i.e., the sample with the highest SP component, lies close to the 50% SSD contribution of Series 1. The FORC diagram, which is calculated for the SSD end member, indicates a more prominent SP contribution than found in the measured FORC diagram (**Supplementary Figure S4A**). The PCA analysis, however, reproduces the FORC diagram for sample 17 (**Supplementary Figure S4N**). It is interesting that the SP end member of Series 2, shows a lower SP contribution than sample 17, which suggest that the PCA analysis cannot adequately resolve the contribution of these particles with faster relaxation time.

If we process the two sets of data together and use a PCA model that includes three end members, the third end member corresponds to a SSD assemblage, for the chains of magnetite. The second series shows a distinct separate progression in comparison to the first model (**Supplementary Figures S5A,B**). The calculated FORC diagram for the SSD end member of Series 2 (EM3) has a narrower distribution in interaction field (B_u), compared to Series 1. The calculated FORC for the SSD sample of Series 1, however, better resembles the measured FORC (cf., **Supplementary Figures S3A, S5A**).

The third method that we apply is to observe the change in M_{rev}/M_{irrev} as a function of B_C. If we assume that the SSD end member is made up of non-interacting, SSD magnetite and is controlled by shape anisotropy, then the irreversible contribution of magnetization should be 50% of the reversible contribution, and the ratio between the two would be 0.50 (Dunlop and Özdemir, 1997). For this reason the SP content should be reflected in the relative reversible contribution to magnetic hysteresis (Kumari et al., 2014). **Figure 4** illustrates the change in ratio of the reversible to irreversible magnetization (M_{rev}/M_{irrev}). The coercivity of the SSD end member in Series 2 is lower than Series 1, which leads to a slight shift in the two curves. M_{rev}/M_{irrev} is <0.5 for the SSD end member of Series 1, which indicates that the sample does not meet the assumptions completely. This point is considered further in the discussion. As the contribution

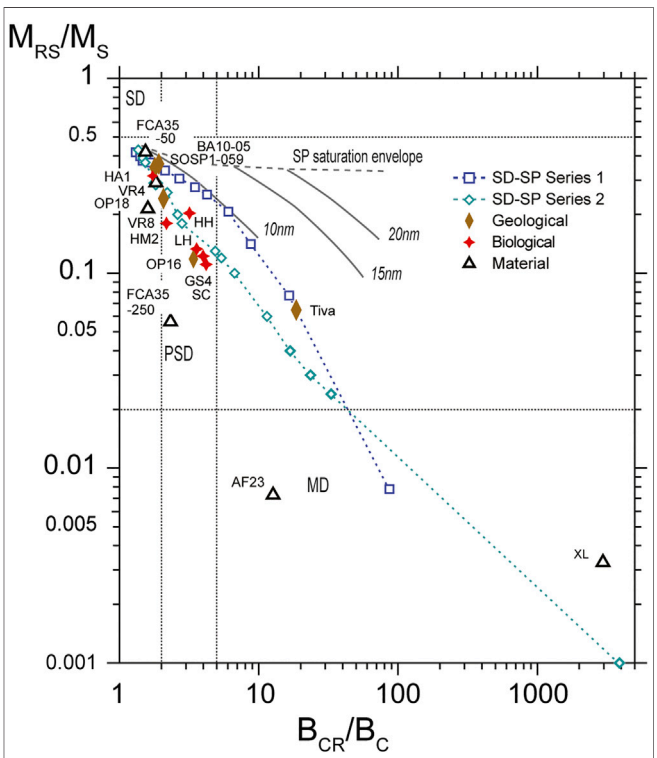

FIGURE 5 | Day-Dunlop plot showing the change in the magnetization and coercivity ratios for the geological, biological and material samples in relation to the SD-SP series.

of M_{rev} to the total magnetization increases, B_C decreases as would be expected from what is observed in the Day-Dunlop plot.

Geological, Biological, and Material Samples

In order to investigate how applicable these methods may be in relation to natural or synthetic samples for which there is no information on the relative amounts of SP and SSD magnetite, we examine three sets of samples that have magnetite as the sole, or in some cases dominant, ferromagnetic phase. The first set include geological samples, the second are brain or brain tumour tissue from humans, and the third are synthesized magnetite. Samples from the three sets show narrow hysteresis loops that saturate in low fields (**Supplementary Figures S6–S8**). No obvious wasp-waisting was noted in any of the samples. The geological and biological samples show a range of magnetization and coercivity ratios when viewed on a Day-Dunlop plot (**Figure 5**). The lacustrine sediment and most of the brain tissue have open hysteresis loops, except for LH and SC, which have very narrow loops, and Tiva Canyon Tuff appears closed (**Supplementary Figures S6, S7**). Most of the geological and biological samples align close to Series 2. The synthetic samples show closed loops in the case of XL, AF23 and FCA35-250, but open loops for VR4, VR8, and FCA35-50 (**Supplementary Figure S8**). On the Day-Dunlop plot the synthetic samples show more deviation with respect to either series.

The lacustrine sediments for SOSP1-059, OP18, and BA10-05 have FORC diagrams that have elongated, narrow FORC distributions (**Supplementary Figure S6**), similar to the FORC diagrams of magnetotactic bacteria (cf., **Supplementary Figures S3, S4**). OP18, however also shows a secondary feature between ca. 20 and 30 mT with a broad distribution in B_U. This feature is common for magnetotactic bacteria in which magnetosomes cluster, due to disintegration of chains once the bacteria die (Kind et al., 2011). The FORC diagrams of the biological samples are characterized by distributions that lie close to the origin, with a SSD-like distribution for HA1 to more SP-like FORC distributions for SC, and LH (**Supplementary Figure S7**). Sample HA and GS have broader distributions in B_U compared to other samples. The Wohlfarth ratio for these samples is approximately 0.30 ± 0.05 (Brem et al., 2006), which indicates that there is interaction between the particles. In the material samples, the FORC diagrams for samples XL, AF23, and FCA35-250 show a confined distribution at the origin with an upward shift, indicative of the SP behaviour (**Supplementary Figure S8**). Samples VR4 and VR8 also have FORC distributions that are also close to the origin, but show a broader coercivity distribution. FCA35-50 has a FORC distribution that is away from the origin, indicating that the particles are magnetically blocked (**Supplementary Figure S8**).

PCA analysis was carried out on each set of samples and the PCA scores of each set projected onto the PCA scores of Series 1, which was processed with SF = 6. For the geological sample, the lacustrine samples, in which magnetite is bacterial, have a PC1 score are close to the sample with a 76–83% SSD concentration when projected on Series 1 (**Figure 6A**). Only the sample from the Tiva Canyon Tuff shows a higher contribution (ca. 50%) from the SP end member. The biological samples show PC1 scores that are similar to each other, lying between ca. 74 and 80% concentration of the SSD EM (**Figure 6B**). HA1 shows the strongest SSD contribution and LH the lowest, although differences between the samples is small (**Figure 6B**). The material set of samples shows more of a spread in PC1 scores, compared to the other two sample sets. XL lies beyond the SP end member of Series 1, and FCA35-50 lies nearest to the SSD end member (**Figure 6C**). The other samples are clustered between the Series 1 samples with 45–66% SSD content. A comparison of FCA35-250 and FCA35-50 illustrates a significant shift that occurs at lower temperature as the magnetic particles have undergone blocking.

Plotting M_{rev}/M_{irrev} as a function B_C, shows that the geological set of samples follows the progression of Series 1 but is shifted toward higher B_C (**Figure 7**). The lacustrine samples cluster around the sample with 76% SSD concentration. The Tiva Canyon Tuff sample has a higher ratio that agrees with a higher concentration of SP magnetite. The biological samples lie close to Series 1 for the lowest values of M_{rev}/M_{irrev}, but then plot along the progression for the geological samples (**Figure 7**). M_{rev}/M_{irrev} falls below 0.5 for the two human brain samples that had Wohlfarth ratios around 0.3. Most of the material samples are also close to the progression found for Series 2, although with a shift to lower B_C. Only FCA35-50 is shifted to a higher coercivity.

DISCUSSION

The two sets of SSD-SP mixtures show similarities in their change in magnetic properties that would be expected with an addition of a second phase that is ferromagnetic, but which carries "no" remanent magnetization. The difference between the two series arises largely from the difference in the core size of the SP end member, with 20 nm in Series 1 and ca. 11 nm in Series 2. Considering that the hysteresis and FORC measurements were made using an averaging time of 100 ms, this would mean that the boundary between SP and SSD behaviour for non-interacting magnetite is around 23 nm. Note the longest averaging time that was used in the FORC measurements was 300 ms, which would shift the boundary slightly higher to around 24 nm.

The two SP end members do not show any frequency dependency with respect to the applied frequencies; therefore, χ_{FD} cannot be used to provide information on the concentration of SP particles. Our results highlight the limitations of using the methods due to the frequencies that are available in commercial instruments.

The hysteresis loops for Series 1 show wasp-waisting with the addition of the SP end member starting between 9 and 19% SP-content. Series 2, however, only shows a weak wasp-waisting by sample 10; what is notable, however, is a narrowing of the hysteresis loop. This difference reflects probably the more rapid relaxation of particles in Series 2. The Day-Dunlop plot is one of the most commonly employed methods to assess particle

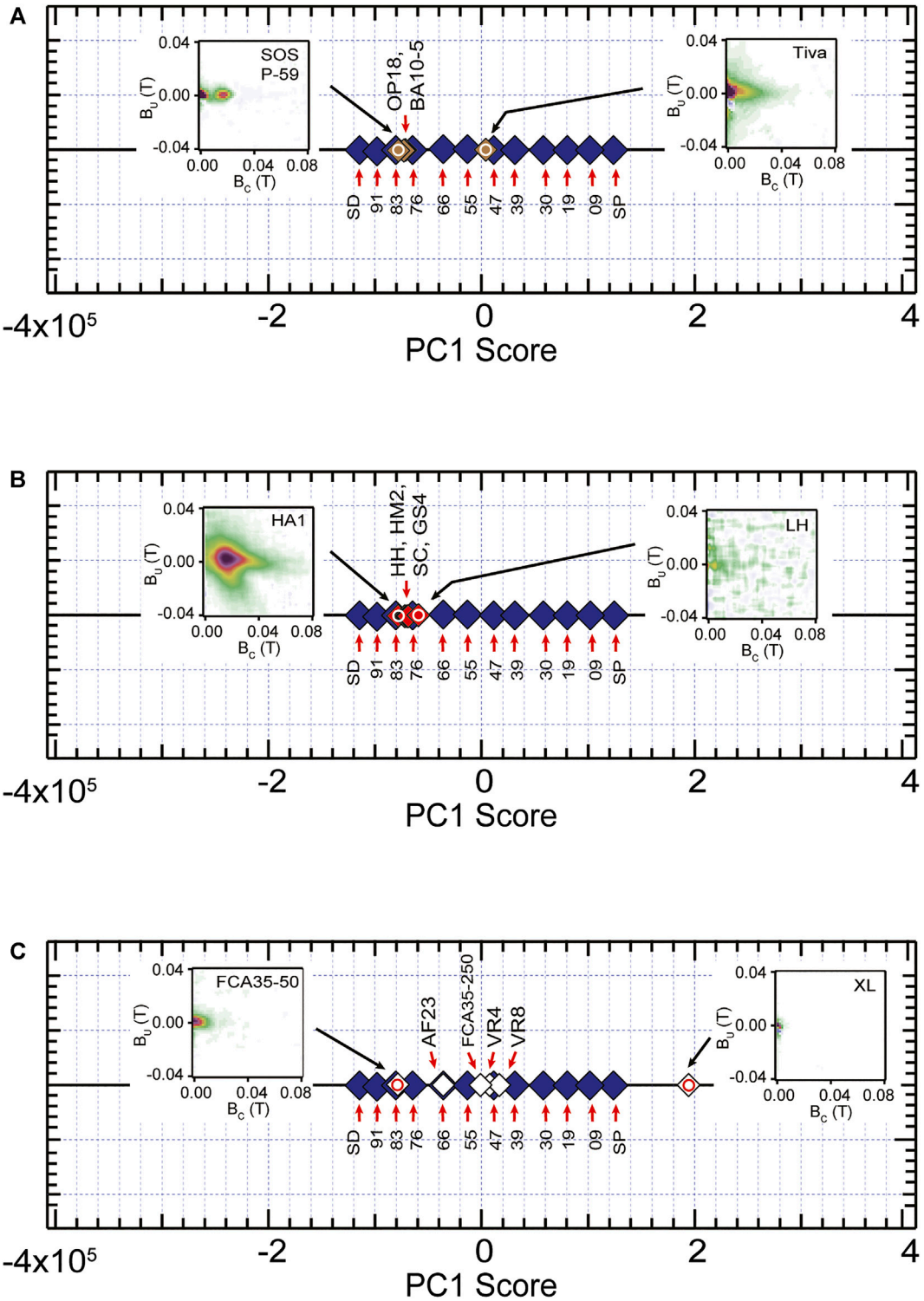

FIGURE 6 | Binary PCA of FORC data for: (**A**) the geological samples **(B)** biological samples, and **(C)** material samples projected onto Series 1; FORC diagrams illustrate the predicted FORCs from the FORCem program for the extreme samples of each sample group (circles). The PCA grid is 1.54 mT and SF = 6 for all samples.

size or domain state of magnetite, based on hysteresis parameters. There is a major concern, which is associated with using hysteresis properties, to estimate particles size. Day et al. (1977) noted that if magnetite particles are interacting, this will lower M_{RS}/M_S, B_C and B_{CR}. Muxworthy et al. (2003) examined the effect of magnetostatic interactions of hysteresis

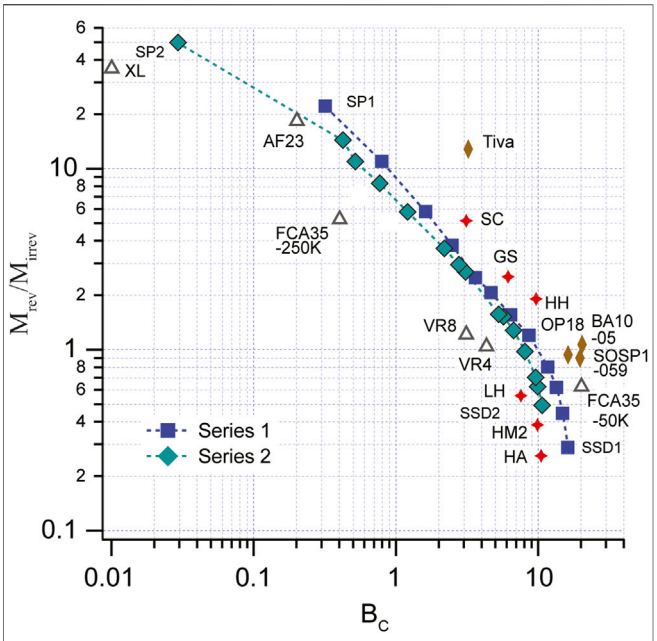

FIGURE 7 | Change in M_{rev}/M_{irrev} as a function of B_C for the geological, biological and material samples in relation to Series 1 and 2.

parameters using micromagnetic models, and demonstrated that the degree to which the parameters will be affected, will be dependent on particle anisotropies, degree of alignment, and particle configuration. For magnetite in the SSD range, magnetostatic interactions can lead to significantly lower values of M_{RS}/M_S, B_C and B_{CR}.

Dunlop (2002) presented a theoretical study in which he demonstrated how hysteresis parameters will change for SSD-SP mixtures, for SP particles between 10 and 30 nm. Dunlop and Carter-Stiglitz (2006) carried out an experimental study on the hysteresis properties of a mixture of SSD magnetite and a ferrofluid of SP magnetite, and found that B_{CR}/B_C was lower than predicted, which they attributed to interactions. Roberts et al. (2018), provides a thorough discussion of the weakness of using this method, where they note, among other points, that Dunlop (2002) does not consider thermal relaxation in his mixtures of SSD-SP magnetite, which will have an effect on the magnetization ratio. When thermal relaxation of the viscous particle is considered, there is a more rapid drop in M_{RS}/M_S (Lanci and Kent, 2003; Kumari et al., 2015; Roberts et al., 2018). This is supported by experimental results (Dunlop-Cater-Stiglitz, 2006; Kumari et al., 2015).

Figure 2 shows the progression of M_{RS}/M_S and B_{CR}/B_C for the two SSD-SP series. Series 1 has higher coercivity ratios relative to Series 2, which would be expected due to the larger volume of the SP particles. How this is reflected in the natural samples or synthetic magnetic nanoparticles is seen in **Figure 5**. The samples from the three sets, which show coercivity ratios that would require the presence of very fine particles (<10 nm), according to Dunlop's (2002) theoretical results. The coercivity ratios, however, are consistent for a broad particle size spectra in the SP range when accounting for thermal relaxation (Lanci and Kent, 2003). It should also be noted that none of these three sets of samples show wasp-waisting (**Supplementary Figures S6–S8**). Samples AF23 and XL are synthetic nanoparticles with better constrained particle sizes that are close to the SP-SSD boundary. These two samples show the lowest magnetization ratios, similar to what was found in the SP end member of the mixing series. In summary there is a progression to lower values of M_{RS}/M_S and higher values of B_{CR}/B_C with increasing SP concentration, but all sample sets lie below the theoretical progression that is expected by only assuming Langevin behaviour.

The FORC diagrams for Series 1 shows a gradual progression of a FORC distribution from a diagram typical for SSD magnetite, which lies away from the origin. The first indication of an SP contribution at the origin of the FORC diagram is for the sample with 19% SP content, and this contribution becomes larger successively with each addition (**Supplementary Figure S3**). The SP end-member is confined to the origin with a slight upward shift. The second series only has a FORC distribution that is typical for magnetotactic bacteria with a broader coercivity spectrum that extends to the origin of the plot. There is no noticeable change in the FORC diagram, other than a gradual decrease in the intensity of the distribution, until the until 10th addition, when the hysteresis loop shows a weak wasp-waisting. The SP end member has only a weak expression at the origin, which suggests that the FORCs will be less influenced due to the faster relaxation of the smaller particle diameter in comparison to the SP end member of Series 1.

PCA analysis of the FORC data provides a more quantitative way to observe changes. Series 1 shows a regular change in the PC1 score with each increment (**Figure 3**; **Supplementary Table S6**), and the calculated FORC diagrams of the end members are in agreement with the FORC diagrams in their major features. If we compare Series 2 with Series 1, the starting SSD end member has a notable SP-contribution (86% SSD-concentration). The sample with the highest SP concentration (sample 17) compares with the sample with ca. 50% SSD--concentration, but the SP end-member of Series 2 falls around the 68% concentration of Series 1. The fact that a higher SSD concentration is predicted for the SP end member of Series 2 indicates that the PCA cannot properly assess the SP end member with its fast relaxation. This point is discussed below.

A comparison of the samples from geological samples projected onto Series 1 shows that the lacustrine sediments fall toward an SSD concentration of around 76–83% of Series 1 in PCA analysis (**Figure 6**). Bacterial magnetite is thought to be the main source of magnetite in the samples and this comparable to the SD end member of Series 2, which is bacterial magnetite. The Tiva Canyon Tuff sample lies by ca. 50% contribution of SP particles from Series 1 similar to the higher SP concentration in Series 2. Note that a largely SP content that was found by Till et al. (2011) from low temperature blocking in field-cooled and zero-field-cooled experiments. The biological samples also lie around an SSD concentration of around 74–80%. Note that all of the biological samples show an increase in isothermal remanent magnetization when measured at 77 K (Brem, 2006; Blaser,

2008). This confirms that all samples contain a certain amount of SP magnetite, but it is not possible to determine the concentration. The synthetic samples show a larger spread in particle size, which is in agreement to physical measurements. Samples VR4 and VR8 are mesocrystals of magnetite made up of ca. 9–11 nm crystallites that agglomerate into a single crystal with 45 nm diameter. The SP content reflects the remainder of crystallites or smaller aggregates in the colloidal solution (Reichel et al., 2017). Sample FCA35 is a synthetic magnetite with ca. 16 ± 1 nm core (pers. comm. F. Crippa). It is SP at room temperature but undergoes partial blocking at 250 K, where the PCA analysis suggest that ca. 50% of the magnetization is blocked. At 50 K, ca. 83% of the magnetization is blocked in comparison to Series 1. AF23 has a 23 ± 1 nm magnetite core (pers. comm. A. Fink), which is close to the SP-SSD boundary, and the same is found for XL, whose core diameter is close to being magnetically ordered at room temperature (Hirt et al., 2017). The two samples, however, have markedly different PC1 scores. Although it is difficult to reconcile this difference, it should be noted that AF23 consists of a single magnetite crystal, whereas XL is a mesocrystal, i.e., an assemblage of smaller subunits, in which all have the same crystallographic orientation.

The last method to qualitatively assess the SP contribution to the magnetization is a comparison of the reversible to irreversible magnetization. This method assumes that magnetite is non-interacting as in the case of the Day-Dunlop plot. Both mixing series show an increase in M_{rev}/M_{irrev} with increasing SP concentration. This parameter can be plotted as a function of B_C, which will decrease as the SP-content increases. We use a log plot, because the increase in the ratio is small for low concentrations for the SP end member. There is a progressive increase in M_{rev}/M_{irrev} accompanied by the decrease in B_C, which would be expected. The track that the progression follows will be sensitive to the coercivity of the SSD end member, i.e., where the progression starts on the plot. This effect is seen for the lake sediments that have a higher coercivity than the SSD end member of Series 1, and therefore lie to the higher coercivity end of Series 1. The size of the SP end member affects how rapidly M_{rev}/M_{irrev} will increase; therefore, higher M_{rev}/M_{irrev} will be reached for lower SP content. Although one would expect $M_{rev}/M_{irrev} < 0.5$ for magnetite that is controlled by magnetocrystalline anisotropy, it is also found in the samples for which there is independent evidence for interaction between particles (Wohlfarth ratios).

Plots of $\partial M_{rev}/\partial B$ and $\partial M_{irrev}/\partial B$ are also of value (cf., **Supplementary Figures S3, S4, S6–S8**). For Series 1 M_{irrev} is characterized by a Gaussian curve. With the first addition of an SP component, little change is seen in the general shape of the hysteresis curve, or the FORC diagram, but the Gaussian curve shows a weak deviation on its flank around $\partial B = 0$. This feature becomes stronger with each addition of the SP material until two separate peaks are seen. It is these two distinct coercivity contributions that lead to wasp-waisting in the hysteresis curve. Note, in the case of Series 2, however, this secondary peak is not seen in M_{irrev}.

In summary, three methods were evaluated for detecting SP magnetite in mixtures with SSD magnetite. Both the Day-Dunlop plot and M_{rev}/M_{irrev} will see a progression that is related to the amount of SP particles in a material. Critical for the progression in the Day-Dunlop plot is the SP particles size, whereas it is the coercivity of the SSD end member that will be important for M_{rev}/M_{irrev} plotted as a function of B_C. Both methods, however, assume that the magnetite is non-interacting. If interactions occur between the magnetite particles, then there will be a reduction in M_{RS}/M_S, B_C, and B_{CR}, which would predict falsely a higher SP concentration. This may not be serious for weak interactions, as seen in the example of OP 18 compared to SOSP1-059, but would not be suitable for an assembly of interacting particles. A critical point is that both approaches are also not applicable if there are particles that are larger than SSD, which would also contribute to the reversible magnetization.

FORC analysis and PCA of the FORC measurements is suitable in detecting SP content, particularly when the SP particles are near to the SP-SSD boundary. The method loses its sensitivity when the SP particles are very fine and have short relaxation times. Fine SP particles will still contribute to the induced magnetization, which is why they affect hysteresis and M_{rev}/M_{irrev}, but will have less of a contribution to the FORC distribution. The SP concentration, which the PCA analysis calculates, will be dependent on knowing what the correct end members are so that they can be fitted. This can often be a limiting factor, particularly in natural samples that can show variability within a given locality, and the number of end members may not be clear. The smoothing factor, which is used to process the FORCs, will also play a role in any comparison of FORC results, therefore all data sets should be processed using the same smoothing factor.

In addition to problems that will arise if there are particles that are larger than SSD, or are interacting magnetically, we extend further caveats with respect to all three approaches. Firstly, the presence of other mineral phases, e.g., hematite, will greatly affect hysteresis properties. Mixtures of different ferromagnetic minerals with different particle sizes will lead to competing factors, which will not be possible to separate. Secondly, performing a slope correction could remove part of the contribution from the superparamagnetic contribution. Thirdly, averaging time of measurements is another factor that needs consideration and plays an important role in any comparison. Samples should only be evaluated if their measurement has been made using the same averaging time. Longer averaging time will lead to more relaxation during a measurement, thus influencing the reversible magnetization.

We can ask how often one deals with ideal mixtures of SSD-SP particles that are only made up of non-interacting magnetite. They are most likely to be found in synthetic particles, and the above approaches can be very useful in the characterization of these systems. Depending on the source of the ferromagnetic particles in biological systems, these are also often limited to finer particles. The problem in tissue samples, however can be clustering, and therefore meeting the criterion of non-interaction. For example, Brem et al. (2006) found clustering between magnetite/maghaemite particles in the brain tissues that were studied, but measurements had to be made on freeze-dried

tissue that was compressed. They could not conclude if the particles were clustered naturally or due to sample preparation. In any case these presented methods can provide useful information in a comparison of different tissues, although some overestimation of the SP concentration may occur. The same can be said for natural materials. These can have more variety in the composition of ferromagnetic (s.l.) phases, and in particle size, which may not include only SP and SSD particle size. The degree of magnetic interaction may also be more common. Critical is that magnetite is the main ferromagnetic phase, and there is independent evidence that the effect due to interactions is not large.

CONCLUSION

We have evaluated three methods to estimate the relative contribution of SP magnetite to mixtures with SSD magnetite, using two mixing series of SSD magnetite with SP magnetite, which have two different particle sizes. Both the Day-Dunlop plot or M_{rev}/M_{irrev} plotted as a function of B_C will detect changes in the SP contribution to the magnetization. PCA analysis of FORC measurements will also detect changes in the relative amount of SP particles, but is less sensitive in distinguishing small differences. The particle size or size distribution will affect the relatively change in magnetization with increasing SP concentration in all three methods. For this reason, the methods provide a qualitative method for assessing the concentration of SP magnetite, although comparisons within a selected group of samples may provide semi-quantitative information.

DATA AVAILABILITY STATEMENT

The raw data supporting the conclusions of this article will be made available by the authors, without undue reservation.

ETHICS STATEMENT

The studies involving human participants were reviewed and approved by University Hospital- Zurich Medical Ethics Committee. Written informed consent for participation was not required for this study in accordance with the national legislation and the institutional requirements.

AUTHOR CONTRIBUTIONS

PL and AH contributed equally to the experimental design, data acquisition, data evaluation and writing the manuscript.

FUNDING

PL acknowledges support from the financial support from the following agencies: China Scholarship Council (No. 201706410009), the Science and Technology Development Fund, Macau SAR (Project No. 0002/2019/APD).

ACKNOWLEDGMENTS

We thank M. Kumari for her helpful discussion. A. Petro-Fink and F. Crippa are acknowledged for use of their magnetic nanoparticle samples, and O. Paasche for sample OP18. We gratefully acknowledged the comments of two reviewers and L. Sagnotti for improving this manuscript.

SUPPLEMENTARY MATERIAL

The Supplementary Material for this article can be found online at: https://www.frontiersin.org/articles/10.3389/feart.2020.586913/full#supplementary-material.

REFERENCES

Beyhum, W., Hautot, D., Dobson, J., and Pankhurst, Q. A. (2005). Magnetic biomineralisation in huntington's disease transgenic mice. *J. Phys. Conf. Ser.* 17, 50–53. doi:10.1088/1742-6596/17/1/008

Blaser, C. (2008). *Magnetic iron mineralogy in human tissue from brain tumors*. Zürich, Switzerland: University of Zürich.

Brem, F., Hirt, A. M., Winklhofer, M., Frei, K., Yonekawa, Y., Wieser, H. G., et al. (2006). Magnetic iron compounds in the human brain: a comparison of tumour and hippocampal tissue. *J. R. Soc. Interface*. 3, 833–841. doi:10.1098/rsif.2006.0133

Brem, F. K. (2006). Magnetic characterization of iron phases in human brain tissue: application to epileptic and tumour tissue. Zürich, Switzerland: ETH Zürich.

Calderon-Garciduenas, L., Gonzalez-Maciel, A., Mukherjee, P. S., Reynoso-Robles, R., Perez-Guille, B., Gayosso-Chavez, C., et al. (2019). Combustion and friction-derived magnetic air pollution nanoparticles in human hearts. *Environ. Res.* 176, 108567. doi:10.1016/j.envres.2019.108567

Crippa, F., Moore, T. L., Mortato, M., Geers, C., Haeni, L., Hirt, A. M., et al. (2017). Dynamic and biocompatible thermo-responsive magnetic hydrogels that respond to an alternating magnetic field. *J. Magn. Magn Mater.* 427, 212–219. doi:10.1016/j.jmmm.2016.11.023

Crippa, F., Rodriguez-Lorenzo, L., Hua, X., Goris, B., Bals, S., Garitaonandia, J. S., et al. (2019). Phase transformation of superparamagnetic iron oxide nanoparticles *via* thermal annealing: implications for hyperthermia applications. *ACS Appl. Nano Mater.* 2, 4462–4470. doi:10.1021/acsanm.9b00823

Day, R., Fuller, M., and Schmidt, V. A. (1977). Hysteresis properties of titanomagnetite: grain size and compositional dependence. *Phys. Earth Planet. Inter.* 13, 260–267. doi:10.1016/0031-9201(77)90108-X

Dearing, J. R., Dann, R. J. L., Hay, K., Lees, J. A., Loveland, P. J., Maher, B. A., et al. (1996). Frequency-dependent susceptibility measurements of environmental materials. *Geophys. J. Int.* 124, 228–240. doi:10.1111/j.1365-246X.1996.tb06366.x

Dekkers, M. J. (1988). *Some rock magnetic parameters for natural goethite, pyrrhotite, and fine-grained hematite*. PhD dissertation. Utrecht (Netherlands): University of Utrecht.

Dobson, J. (2004). Magnetic iron compounds in neurological disorders. *Ann. N. Y. Acad. Sci.* 1012, 183–192. doi:10.1196/annals.1306.016

Dunlop, D. J. (2002). Theory and application of the Day plot (M_{rs}/M_s versus H_{cr}/H_c) 1. Theoretical curves and tests using titanomagnetite data. *J. Geophys. Res. Solid Earth*. 107, 2056. doi:10.1029/2001jb000486

Dunlop, D. J., and Carter-Stiglitz, B. (2006). Day plots of mixtures of superparamagnetic, single-domain, pseudosingle-domain, and multidomain

magnetites. *J. Geophys. Res. Solid Earth*. 111, B12S09. doi:10.1029/2006JB004499

Dunlop, D. J., and Özdemir, Ö. (1997). *Rock magnetism: fundamentals and Frontiers*. Cambridge, United Kingdom: Cambridge University Press.

Egli, R. (2004a). Characterization of individual rock magnetic components by analysis of remanence curves. 2. Fundamental properties of coercivity distributions. *Phys. Chem. Earth*. 29, 851–867. doi:10.1016/j.pce.2004.04.001

Egli, R. (2004b). Characterization of individual rock magnetic components by analysis of remanence curves. 3. Bacterial magnetite and natural processes in lakes. *Phys. Earth Planet. Int*. 29, 869–884. doi:10.1016/j.pce.2004.03.010

Egli, R. (2003). *Environmental influences on the magnetic proeprties of lake sediments*. Zürich, Switzerland: ETH-Zurich.

Egli, R. (2013). VARIFORC: an optimized protocol for calculating non-regular first-order reversal curve (FORC) diagrams. *Global Planet. Change*. 110, 302–320. doi:10.1016/j.gloplacha.2013.08.003

Faivre, D., and Schüler, D. (2008). Magnetotactic bacteria and magnetosomes. *Chem. Rev.* 108, 4875–4898. doi:10.1021/cr078258w

Geiss, C. E., Heider, F., and Soffel, H. C. (1996). Magnetic domain observations on magnetite and titanomaghemite grains (0.5-10mm). *Geophys. J. Int.* 124, 75–88. doi:10.1111/j.1365-246X.1996.tb06353.x

Harrison, R. J., and Feinberg, J. M. (2008). FORCinel: an improved algorithm for calculating first-order reversal curve distributions using locally weighted regression smoothing. *Geochem. Geophys. Geosyst.* 9, Q05016. doi:10.1029/2008GC001987

Harrison, R. J., Muraszko, J., Heslop, D., Lascu, I., Muxworthy, A. R., and Roberts, A. P. (2018). An improved algorithm for unmixing first-order reversal curve diagrams using principal component analysis. *Geochem. Geophys. Geosyst.* 19, 1595–1610. doi:10.1029/2018GC007511

Heider, F. (1988). *Magnetic properties of hydrothermally grown Fe_3O_4 crystals*. PhD dissertation, Toronto (ON): University of Toronto.

Heider, F., Zitzelsberger, A., and Fabian, F. (1996). Magnetic susceptibility and remanent coercive force in grown magnetite crystals from 0.1 μm to 6 mm. *Phys. Earth Planet. Int*. 93, 239–256. doi:10.1016/0031-9201(95)03071-9

Heslop, D. (2005). A Monte Carlo investigation of the representation of thermally activated single-domain particles within the day plot. *Stud. Geophys. Geod.* 49, 163–176. doi:10.1007/s11200-005-0003-7

Hirt, A. M., Kumari, M., Heinke, D., and Kraupner, A. (2017). Enhanced methods to estimate the efficiency of magnetic nanoparticles in imaging. *Molecules* 22, 2204. doi:10.1039/c6ra03115c

Hosking, D. E., Ayton, S., Beckett, N., Booth, A., and Peters, R. (2018). More evidence is needed. Iron, incident cognitive decline and dementia: a systematic review. *Ther. Adv. Chron. Dis.* 9, 241–256. doi:10.1177/2040622318788485

Hrouda, F. (2011). Models of frequency-dependent susceptibility of rocks and soils revisited and broadened. *Geophys. J. Int.* 187, 1259–1269. doi:10.1111/j.1365-246X.2011.05227.x

Ilyashuk, E. A., Koinig, K. A., Heiri, O., Ilyashuk, B. P., and Psenner, R. (2011). Holocene temperature variations at a high-altitude site in the Eastern Alps: a chironomid record from Schwarzsee ob Sölden, Austria. *Quat. Sci. Rev.* 30, 176–191. doi:10.1016/j.quascirev.2010.10.008

Jacob, J. J., and Suthindhiran, K. (2016). Magnetotactic bacteria and magnetosomes—scope and challenges. *Mater. Sci. Eng. C Mater. Biol. Appl.* 68, 919–928. doi:10.1016/j.msec.2016.07.049

Katzmann, E., Eibauer, M., Lin, W., Pan, Y., Plitzko, J. M., and Schüler, D. (2013). Analysis of magnetosome chains in magnetotactic bacteria by magnetic measurements and automated image analysis of electron micrographs. *Appl. Environ. Microbiol.* 79, 7755–7762. doi:10.1128/AEM.02143-13

Kind, J., Gehring, A. U., Winklhofer, M., and Hirt, A. M. (2011). Combined use of magnetometry and spectroscopy for identifying magnetofossils in sediments. *Geochem. Geophys. Geosyst.* 12, Q08008. doi:10.1029/2011GC003633

Kumari, M., Hirt, A. M., Uebe, R., Schuler, D., Tompa, É., Posfai, M., et al. (2015). Experimental mixtures of superparamagnetic and single-domain magnetite with respect to Day-Dunlop plots. *Geochem. Geophys. Geosyst.* 16, 1739–1752. doi:10.1002/2015GC005744

Kumari, M., Widdrat, M., Tompa, E., Uebe, R., Schuler, D., Mihaly, P., et al. (2014). Distinguishing magnetic particle size of iron oxide nanoparticles with first-order reversal curves. *J. Appl. Phys.* 116, 124304. doi:10.1063/1.4896481

Lanci, L., and Kent, D. V. (2003). Introduction of thermal activation in forward modeling of hysteresis loops for single-domain magnetic particles and implications for the interpretation of the Day diagram. *J. Geophys. Res. Solid Earth*. 108, 2124. doi:10.1029/2001jb000944

Lascu, I., Harrison, R. J., Li, Y., Muraszko, J. R., Channell, J. E. T., Piotrowski, A. M., et al. (2015). Magnetic unmixing of first-order reversal curve diagrams using principal component analysis. *Geochem. Geophys. Geosyst.* 16, 2900–2915. doi:10.1002/2015GC005909

Liu, P. F., Hirt, A. M., Schuler, D., Uebe, R., Zhu, P. M., Liu, T. Y., et al. (2019). Numerical unmixing of weakly and strongly magnetic minerals: examples with synthetic mixtures of magnetite and hematite. *Geophys. J. Int.* 217, 280–287. doi:10.1093/gji/ggz022

Lohsse, A., Kolinko, I., Raschdorf, O., Uebe, R., Borg, S., Brachmann, A., et al. (2016). Overproduction of magnetosomes by genomic amplification of biosynthesis-related gene clusters in a magnetotactic bacterium. *Appl. Environ. Microbiol.* 82, 3032–3041. doi:10.1128/AEM.03860-15

Maher, B. A., Ahmed, I. A., Karloukovski, V., Maclaren, D. A., Foulds, P. G., Allsop, D., et al. (2016). Magnetite pollution nanoparticles in the human brain. *Proc. Natl. Acad. Sci. U.S.A.* 113, 10797–10801. doi:10.1073/pnas.1605941113

Moskowitz, B. M., Frankel, R., and Bazylinski, D. (1993). Rock magnetic criteria for the detection of biogenic magnetite. *Earth Planet. Sci. Lett.* 120, 283–300. doi:10.1016/0012-821X(93)90245-5

Muxworthy, A., Williams, W., and Virdee, D. (2003). Effect of magnetostatic interactions on the hysteresis parameters of single-domain and pseudo-single-domain grains. *J. Geophys. Res. Solid Earth*. 108, 2517. doi:10.1029/2003jb002588

Newell, A. J. (2005). A high-precsion model of first-order reversal curve (FORC) functions for single-domain ferromagnetic with uniaxial anisotropy. *Geochem. Geophsy. Geosys.* 6, Q05010. doi:10.1029/2004GC00877

Pike, C. R., Roberts, A. P., and Verosub, K. L. (2001). First-order reversal curve diagrams and thermal relaxation effects in magnetic particles. *Geophys. J. Int.* 145, 721–730. doi:10.1046/j.0956-540x.2001.01419.x

Reichel, V., Kovács, A., Kumari, M., Bereczk-Tompa, É., Schneck, E., Diehle, P., et al. (2017). Single crystalline superstructured stable single domain magnetite nanoparticles. *Sci. Rep.* 7, 45484. doi:10.1038/srep45484

Roberts, A. P., Tauxe, L., Heslop, D., Zhao, X., and Jiang, Z. X. (2018). A critical appraisal of the "Day" diagram. *J. Geophys. Res. Solid Earth*. 123, 2618–2644. doi:10.1002/2017JB015247

Sotiriou, G. A., Hirt, A. M., Lozach, P. Y., Teleki, A., Krumeich, F., and Pratsinis, S. E. (2011). Hybrid, silica-coated, janus-like plasmonic-magnetic nanoparticles. *Chem. Mater.* 23, 1985–1992. doi:10.1021/cm200399t

Starsich, F. H., Sotiriou, G. A., Wurnig, M. C., Eberhardt, C., Hirt, A. M., Boss, A., et al. (2016). Silica-coated nonstoichiometric nano Zn-ferrites for magnetic resonance imaging and hyperthermia treatment. *Adv. Healthcare Mater.* 5, 2698–2706. doi:10.1002/adhm.201600725

Starsich, F. H. L., Eberhardt, C., Boss, A., Hirt, A. M., and Pratsinis, S. E. (2018). Coercivity determines magnetic particle heating. *Adv. Healthcare Mater.* 7, e1800287. doi:10.1002/adhm.201800287

Storen, E. W. N., Paasche, O., Hirt, A. M., and Kumari, M. (2016). Magnetic and geochemical signatures of flood layers in a lake system. *Geochem. Geophys. Geosyst.* 17, 4236–4253. 10.1002/2016GC006540

Sweetkind, D. S., Reynolds, R. L., Sawyer, D. A., and Rosenbaum, J. G. (1993). Effects of hydrothermal alteration on the magnetization of the oligocene carpenter ridge tuff, bachelor caldera, san juan mountains, Colorado. *J. Geophys. Res.: Solid Earth*. 98, 6255–6266. doi:10.1029/93JB00014

Tauxe, L., Mullender, T. A. T., and Pick, T. (1996). Potbellies, wasp-waists, and superparamagnetism in magnetic hysteresis. *J. Geophys. Res. Solid Earth*. 101, 571–583. doi:10.1029/95JB03041

Till, J. L., Jackson, M. J., Rosenbaum, J. G., and Solheid, P. (2011). Magnetic properties in an ash flow tuff with continuous grain size variation: a natural

reference for magnetic particle granulometry. *Geochem. Geophsy. Geosyst.* 12, Q07Z26. doi:10.1029/2011GC003648

Widdrat, M., Kumari, M., Tompa, É., Pósfai, M., Hirt, A. M., and Faivre, D. (2014). Keeping nanoparticles fully functional: long-term storage and alteration of magnetite. *Chempluschem*. 79, 1225–1233. doi:10.1002/cplu.201402032

Winklhofer, M., Dumas, R. K., and Liu, K. (2008). Identifying reversible and irreversible magnetization changes in prototype patterned media using first and second-order reversal curves. *J. Appl. Phys.* 103, 07C518. doi:10.1063/1.2837888

Conflict of Interest: The authors declare that the research was conducted in the absence of any commercial or financial relationships that could be construed as a potential conflict of interest.

frontiers in Earth Science

ORIGINAL RESEARCH
published: 24 February 2021
doi: 10.3389/feart.2020.608387

Ultrafine Magnetic Particles: A DIET-Proxy in Organic Rich Sediments?

Andrea Teixeira Ustra[1], Carlos Mendonça[1], Aruã da Silva Leite[2,3], Melina Macouin[2,3], Rory Doherty[4], Marc Respaud[2,5] and Giovana Tocuti[1]*

[1]Department of Geophysics, University of São Paulo, São Paulo, Brazil, [2]Université de Toulouse, Toulouse, France, [3]GET/OMP, UMR CNRS 5563, Université Paul-Sabatier, Toulouse, France, [4]School of Natural and Built Environment, Queen's University Belfast, Belfast, United Kingdom, [5]LPCNO-INSA Toulouse, CNRS, CEMES, UPR 8011, Université de Toulouse, Toulouse, France

In this work we present results of the magnetic properties characterization of sediment samples from a brownfield site that is generating methane biogas in São Paulo–Brazil. We applied interpretation procedures (frequency dependent susceptibility and time-dependent Isothermal Remanent Magnetization) appropriate to study the ultrafine magnetic fraction response of the samples. The higher content of superparamagnetic (SP) particles correlates well with the detected biogas pockets, suggesting that the methanogens activity produces these ultrafine particles, different from the magnetic particles at other depth levels. We propose the use of two simple measurement and interpretation techniques to identify such magnetic particles fingerprints. The results presented here support the use of environmental magnetism techniques to investigate biogeochemical processes of anaerobic microbial activity.

Keywords: direct inter species electron transfer (DIET), magnetic nanoparticles, superparamagnetic particles, methane, brownfield, organic rich sediments

OPEN ACCESS

Edited by:
Bernard A. Housen, Western Washington University, United States

Reviewed by:
Diana Jordanova, National Institute of Geophysics, Geodesy and Geography (BAS), Bulgaria
Maodu Yan, Institute of Tibetan Plateau Research (CAS), China

****Correspondence:***
Andrea Teixeira Ustra
andrea.ustra@iag.usp.br

Specialty section:
This article was submitted to Geomagnetism and Paleomagnetism, a section of the journal Frontiers in Earth Science

Received: *20 September 2020*
Accepted: *30 December 2020*
Published: *24 February 2021*

Citation:
Ustra AT, Mendonça C, Leite AS, Macouin M, Doherty R, Respaud M and Tocuti G (2021) Ultrafine Magnetic Particles: A DIET-Proxy in Organic Rich Sediments?. Front. Earth Sci. 8:608387. doi: 10.3389/feart.2020.608387

INTRODUCTION

Organic matter buried in anaerobic environments, (e.g. landfills or organic-rich sediments) is oxidized through a series of biogeochemical processes producing methane and carbon dioxide as major products (Christensen, 2010). The well-known electron sources for carbon dioxide reduction to methane are H_2 (Sieber et al., 2012) or other dissolved carriers (Bryant et al., 1967; Stams and Plugge, 2009). Recent findings however have shown that *Methanosaeta* and *Methanosarcina* species can directly accept electrons from *Geobacter* as donors via direct interspecies electron transfer (DIET), in this process reducing carbon dioxide to methane (Chen et al., 2014a; Rotaru et al., 2014a; Chen et al., 2014b; Rotaru et al., 2014b; Wang et al., 2016; Xiao et al., 2018). Possible mechanisms of electron transfer in DIET-based syntrophy seem to be through electrified paths formed by pili-like appendages with conductive minerals or outer cell electrical connectors of adjacent partners (Lovley, 2017). DIET connection of *Methanosaeta* with *Geobacter* species has been recognized (Summers et al., 2010; Lovley, 2011; Shrestha et al., 2013a; Shrestha et al., 2013b) and assumed as a major player in global methane budget (Rotaru et al., 2014b). Methane production based on DIET can be stimulated by introducing conductive particulates (Martins et al., 2018), such as biochar (Chen et al., 2014a; Xiao et al., 2019); carbon cloth (Li et al., 2018) and magnetite nanoparticles (Kato et al., 2012; Zhang and Lu, 2016; Xiao et al., 2018) suggesting the importance of conductive particulate to shuttle interspecies electron-transport.

In principle, syntrophic DIET associations can sustain methanogenesis in H_2 depleted environments (or other dissolved carriers) by directly coupling iron-reducing bacteria with methanogens. It is accepted that the partnership between *Geobacter* and *Methanosarcina* can competitively exclude acetoclastic methanogens like *Methanothrix* in the absence of dissolved electron carrier (Rotaru et al., 2018). Paddy soil incubation of ferrihydrite indicates that methanogenesis is initially suppressed as magnetite grains are produced and *Geobacter* proliferates, and then enhanced as DIET develops using the magnetite network for interspecies electrical connections (Liu et al., 2015). Other species such as *Syntrophomonas* have been proposed as candidates for DIET with *Methanosaeta* suggesting that many microorganisms are capable of DIET processes (Zhao et al., 2018).

Magnetite production and alteration then may develop a major role in DIET syntrophy, either in stages in which Fe(III) reduction are catalyzed by iron-reducing bacteria as used to convey electron-transfer between interspecies partners. Iron speciation by dissimilatory iron-reducing bacteria is widespread in waterlogged soils (Lovley et al., 1987; Maher and Taylor 1988) and their importance for iron cycling in such environments makes them a key potential source of ultra-fine soil magnetite (Roberts, 2015). A proxy characterizing concentration and magnetite properties (grain size and mineral type, for example) may be useful to recognize a biogeochemical process active in modern environments or recorded in continuous coring of sedimentary sequences. A diversity of iron-reducing microorganisms can convert poorly crystalline Fe(III) oxy/hydroxides to extracellular magnetite while using Fe(III) as an electron acceptor for the oxidation of organic compounds (Lovley et al., 2004). The Fe (III) reducing bacteria *Geothrix* has been shown to produce magnetite at brownfield sites (Klueglein et al., 2013) and it has been suggested the Geothrix can act in syntrophy with methanogens though not necessarily via a DIET mechanism (Sutcliffe et al., 2018). Common Fe(III) minerals in soils and sediments are hematite (α-Fe_2O_3), ferrihydrite ($5Fe_2O_3.9H_2O$) or oxyhydroxides goethite (α-FeOOH), lepidocrocite (γ-FeOOH). The reduction of Fe(III) minerals to produce magnetite (Fe_3O_4) is energetically favorable (~0.01 eV), adding 1 Bohr magneton (9.27×10^{-24} Am^2) to the crystalline frame, which represents a magnetization upgrade of about 25% (Liu et al., 2012).

Depending on culture conditions and bacterial forms (Vali et al., 2004), the respiration of iron-reducing bacteria based on solid Fe(III) mineral phases produces extracellular magnetite crystals (Lovley et al., 1987; Lovley, 1991; Coker et al., 2008) of ultrafine grains with diameters between 10 and 50 nm. The extracellular crystallization process results in particles lacking characteristic morphology but usually with superparamagnetic (SP) properties at room temperature (Moskowitz et al., 1993). The superparamagnetic response is observed when single-domain, ferromagnetic minerals are below a critical blocking volume, unable to sustain permanent magnetization at room temperature. Incubation of metal-reducing bacteria with Fe(III) oxyhydroxides have produced magnetite nanoparticles with diameters between 10 and 15 nm for bacterium *Geobacter sulfurreducens* (Byrne et al., 2015) and between 26 nm and 38 nm for bacterium *Shewanella* (Lee et al., 2008). In many environments the magnetic properties associated to ultrafine magnetite particles must be isolated in order to better understand the superparamagnetic signature associated to iron-reducing bacteria and their role in DIET syntrophy.

In this paper we study a trapped gas pocket formed in Quaternary organic sediments, by tracking specific mineral changes that can be associated to biogeochemical processes. We focus our analysis on changes regarding the magnetic carrier mineralogy analyzing the frequency dependent susceptibility and time-dependent Isothermal Remanent Magnetization (IRM) to detect subtle physical and compositional variations that could be indicative of a DIET process. In addition to classic techniques used in environmental magnetism (thermomagnetic and hysteresis curves) we apply specific procedures to characterize the SP mineral content in terms of volume variations and concentration estimates along a cored section that intercepts a methane pocket trapped within organic-rich sediments. We recognize an association between iron-reducing bacteria and occurrence of SP minerals at a region were iron-reduction is developed and methane accumulation observed, possibly according to a DIET scheme.

MATERIALS AND METHODS

Research Site

The studied site is situated at a flood plain of the Tietê River, in São Paulo - SP, Brazil. The area contains a series of anthropogenic deposits (~4 m) that overlies Quaternary fluvial sediments (~6 m) and Neogene sandstones. The entire site was formerly used as a large drying pool for dredged sediments when a nearby channel was opened. The sediments settled in the pool kept under anoxic conditions the organic-rich sediments of the fluvial plain inducing methanogenic processes and methane trapping within sandy lenses at different depths of the section. Two main methane pockets were sampled along three multilevel monitoring wells, each one with 15 gas and water sampling ports 0.6 m spaced down to 8.6 m in the Quaternary section (Mendonça et al., 2015a). Continuous samples of direct-push coring were analyzed for total content of organic carbon and grain size laser diffraction Mendonça et al. (2015a). The trapped pockets of biogas were identified within a thick (approximately 6 m) layer of organic-rich sediments, with organic carbon up to 40% in weight. The pockets of methane were confirmed by direct gas sampling from the multilevel monitoring wells (**Figure 1**). The shallower accumulation (top at ~2.5 m) has pressure equilibrated to the atmosphere, while the deeper gas reservoir (depth ~6 m) is overpressured to about 0.4–0.5 kPa above the atmosphere. Gas composition in both reservoirs is enriched in CH_4, about 37–45% of CO_2 to 55–63% CH_4, with traces of H_2S (~30 ppm). The piezometric surface is relatively flat, with a hydraulic gradient of 0.0082 towards the river

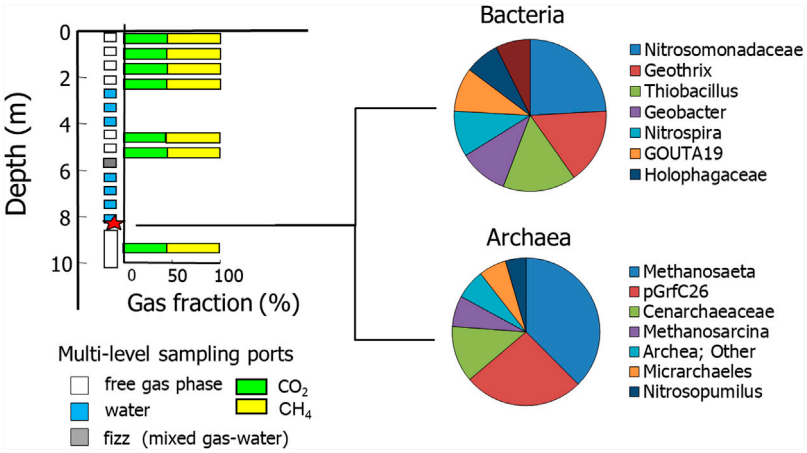

FIGURE 1 | Gas composition sampled in a multi-level borehole and typical bacterial and archaeal genus-level taxonomic profile of suspended sediment in groundwater from different depths (modified from Mendonça et al., 2015b).

channel. High permeability (12–62 cm day^{-1}) of the surface anthropogenic layer does not work as an efficient sealing unit for gas pockets volumes reaching the vadose zone but it facilitates water recharge and removal of gas in this zone as the water infiltrates. A monthly based ERT (Earth Resistivity Tomography) imaging recognized one episode with methane release and paths for water infiltration during rainy periods (Mendonça et al., 2015b).

Sediments recovered from groundwater sampled from the multi-wells underwent microbial analysis. Groundwater sampled from the multi-wells underwent microbial analysis. Procedures for microbial DNA extractions, bacterial and archaeal pyrosequencing, and sequence analysis are described in Mendonça et al. (2015b). It was found that the methane-producing archaea *Methanosaeta* are ubiquitous in the environment and probably generates the methane and carbon dioxide gas pockets trapped beneath impervious layers (**Figure 1**). The distribution of methanogens is well correlated with the methane pockets and higher levels of acetate. *Methanosaeta* species have high affinity for acetate (Lee et al., 2014) and are ubiquitous in many natural environments. *Methanosaeta* species are also capable of direct interspecies electron accepting from some *Geobacter* species for the reduction of carbon dioxide to methane (Rotaru et al., 2014b). Based on these findings we undertook a sampling regime of the recovered cores for magnetic properties characterization to identify if there is a relationship between methane production within gas pockets and the production of biogenic magnetic minerals in soils at the same horizons.

Magnetic Properties Characterization

Magnetic properties of soils and rocks are strongly dependent upon magnetic carrier grain size, which are classified as multi domain (MD), stable single domain (SSD), (e.g. up to 50 nm for magnetite), pseudo single domain (PSD) or "*vortex*" structure. Magnetic particles formed by dissimilatory iron-reducing bacteria are typically ultrafine, as such generating mineral carriers with superparamagnetic properties, (e.g. ultrafine magnetite or greigite) from reducing Fe(III) minerals from background geological media. To characterize the magnetic properties within and in the vicinity of the methane pockets 21 sediment samples from direct pushing coring (every 0.5 m, from 0.5 to 10.5 m deep) were analysed with focus on their superparamagnetic content, by using frequency dependent susceptibility (FDS) and superparamagnetic concentration and dipole moment (SPCDM) analysis.

Thermomagnetic Curve

In this analysis, magnetic susceptibility changes as a function of temperature are recorded. The high temperature protocol consists of measurements during the heating stage, from room temperature to approximately 700 °C and then repeating measurements while the sample cools to room temperature. High temperature curves are useful to identify changes of mineral phase that take place at specific temperatures, (e.g. Curie temperature T_C or Néel temperature T_N). T_C marks the sudden loss of magnetization when a ferri- or ferro-magnetic mineral becomes paramagnetic in temperatures $T > T_C$. For magnetite, $T_C \sim 580$ °C. T_N is the analogous of the Curie temperature in antiferromagnetic minerals such as hematite ($T_N \sim 675$ °C), where the mineral becomes paramagnetic at temperatures $T > T_N$ (Dunlop and Özdemir, 2001).

Thermomagnetic curves can also show magnetic carrier size effect, such as the Hopkinson peak (sudden increase of susceptibility temperature until a peak reached before T_C). Özdemir and Dunlop (2014) reported a systematic trend of the Hopkinson's peak height with magnetic grain size for natural magnetite samples. Also recognizable is mineral phase transformations as the sample is heated and cooled. In this case, the heating and cooling curves are distinguishable from one another and are said to be irreversible, revealing mineralogical transformations caused by dehydration or change in the sample redox state.

The measurements presented in this work were taken with Kappabridge KLY-4S at USPMAG (University of São Paulo), at the heating rate of 0.2 °C/s under inert Ar atmosphere.

Magnetic Hysteresis

Hysteresis cycles are designed to observe the ability of a ferromagnetic material to acquire permanent magnetization under an external magnetic field. This feature is usually investigated by first applying a strong field magnetic (**H**) so that the magnetization (**M**) is saturated. As **H** is then decreased to zero, **M** does not fall to the origin. If the field increases in the opposite direction, **M** gradually falls to zero to then reverse again as the saturation magnetization is reached. Repeated cycling of H traces out the *hysteresis loop*.

The standard hysteresis parameters *Mr*, *Ms*, *Hc*, and *Hcr* (where *Mr* is the saturation remanence, *Ms* is the saturation magnetization, *Hc* is the coercive force, and *Hcr* is the coercivity of remanence) represent the bulk magnetic properties of the sample and are often used to characterize geological samples. Low coercivity materials will produce hysteresis loops of rectangular shape and mixtures of minerals with different coercivities may produce constricted hysteresis loops that are narrow in the middle section but wider above and below this region (wasp-waisted) (Tauxe et al., 1996, 2002).

The analysis of hysteresis loops at different temperatures may reveal changes in the magnetic domain state for the magnetic minerals. Magnetic grains below a certain particle size, for example, do not preserve magnetic remanence above a critical temperature, when the superparamagnetic condition is activated (Dunlop and Özdemir, 2001).

We used the Physical Properties Measurement System (PPMS) Quantum Design using a vibrating sample magnetometry (VSM) to record hysteresis loops at 300, 25, 10 and 5 K and maximum external field of approximately 5×10^4Oe.

First-Order Reversal Curves (FORC)

FORC diagrams (Pike et al., 1999; Roberts et al., 2000) provide further magnetic minerals and domain states characterization and the extent of magnetostatic interactions. FORC measurements start by saturating a sample in a strong positive field *Hr*, followed by changing the field to a negative field *Hr* and then sweeping it back to *Hr*. The difference between successive FORCs arises from irreversible magnetization changes that occur between successive reversal fields. FORCs distributions are interpreted in terms of the coercivity distribution and the interaction field distribution.

For example, an assemblage of noninteracting single domain particles produces closed concentric contours with negligible vertical spread of the FORC distribution, in contrast with the closed concentric contours with high vertical spread produced by interacting single domain particles. The superparamagnetic behavior is dominant in the FORC distribution when the measurement time is comparable to the relaxation times of particles near the SP-SSD threshold size (Pike et al., 2001). Multidomain particles produce a different feature in the FORC diagram, where the magnetic interactions among domain walls produce asymmetric contours, which make it straightforward to discriminate these particles.

Frequency Dependent Susceptibility (FDS)

FDS aims to quantify the SP-SSD response in terms of grain size variation able to explain the dependence of the magnetic susceptibility with grain size fining from a reference SSD characteristic volume. This formulation is based on the Debye relaxation model (Ustra et al., 2018) by considering measurements with three-frequency susceptibilimeters usually employed to characterize superparamagnetic contents in soil and rock magnetism. According to this model, the in-phase (or real) magnetic susceptibility $\chi_r = \chi(f)$ for an assemblage of uniform magnetic carrier is $\chi_r = \chi_h + \Delta\chi \frac{1}{1+(2\pi f\tau)^2}$. where χ_h is the FDS high-frequency limit, $\Delta\chi = \chi_l - \chi_h$ with χ_l as its corresponding low-frequency limit and τ is relaxation time constant. For measurements with a set of at least three frequencies f, (e.g. 976, 3,904 and 15,616 Hz as for the MFK1-FA Kappabridge susceptibility meter) the FDS data allow solving for unknown parameters $(\chi_h, \Delta\chi, \tau)$ according to a constrained, non-linear data-fitting procedure (Ustra et al., 2019). Once estimated, such model parameters are used to determine the transition parameter $F_t = \chi_l/\chi_h = v/v_c$, that relates the mean volume v for the particle assemblage with respect to a characteristic volume $v_c = \frac{2k_BT}{\mu_0 H_K M_S}$.

Standing for the respective mineral grains in the SP-SSD transition, in which M_S is the sample saturation magnetization [Am^{-1}], k_B $1{,}38 \times 10^{-23}$ [JK^{-1}] is the Boltzmann constant and T [K] is the temperature H_K [Am^{-1}]is the sample macroscopic coercivity and $\mu_0 = 4\pi \times 10^{-7}$ [Hm^{-1}] is the free space permeability. The quantity F_t^{-1}, such that $v_c = F_t^{-1}v$, can be regarded as a fining proxy since it expresses how much the particles go finer having as reference the characteristic volume for the grain. As discussed by Ustra et al. (2019) the determination of volume v according to the Neel's model $v = v_c \ln(\tau/\tau_0)$ is inaccurate using inferences for τ from data sets with three-frequencies only. Characteristic time τ_0 is a time-factor varying from 10^{-12} to 10^{-8} s (Dormann et al., 1996; Worm 1999). We use the MATLAB program *FDS_inv.m* (Ustra et al., 2019) to invert the three-frequency dataset acquired with Kappabridge MK1 at LabCore (University of São Paulo).

Superparamagnetic Concentration and Dipole Moment (SPCDM)

The SPCDM procedure developed by Leite et al. (2018) is based on Neél's model for superparamagnetism for which sample magnetization $M(B_i, T)$ is dependent of the external applied field (B_i) and temperature $M(B_i, T) = M_S L\left(\frac{\mu B_i}{k_B T}\right)$ in which μ is the mean moment of dipole [Am^2] of the magnetic carrier composing the sample; B_i is the external magnetic field applied to the sample, L is the Lagrange function such that $L(\alpha) = \coth(\alpha) - 1/\alpha$. The magnetization is such that $M_S = \eta\mu$, the term η [m^{-3}] expressing the concentration (number of particles per volume) of the magnetic carriers. For a sample with density ρ [kgm^{-3}], the mass concentration of the magnetic

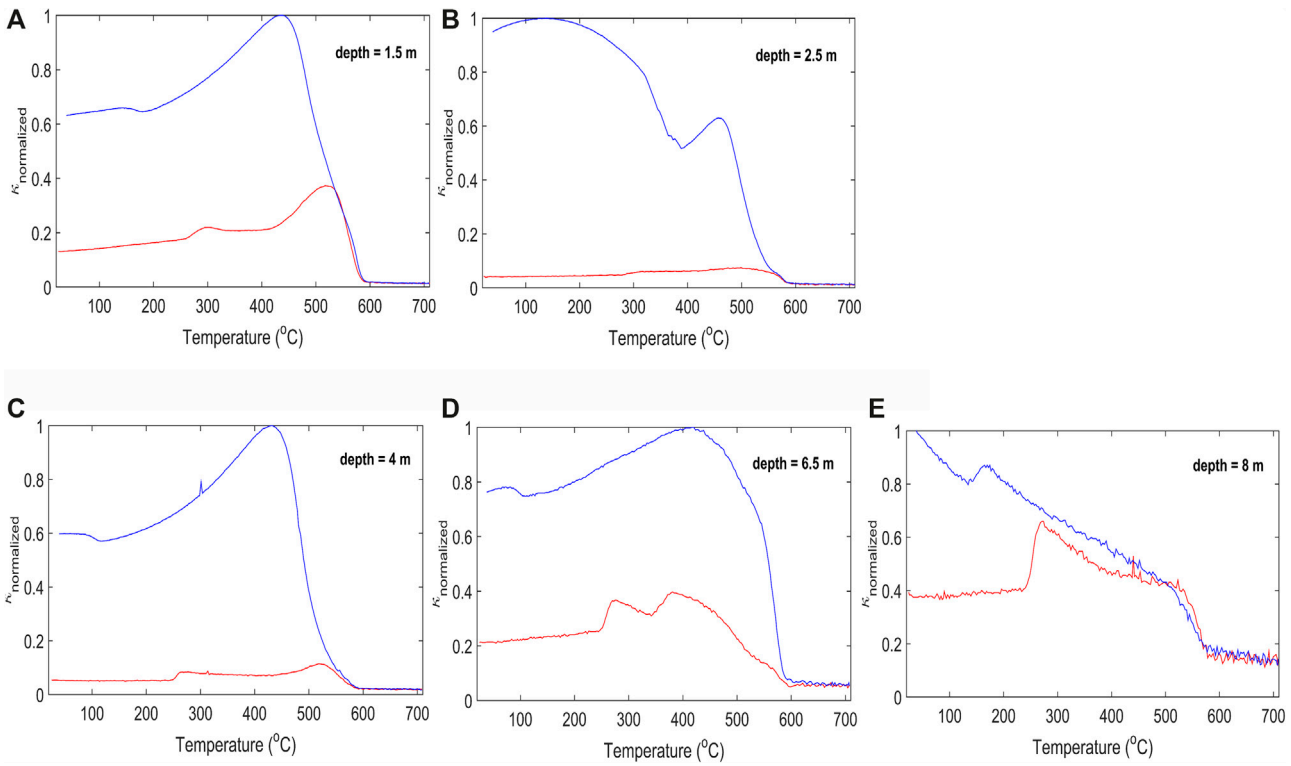

FIGURE 2 | Magnetic susceptibility changes with temperature for samples collected at 1.5, 2.5, 4, 6.5 and 8 m, during sample heating (red) and cooling (blue). The samples are representative of the anthropogenic deposits **(A–C)** and the Quaternary sediments (organic **(D–E)**. The different values of susceptibility measured when comparing the heating and cooling curves reveal mineralogical transformations caused by dehydration or change in the sample redox state in the heating process.

carriers is obtained by η/ρ. The moment of dipole of the particle is such that $\mu = v\sigma_S$ where σ_S is the magnetization saturation for the magnetic carrier. The SPCDM procedure isolates the superparamagnetic contribution $M(B_i, T)$ by applying a set of external fields $B_i\,(i = 1 : 17)$ B_i ranging from 5 to 340 mT, by using a precise MicroMag3900 magnetometer, at USPMAG (University of São Paulo). These magnetization values provide unknown parameters (M_S, μ) from which estimates about particle concentration $(\eta = M_S/\mu)$ and particle volume $(v = \mu/\sigma_S)$ can be achieved. For volume estimates, the magnetization of pure magnetite can be assumed in most cases. In summary, the SPCDM provides saturation magnetization (M_S), the particle moment of dipole μ and, from these, particle concentration η $[m^{-3}]$ and grain volume v, if saturation magnetization σ_S for mineral carrier is known.

RESULTS AND DISCUSSION

The thermomagnetic measurements presented in **Figure 2** served as a preliminary analysis to identify the magnetic mineralogy diversity at the site. All heating curves captured the magnetic susceptibility increase above 250–300 °C, indicating transformations of iron (hydr)oxides under a reducing atmosphere (Hanesch et al., 2006). While heating, the magnetic susceptibility increases with temperature to around 400–580 °C, followed by a significant loss of magnetization, indicating the occurrence of magnetite. The magnetic susceptibility increase indicates transformations of paramagnetic or clay minerals into magnetite (Roberts, 2015).

It is possible that ferrihydrite is being converted to magnetite, a common product of bacterial Fe(III) hydroxide reduction. The precipitation of magnetite in ferrihydrite reduction by dissimilatory Fe(III)-reducing microorganisms has been reported by several studies, (e.g. Lovley et al., 1987; Vali et al., 2004; Coker et al., 2008; Zhuang et al., 2015).

Even though magnetite is visible in the irreversible thermomagnetic curves, the presence of magnetite in the soils, prior the transformation of ferrihydrite into magnetite is verified in the FORC diagrams. **Figure 3A**) shows a clear SD-like behavior on 2.5 m (anthropogenic sediments) with small asymmetrical spread (higher towards the positive area) in the *Bu* axis, peaking around zero, indicating little to no magnetic interaction. The coercivity distribution peak in *Bc* is around 20 mT, evidence of magnetite, in accordance to the thermomagnetic curves. **Figure 3B**) shows the FORC diagram from the sample collected at 6 m (Quaternary sediments). A maximum coercivity peak close to the origin at around 5mT indicates a prevalent reversible component of magnetization (Sagnotti and Winkler, 2012), with open contours diverging asymmetrically on the *Bu* axis, showing resemblance to SP dominated population of

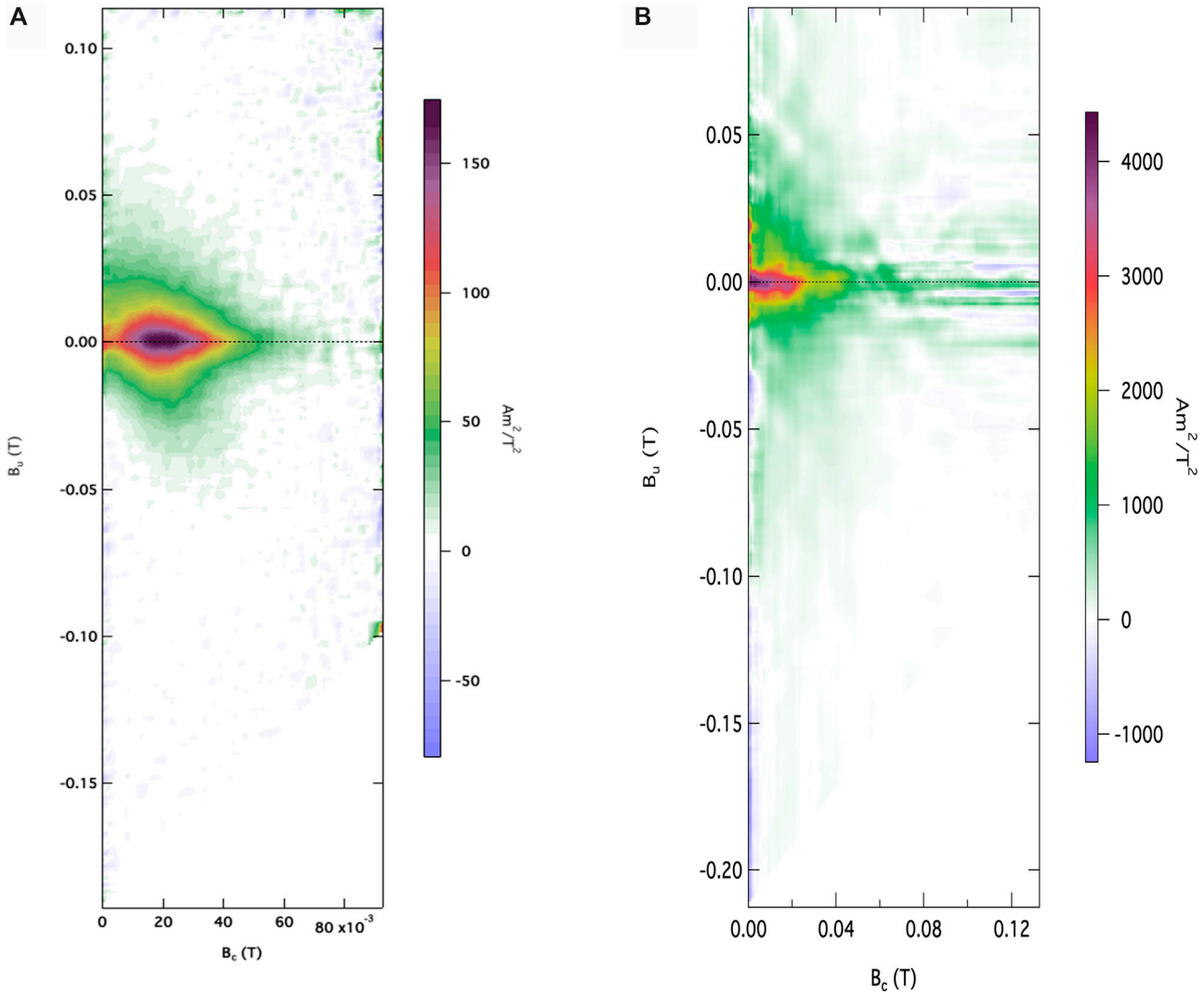

FIGURE 3 | FORC distribution of sample collected at **(A)** 2.5 m (anthropogenic deposit sediments) and **(B)** 6.0 m (Quaternary sediments). At 2.5 m the contours present small asymmetrical spread in the *Bu* axis, with a peak around zero, indicating single domain behavior with little to no magnetic interaction. The coercivity distribution peak in *Bc* around 20 mT is evidence of magnetite. At 6.0 m, open contours diverging asymmetrically on the *Bu* axis indicate dominance of SP population of grains.

grains (Roberts et al., 2014). The FORC also shows strong interaction fields (*Bu*) spreading until coercivities of 40 mT.

Samples collected at depths of 2.5 and 8 m were submitted to hysteresis cycles taken at distinct temperatures (**Figures 4A–C**, respectively). Below room temperature, the magnetization processes are irreversible and produces the ferromagnetic hysteresis loop. However, **Figures 4A,B** (2.5 m) and (8.0 m) capture the magnetic carrier's inabilities to sustain magnetization at room temperature (300 K, also shown as insets graphs), producing a superparamagnetic response of the sigmoidal shape of a ferromagnetic response, but losing the loop.

With evidence of SP-SSD particles in the magnetic particles assemblages, quantitative interpretation techniques based on the SP-SSD magnetic response were applied (see **Supplementary material** for individual FDS and SPCDM analysis). **Figure 5** shows the depth profiles of the measured magnetic susceptibility, F_t^{-1} obtained from FDS measurements and superparamagnetic particles concentration, η. Magnetic susceptibility measurements (**Figure 5A**) show that the shallower portion of the soil is more magnetic and MS decreases with depth. The high MS in the uppermost 2.5 m is attributed to the unsaturated sediments magnetic properties. The maximum value of magnetic susceptibility is observed at 2.5 m, a known zone of gas pocket. Even though magnetic susceptibility decreases with depth, around 6.5 m it increases again, at a depth coincident with the second gas pocket zone. The parameter F_t^{-1}

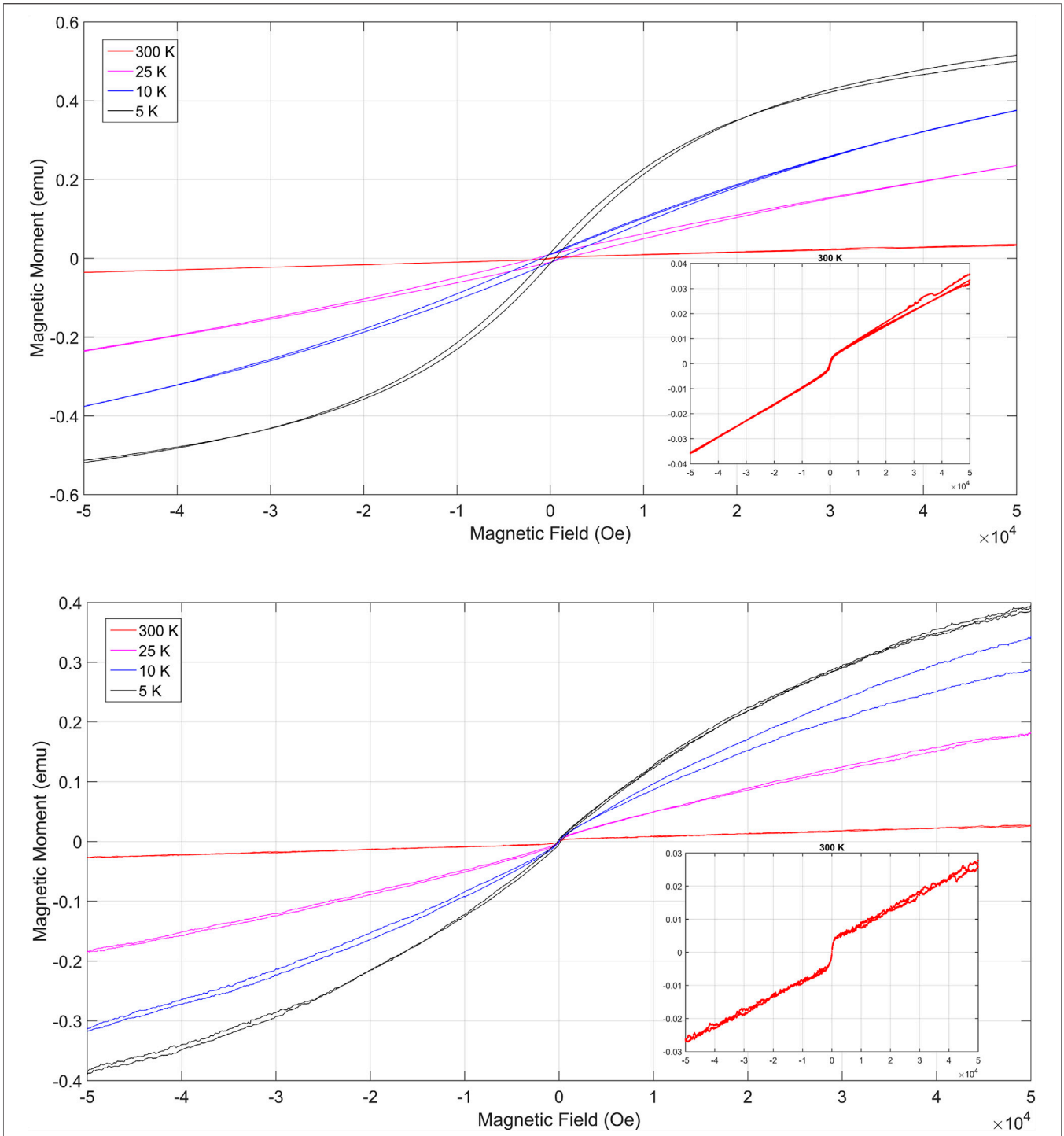

FIGURE 4 | Hysteresis cycles at distinct temperatures: **(A)** 2.5 m and **(B)** 8 m. The samples are representative of the anthropogenic deposits **(A)** and Quaternary sediments **(B)**. Inset graphs show in detail the measurements at room temperature. The ferromagnetic behavior is observed bellow room temperature. The superparamagnetic response is observed in **(A)** as a sigmoidal shape of a ferromagnetic response with no loop. This fingerprint is not visible in the hysteresis cycle in **(B)**.

(**Figure 5B**), an estimation of the SP-SSD size variations, reveals that magnetic particles present a more significant frequency effect at 4.5 and 6.5 m. We interpret that magnetic carriers size variations in the SP-SSD threshold are more significant at these two depths, which is at the boundary of the second gas pocket zone. The superparamagnetic particles concentration (SP concentration) profile (**Figure 5C**) shows two peaks, which agree with the gas pockets depths (0.5–2.5, 5–6 and 10.5 m).

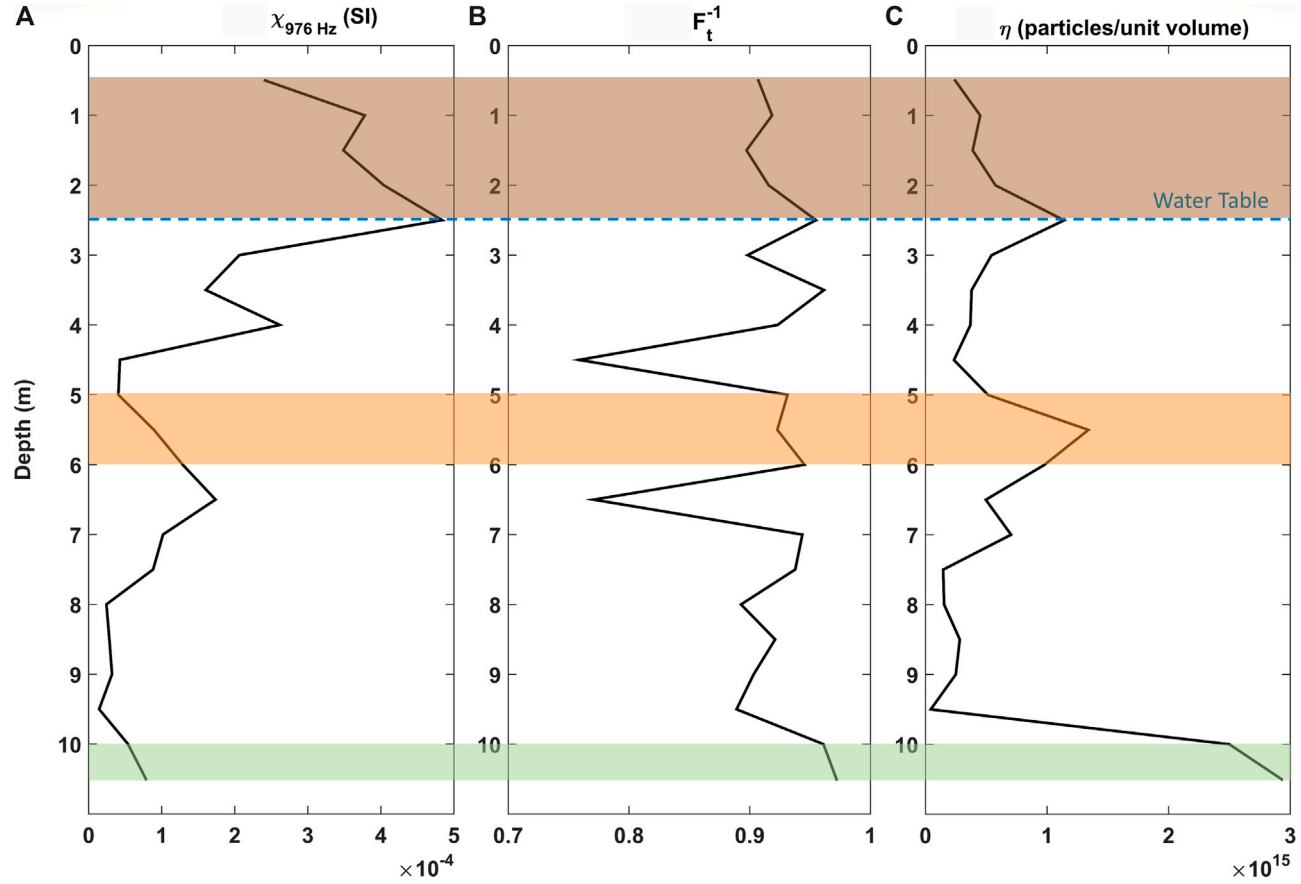

FIGURE 5 | Interpretation parameters: **(A)** Magnetic susceptibility, χ, **(B)** transition parameter, F_t^{-1} and **(C)** concentration of superparamagnetic particles, η. The gas pockets depths are highlighted in brown, orange and green. χ show a more magnetic soil at the vadone zone (depth <2.5 m). F_t^{-1} indicates highest variations of magnetic particle sizes in the SP-SSD threshold at the boundaries of the second gas pocket zone (4.5 and 6.5 m). η is higher in the gas pockets depths than in the rest of core samples.

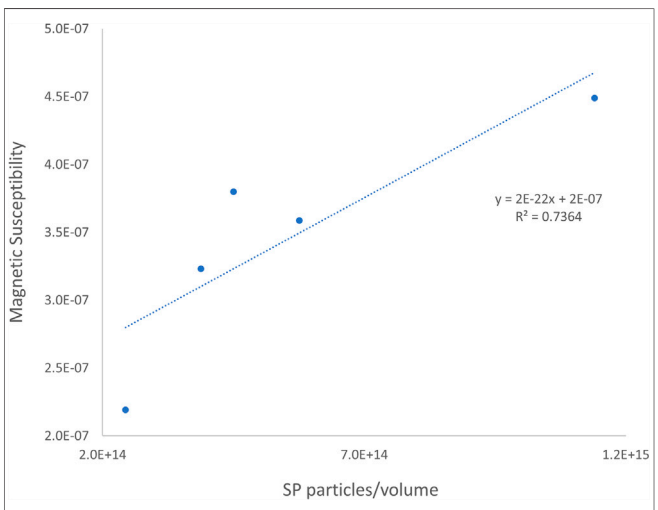

FIGURE 6 | Linear correlation between magnetic susceptibility and SP particles content, for the samples from the vadose zone.

The high MS values are not always in agreement with high SP particles shown by η, demonstrating that increasing content of SP ferrimagnetic particles alone cannot account for the variations of magnetic susceptibility of all samples. This apparent contradiction results from the limitations of both the FDS and the SPCDM methods. The FDS method captures a relaxation from magnetic particles within the SP-SSD threshold, in the 976–15,616 Hz AC field frequency range. On the other hand, the SPCDM captures faster relaxations, which are produced by finer particles (higher relaxation frequencies).

In this study, both methods were complementary, delimiting a zone of increasing the abundance SP-SSD particles (high F_t^{-1} and low η) and a zone of mostly SP particles (low F_t^{-1} and high η).

In the unsaturated zone, from 0.5 to 2.5 m, we believe that superparamagnetic particles are formed in a different process that will not be discussed in this work, where the grain size is not affected. The linear correlation between MS and η shown in **Figure 6** evidence that η follows the same pattern as

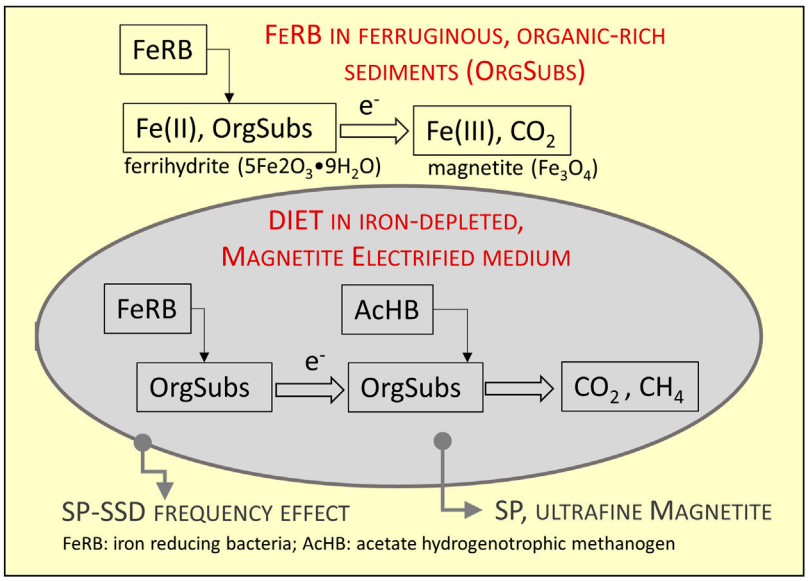

FIGURE 7 | Conceptual model illustrating the magnetic signatures observed across the methane pockets. The transformation of ferrihydrite into magnetite by iron reducing bacteria and the electron transfer to methanogens archaea. The DIET zone in this case is identified by a region of high SP content, surrounded by coarser particles within the SP-SSD threshold.

magnetic susceptibility within this anthropogenic layer, suggesting the magnetic response of this portion is dominated by the superparamagnetic particles. F_t^{-1} closer to one supports the interpretation that these depths are dominated by the superparamagnetic particles. When superparamagnetic particles are predominant, they dominate the susceptibility and SPCDM signals, but the frequency effect is little because there are little variations of the grain size distribution of the sample. In terms of bio-precipitation, this may be reflecting that most of the Fe-bearing particles are being used by microorganisms.

Even though magnetic signatures are a result of the magnetic grain sizes, this investigation approach does not aim to estimate the magnetic grain sizes and rather seek for these grains fingerprints. Moreover, the complex history of the site reminds us to expect an assemblage of grain sizes. This aspect enhances the usefulness of our quantitative interpretation procedures, which isolates and quantifies the ultrafine content.

In general, the distribution of SP minerals correlates well with the detected methanogens, suggesting that the SP particles of magnetite at these depths are anaerobically produced by iron-reducing dissimilatory microorganisms such as, *Geobacter* and *Geothrix*. There may be further syntrophy with methanogens such as *Methanosaeta* where Geobacter can further be involved in the DIET mechanism. Microbial analysis (**Figure 1**) supports the hypothesis of DIET as the methane producing mechanism at depths where superparamagnetic particles achieve highest concentrations. We propose a conceptual model of magnetic particles size range associated with the DIET hypothesis. **Figure 7** illustrates the transformation of ferrihydrite into magnetite by iron reducing bacteria and the electron transfer to methanogens archaea. The DIET zone in this case is identified by a region of high SP content, surrounded by coarser particles within the SP-SSD threshold.

Other non-DIET reactions with Fe(III) reducing bacteria such as *Geothrix* with may also have a role in the production of magnetite (Klueglein et al., 2013) and there may be some syntrophy with *Methanosaeta* (Sutcliffe et al., 2018).

CONCLUSION

Magnetic properties measurements revealed the ultrafine magnetic particles occurrence in a brownfield site. The distribution of superparamagnetic concentration correlates well with the detected methanogens in gas pockets, suggesting that the microbial activity producing methane is producing these ultrafine particles, different from the magnetic particles produced at other depths. The results presented here support the use of environmental magnetism techniques to investigate biogeochemical processes of anaerobic microbial activity. Possibly, this kind of superparamagnetic fingerprint can be found in non-active methanogenic basins but recorded by magnetic mineralogy once preserved.

DATA AVAILABILITY STATEMENT

The raw data supporting the conclusions of this article will be made available by the authors, without undue reservation.

AUTHOR CONTRIBUTIONS

AU conducted the magnetic susceptibility measurements (frequency and temperature dependence), and conducted the multi-frequency analysis. AU has been studing the site for many years and for this study she planned the magnetic investigation and interpreted the results with the co-authors. CA was the project's PI and contributed discussing the results and writing/revising many parts of the manuscript. AL conducted the magnetizations decay and FORCs and MR conducted the hysteresis measurements. FORC and hysteresis were also supervised and discussed with MM. GT, an undergraduate student, conducted the thermomagnetic measurements. RD participated in the research at the site colaborating with the microbiological analysis. The results were discussed with all co-authors, who also wrote/revised the manuscript.

ACKNOWLEDGMENTS

The authors thank FAPESP (grant # 2013/22912) and CNRS (project NanoEnvi-GET). We would like to acknowledge the laboratories where measurements were taken: USPMAG for thermomagnetic and time-dependent IRM, Institut National des Sciences Appliquées (INSA)—Toulouse for hysteresis, Institut de Physique du Globe de Paris for FORC and LabCore for frequency dependence susceptibility (Oceanography Institute, University of São Paulo).

SUPPLEMENTARY MATERIAL

The Supplementary Material for this article can be found online at: https://www.frontiersin.org/articles/10.3389/feart.2020.608387/full#supplementary-material.

REFERENCES

Bryant, M. P., Wolin, E. A., Wolin, M. J., and Wolfe, R. S. (1967). Methanobacillus omelianskii, a symbiotic association of two species of bacteria. *Arch. Mikrobiol.* 59, 20–31. doi:10.1007/BF00406313

Byrne, J. M., Klueglein, N., Pearce, C., Rosso, K. M., Appel, E., and Kappler, A. (2015). Redox cycling of Fe(II) and Fe(III) in magnetite by Fe-metabolizing bacteria. *Science* 347, 1473–1476. doi:10.1126/science.aaa4834

Chen, S., Rotaru, A. E., Liu, F., Philips, J., Woodard, T. L., Nevin, K. P., et al. (2014b). Carbon cloth stimulates direct interspecies electron transfer in syntrophic co-cultures. *Bioresour. Technol.* 173, 82–86. doi:10.1016/j.biortech.2014.09.009

Chen, S., Rotaru, A. E., Shrestha, P. M., Malvankar, N. S., Liu, F., Fan, W., et al. (2014a). Promoting interspecies electron transfer with biochar. *Sci. Rep.* 4, 5019. doi:10.1038/srep05019

Christensen, T. R. (2010). *Wetlands in methane and climate change*. London, United Kingdom: Earthscan Ltd.

Coker, V. S., Bell, A. M. T., Pearce, C. I., Pattrick, R. A. D., Van der Laan, G., and Lloyd, J. R. (2008). Time-resolved synchrotron powder X-ray diffraction study of magnetite formation by the Fe(III)-reducing bacterium Geobacter sulfurreducens. *Am. Mineral.* 93 (4), 540–547. doi:10.2138/am.2008.2467

Dormann, J. L., D'Orazio, F., Lucari, F., Tronc, E., Prené, P., Jolivet, J. P., et al. (1996). Thermal variation of the relaxation time of the magnetic moment of gamma -Fe2O3 nanoparticles with interparticle interactions of various strengths. *Phys. Rev. B Condens. Matter.* 53 (21), 14291. doi:10.1103/physrevb.53.14291

Dunlop and Özdemir, D. J. O. (2001). *Rock magnetism: fundamentals and Frontiers*. Cambridge Univ. Press.

Hanesch, M., Stanjek, H., and Petersen, N. (2006). Thermomagnetic measurements of soil iron minerals: the role of organic carbon. *Geophys. J. Int.* 165, 53–61. doi:10.1111/j.1365-246x.2006.02933.x

Kato, S., Hashimoto, K., and Watanabe, K. (2012). Microbial interspecies electron transfer via electric currents through conductive minerals. *Proc. Natl. Acad. Sci. U.S.A.* 109, 10042–10046. doi:10.1073/pnas.1117592109

Klueglein, N., Lösekann-Behrens, T., Obst, M., Behrens, S., Appel, E., and Kappler, A. (2013). Magnetite formation by the novel Fe(III)-reducingGeothrix fermentansStrain HradG1 isolated from a hydrocarbon-contaminated sediment with increased magnetic susceptibility. *Geomicrobiol. J.* 30, 863–873. doi:10.1080/01490451.2013.790922

Lee, J., Hwang, B., Koo, T., Shin, S. G., Kim, W., and Hwang, S. (2014). Temporal variation in methanogen communities of four different full-scale anaerobic digesters treating food waste-recycling wastewater. *Bioresour. Technol.* 168 (3), 59–63. doi:10.1016/j.biortech.2014.03.161

Lee, J. H., Roh, Y., and Hur, H. G. (2008). Microbial production and characterization of superparamagnetic magnetite nanoparticles by Shewanella sp. HN-41. *J. Microbiol. Biotechnol.* 18, 1572–1577.

Leite, A. S., Mendonça, C. A., Moraes, P. L. A., and Ustra, A. T. (2018). A procedure for quantitative characterization of superparamagnetic minerals in environmental magnetism. *Geophys. J. Int.* 215 (3), 1974–1984. doi:10.1093/gji/ggy395

Li, Y., Zhang, H., Tu, C., and Luo, Y. (2018). Magnetic characterization of distinct soil layers and its implications for environmental changes in the coastal soils from the yellow river delta. *Catena* 162, 245–254. doi:10.1016/j.catena.2017.11.006

Liu, F., Rotaru, A. E., Shrestha, P. M., Malvankar, N. S., Nevin, K. P., and Lovley, D. R. (2015). Magnetite compensates for the lack of a pilin-associated c-type cytochrome in extracellular electron exchange. *Environ. Microbiol.* 17, 648–655. doi:10.1111/1462-2920.12485

Liu, F., Rotaru, A.-E., Shrestha, P. M., Malvankar, N. S., Nevin, K. P., and Lovley, D. R. (2012). Promoting direct interspecies electron transfer with activated carbon. *Energy Environ. Sci.* 5, 8982. doi:10.1039/c2ee22459c

Lovley, D. R., Stolz, J. F., Nord, G. L., and Phillips, E. J. P. (1987). Anaerobic production of magnetite by a dissimilatory iron-reducing microorganism. *Nature* 330, 252–254. doi:10.1038/330252a0

Lovley, D. R. (1991). "Magnetite formation during microbial dissimilatory iron reduction," in *Iron biominerals*. Editors R. B. Frankel and R. P. Blakemore (Berlin, Germany: Springer), 151–166. doi:10.1007/978-1-4615-3810-3_11

Lovley, D. R., Holmes, D. E., and Nevin, K. P. (2004). Dissimilatory Fe(III) and Mn(IV) reduction. *Adv. Microb. Physiol.* 49, 219–286. doi:10.1016/S0065-2911(04)49005-5

Lovley, D. R. (2011). Live wires: direct extracellular electron exchange for bioenergy and the bioremediation of energy-related contamination. *Energy Environ. Sci.* 4, 4896–4906. doi:10.1039/c1ee02229f

Lovley, D. R. (2017). Syntrophy goes electric: direct interspecies electron transfer. *Annu. Rev. Microbiol.* 71, 643–664. doi:10.1146/annurev-micro-030117-020420

Maher, B. A., and Taylor, R. M. (1988). Formation of ultrafine-grained magnetite in soils. *Nature* 336, 368–370. doi:10.1038/336368a0

Martins, G., Salvador, A. F., Pereira, L., and Alves, M. M. (2018). Methane production and conductive materials: a critical review. *Environ. Sci. Technol.* 52 (18), 10241–10253. doi:10.1021/acs.est.8b01913

Mendonça, C. A., Doherty, R., Fornaro, A., Abreu, E. L., Novaes, G. C., Fachin, S. J. S., et al. (2015a). Integrated earth resistivity tomography (ERT) and multilevel sampling gas: a tool to map geogenic and anthropogenic methane accumulation on brownfield sites. *Environ Earth Sci.* 74, 1217–1226. doi:10.1007/s12665-015-4111-6

Mendonça, C. A., Doherty, R., Amaral, N. D., McPolin, B., Larkin, M. J., and Ustra, A. (2015b). Resistivity and induced polarization monitoring with microbial ecology of biogas dynamics on a brownfield site. *Inter* 4 (3), SAB43–SAB56. doi:10.1190/INT-2015-0057.1

Moskowitz, B. M., Frankel, R. B., and Bazylinski, D. A. (1993). Rock magnetic criteria for the detection of biogenic magnetite. *Earth Planet Sci. Lett.* 120, 283–300. doi:10.1016/0012-821x(93)90245-5

Özdemir, Ö., and Dunlop, D. J. (2014). Hysteresis and coercivity of hematite. *J. Geophys. Res. Solid Earth* 119, 2582–2594. doi:10.1002/2013jb010739

Pike, C. R., Roberts, A. P., and Verosub, K. L. (1999). Characterizing interactions in fine magnetic particle systems using first order reversal curves. *J. Appl. Phys.* 85, 6660–6667. doi:10.1063/1.370176

Pike, C. R., Roberts, A. P., and Verosub, K. L. (2001). First-order reversal curve diagrams and thermal relaxation effects in magnetic particles. *Geophys. J. Int.* 145, 721–730. doi:10.1046/j.0956-540x.2001.01419.x

Roberts, A. P., Heslop, D., Zhao, X., and Pike, C. R. (2014). Understanding fine magnetic particle systems through use of first-order reversal curve diagrams. *Rev. Geophys.* 52 (4), 557–602. doi:10.1002/2014rg000462

Roberts, A. P. (2015). Magnetic mineral diagenesis. *Earth Sci. Rev.* 151, 1–47. doi:10.1016/j.earscirev.2015.09.010

Roberts, A. P., Pike, C. R., and Verosub, K. L. (2000). FORC diagrams: anew tool for characterizing the magnetic properties of natural samples. *J. Geophys. Res.* 105 (28), 461–475 .doi:10.1029/2000jb900326

Rotaru, A.-E., Shrestha, P. M., Liu, F., Shrestha, M., Shrestha, D., Embree, M., et al. (2014b). A new model for electron flow during anaerobic digestion: direct interspecies electron transfer to Methanosaeta for the reduction of carbon dioxide to methane. *Energy Environ. Sci.* 7, 408–415. doi:10.1039/c3ee42189a

Rotaru, A. E., Calabrese, F., Stryhanyuk, H., Musat, F., Shrestha, P. M., Weber, H. S., et al. (2018). Conductive particles enable syntrophic acetate oxidation between Geobacter and Methanosarcina from coastal sediments. *mBio* 9, e00226–18. doi:10.1128/mBio.00226-18

Rotaru, A. E., Shrestha, P. M., Liu, F., Markovaite, B., Chen, S., Nevin, K. P., et al. (2014a). Direct interspecies electron transfer between Geobacter metallireducens and Methanosarcina barkeri. *Appl. Environ. Microbiol.* 80, 4599–4605. doi:10.1128/AEM.00895-14

Sagnotti, L., and Winkler, A. (2012). On the magnetic characterization and quantification of the superparamagnetic fraction of traffic-related urban airborne PM in Rome, Italy. *Atmos. Environ.* 59, 131–140. doi:10.1016/j.atmosenv.2012.04.058

Shrestha, P. M., Rotaru, A. E., Aklujkar, M., Liu, F., Shrestha, M., Summers, Z. M., et al. (2013b). Syntrophic growth with direct interspecies electron transfer as the primary mechanism for energy exchange. *Environ Microbiol Rep.*, 5, 904–910. doi:10.1111/1758-2229.12093

Shrestha, P. M., Rotaru, A. E., Summers, Z. M., Shrestha, M., Liu, F., and Lovley, D. R. (2013a). Transcriptomic and genetic analysis of direct interspecies electron transfer. *Appl. Environ. Microbiol.* 79, 2397–2404. doi:10.1128/AEM.03837-12

Sieber, J. R., McInerney, M. J., and Gunsalus, R. P. (2012). Genomic insights into syntrophy: the paradigm for anaerobic metabolic cooperation. *Annu. Rev. Microbiol.* 66, 429–452. doi:10.1146/annurev-micro-090110-102844

Stams, A. J., and Plugge, C. M. (2009). Electron transfer in syntrophic communities of anaerobic bacteria and archaea. *Nat. Rev. Microbiol.* 7, 568–577. doi:10.1038/nrmicro2166

Summers, Z. M., Fogarty, H. E., Leang, C., Franks, A. E., Malvankar, N. S., and Lovley, D. R. (2010). Direct exchange of electrons within aggregates of an evolved syntrophic coculture of anaerobic bacteria. *Science* 330, 1413–1415. doi:10.1126/science.1196526

Sutcliffe, B., Chariton, A. A., Harford, A. J., Hose, G. C., Stephenson, S., Greenfield, P., et al. (2018). Insights from the genomes of microbes thriving in uranium-enriched sediments. *Microb. Ecol.* 75, 970–984. doi:10.1007/s00248-017-1102-z

Tauxe, L., Bertram, H. N., and Seberino, C. (2002). Physical interpretation of hysteresis loops: micromagnetic modeling of fine particle magnetite. *G-cubed* 3 (10), 1–22. doi:10.1029/2001gc000241

Tauxe, L., Pick, T., and Constable, C. (1996). Wasp-waists, pot-bellies, and superparamagnetism. *Journal of Geophysical Research B: Solid Earth* 101 (95), 571–583. doi:10.1029/95jb03041

Ustra, A., Mendonça, C. A., Leite, A., Jovane, L., and Trindade, R. I. F. (2018). Quantitative interpretation of the magnetic susceptibility frequency dependence. *Geophys. J. Int.* 213 (2), 805–814. doi:10.1093/gji/ggy007

Ustra, A., Mendonça, C., Leite, A., Jaqueto, P., and Novello, V. F. (2019). Low field frequency dependent magnetic susceptibility inversion. *Comput. Geosci.* 133, 104326. doi:10.1016/j.cageo.2019.104326

Vali, H., Weiss, B., Li, Y. L., Sears, S. K., Kim, S. S., Kirschvink, J. L., et al. (2004). Formation of tabular single-domain magnetite induced by Geobacter metallireducens GS-15. *Proc. Natl. Acad. Sci. U.S.A.* 101 (46), 16121–16126. doi:10.1073/pnas.0404040101

Wang, L. Y., Nevin, K. P., Woodard, T. L., Mu, B. Z., and Lovley, D. R. (2016). Expanding the diet for DIET: electron donors supporting direct interspecies electron transfer (DIET) in defined co-cultures. *Front. Microbiol.* 7, 236. doi:10.3389/fmicb.2016.00236

Worm, H.-U. (1999). Time-dependent IRM: a new technique for magnetic granulometry. *Geophys. Res. Lett.* 26 (16), 2557–2560. doi:10.1029/1999gl008360

Xiao, L., Liu, F., Liu, J., Li, J., Zhang, Y., Yu, J., et al. (2018). Nano-Fe3O4 particles accelerating electromethanogenesis on an hour-long timescale in wetland soil. *Environ. Sci. Nano* 5, 436–445. doi:10.1039/C7EN00577F

Xiao, L., Wei, W., Luo, M., Xu, H., Feng, D., Yu, J., et al. (2019). A potential contribution of a Fe(III)-rich red clay horizon to methane release: biogenetic magnetite-mediated methanogenesis. *Catena* 181, 104081. doi:10.1016/j.catena.2019.104081

Zhang, J., and Lu, Y. (2016). Conductive Fe3O4 nanoparticles accelerate syntrophic methane production from butyrate oxidation in two different lake sediments. *Front. Microbiol.* 7, 1316. doi:10.3389/fmicb.2016.01316

Zhao, Z., Li, Y., Yu, Q., and Zhang, Y. (2018). Ferroferric oxide triggered possible direct interspecies electron transfer between Syntrophomonas and Methanosaeta to enhance waste activated sludge anaerobic digestion. *Bioresour. Technol.* 250, 79–85. doi:10.1016/j.biortech.2017.11.003

Zhuang, L., Xu, J., Tang, J., and Zhou, S. (2015). Effect of ferrihydrite biomineralization on methanogenesis in an anaerobic incubation from paddy soil. *J. Geophys. Res. Biogeosci.* 120, 876–886. doi:10.1002/2014jg002893

Conflict of Interest: The authors declare that the research was conducted in the absence of any commercial or financial relationships that could be construed as a potential conflict of interest.

frontiers in Earth Science

ORIGINAL RESEARCH
published: 15 March 2021
doi: 10.3389/feart.2021.598172

Methanogens and Their Syntrophic Partners Dominate Zones of Enhanced Magnetic Susceptibility at a Petroleum Contaminated Site

*Carol L. Beaver[1], Estella A. Atekwana[2], Barbara A. Bekins[3], Dimitrios Ntarlagiannis[4], Lee D. Slater[4] and Silvia Rossbach[1]**

[1] Department of Biological Sciences, Western Michigan University, Kalamazoo, MI, United States, [2] Department of Earth Sciences, University of Delaware, Newark, DE, United States, [3] U. S. Geological Survey, Menlo Park, CA, United States, [4] Earth and Environmental Sciences, Rutgers University–Newark, Newark, NJ, United States

OPEN ACCESS

Edited by:
Alexandra Abrajevitch, Institute of Tectonics and Geophysics Named After Y. A. Kosygin (RAS), Russia

Reviewed by:
Nicole Dopffel, Norwegian Research Institute (NORCE), Norway
Oscar Pueyo Anchuela, University of Zaragoza, Spain
Yuki Morono, Japan Agency for Marine-Earth Science and Technology (JAMSTEC), Japan

***Correspondence:**
Silvia Rossbach
silvia.rossbach@wmich.edu

Specialty section:
This article was submitted to Geomagnetism and Paleomagnetism, a section of the journal Frontiers in Earth Science

Received: 24 August 2020
Accepted: 22 February 2021
Published: 15 March 2021

Citation:
Beaver CL, Atekwana EA, Bekins BA, Ntarlagiannis D, Slater LD and Rossbach S (2021) Methanogens and Their Syntrophic Partners Dominate Zones of Enhanced Magnetic Susceptibility at a Petroleum Contaminated Site. Front. Earth Sci. 9:598172. doi: 10.3389/feart.2021.598172

Geophysical investigations documenting enhanced magnetic susceptibility (MS) within the water table fluctuation zone at hydrocarbon contaminated sites suggest that MS can be used as a proxy for investigating microbial mediated iron reduction during intrinsic bioremediation. Here, we investigated the microbial community composition over a 5-year period at a hydrocarbon-contaminated site that exhibited transient elevated MS responses. Our objective was to determine the key microbial populations in zones of elevated MS. We retrieved sediment cores from the petroleum-contaminated site near Bemidji, MN, United States, and performed MS measurements on these cores. We also characterized the microbial community composition by high-throughput 16S rRNA gene amplicon sequencing from samples collected along the complete core length. Our spatial and temporal analysis revealed that the microbial community composition was generally stable throughout the period of investigation. In addition, we observed distinct vertical redox zonations extending from the upper vadose zone into the saturated zone. These distinct redox zonations were concomitant with the dominant microbial metabolic processes as follows: (1) the upper vadose zone was dominated by aerobic microbial populations; (2) the lower vadose zone was dominated by methanotrophic populations, iron reducers and iron oxidizers; (3) the smear zone was dominated by iron reducers; and (4) the free product zone was dominated by syntrophic and methanogenic populations. Although the common notion is that high MS values are caused by high magnetite concentrations that can be biotically formed through the activities of iron-reducing bacteria, here we show that the highest magnetic susceptibilities were measured in the free-phase petroleum zone, where a methanogenic community was predominant. This field study may contribute to the emerging knowledge that methanogens can switch their metabolism from methanogenesis to iron reduction with associated magnetite precipitation in hydrocarbon contaminated sediments. Thus, geophysical methods such as MS may help to identify zones where iron cycling/reduction by methanogens is occurring.

Keywords: hydrocarbon degradation, magnetic susceptibility, methanogenesis, iron reduction, petroleum contamination, *Smithella*

INTRODUCTION

Magnetic susceptibility (MS) is a measure of the ability of a material to become magnetized when placed in a magnetic field and is dependent on the concentration and type of the magnetic minerals present. It generally reflects the presence and volume of the iron oxide magnetite. Because of the abundance of iron in terrestrial environments, MS is commonly used to investigate different geological processes. Example applications of MS include: (1) determining the magnetic stratigraphy in loess deposits, lake sediments and marine sediments to reconstruct the paleoenvironmental evolution and erosional history (e.g., Zhang et al., 2012), (2) examining variations in the detrital input of magnetic minerals related to climate change (e.g., Da Silva et al., 2013), (3) aiding archeological investigations (Walach et al., 2011), (4) serving as a proxy for extreme hydrologic events and rainfall (Li et al., 2019), (5) monitoring soil pollution (Hoffmann et al., 1999; D'Emilio et al., 2007; Zhang et al., 2012), and (6) investigating the movement of tectonic plates. Further, the MS technique has also been used for oil exploration (e.g., Guzmán et al., 2011), for evaluation of oil bearing units (Perez-Perez et al., 2011; Emmerton et al., 2013) and reservoir properties (Potter, 2007; Potter and Ivakhnenko, 2008).

There is also a growing interest in relating environmental magnetic studies to microbial mediated iron cycling (Porsch et al., 2010; Mewafy et al., 2011; Byrne et al., 2015), and oil biodegradation after spills (Rijal et al., 2010, 2012; Atekwana et al., 2014; Beaver et al., 2016; Lund et al., 2017). In particular, Rijal et al. (2010, 2012) and Atekwana et al. (2014) observed large MS anomalies within the water table fluctuation zone (WTFZ) associated with the presence of hydrocarbons relative to background measurements and related these changes to the precipitation of magnetite resulting from microbial degradation of the hydrocarbons by iron-reducing bacteria.

Biodegradation is a natural process performed by microbes that is dependent on the terminal electron acceptors (TEAs) available in the environment (Meckenstock et al., 2015). Oil degradation using aerobic respiration provides microbes with the most energy, but oxygen is eventually exhausted and sediments turn anoxic. After oxygen is depleted, microbial communities switch to different TEAs. Nitrate reduction is the next most energetically favorable process. When nitrate is used up, iron reduction occurs. After Fe(III) is depleted, sulfate reduction and finally fermentation and methanogenesis will take over as predominant microbial processes. To produce methane, methanogens can use methylated compounds such as acetate or methanol as substrates or just carbon dioxide (CO_2) and hydrogen gas (H_2). In fact, the methanogens' use of H_2 leads to a locally very low hydrogen partial pressure, making hydrocarbon fermentation energetically favorable. This interspecies hydrogen transfer represents a syntrophic relationship between fermenters and methanogens. In other syntrophic associations between respiratory bacteria and methanogens, electrons are transferred via certain bacterial appendages such as nanowires (direct interspecies electron transfer – DIET) (Cruz Viggi et al., 2014; Rotaru et al., 2014; Zhuang et al., 2015).

Magnetite is often found in sediments where iron reduction has occurred. When the activity of iron-reducing bacteria increases the local concentration of Fe(II), Fe(II) will sorb to ferrihydrite, causing the precipitation of the mixed valent magnetite (Hansel et al., 2005).

$$Fe^{2+} + 2Fe^{3+} + 4H_2O \rightarrow Fe_3O_4 + 8H^+$$

Therefore an increase in MS can indicate if iron-reducing microorganisms are active while degrading hydrocarbons (Porsch et al., 2010).

Nonetheless the relationship between MS and the activity of iron-reducing bacteria is not completely understood and the use of MS as a proxy for biodegradation is tenuous at best. This is underscored by the observation that the MS signature can be transient due to the creation and destruction of magnetic minerals by biotic and abiotic processes (e.g., Ameen et al., 2014; Lund et al., 2017). Some of these magnetic minerals may be used by microbes to transfer electrons, causing changes in mineral structure. Redox cycling using magnetite by *Rhodopseudomonas*, an iron oxidizer, and *Geobacter*, an iron reducer, has been demonstrated under laboratory conditions, and MS was shown to decrease during the oxidation phase from Fe dissolution and increase during the reduction phase from magnetite precipitation (Byrne et al., 2015). In the field, Rijal et al. (2012) and Ameen et al. (2014) documented temporal decreases in MS at a contaminated former military air force base in Hradčany, Czech Republic, and speculated this to be due to the dissolution of magnetite. Lund et al. (2017) also documented a >90% loss in MS at the National Crude Oil Spill Fate and Natural Attenuation Research Site administered by the United States Geological Survey (USGS) near Bemidji, MN, United States, between 2011 and 2015 when compared to initial MS observations from this aquifer (Mewafy et al., 2011; Atekwana et al., 2014). It was hypothesized that the reduction of MS was due to the transformation of magnetite to siderite coupled with the exhaustion of ferrihydrite.

Currently, we only have a poor understanding of the microbial communities driving the changes in MS and this uncertainty limits the effective application of MS as a proxy for biodegradation and iron cycling studies. The relationship between oil biodegradation and MS is complex as bacterial oil biodegradation coupled to iron reduction could result in the precipitation of magnetite and cause an increase in MS response. Once the bioavailable iron is depleted, the microbes may switch to other metabolic processes that use magnetite. This, in turn, can cause a decrease in the MS response through the oxidation of magnetite to maghemite and then hematite. Interestingly, initial characterization of the microbial community composition at the Bemidji site revealed that not iron-reducing bacteria were prevalent in zones where high MS was measured, but a microbial community dominated by the syntrophic bacterium *Smithella* and methanogenic Archaea (Beaver et al., 2016).

In this publication, we extend the Beaver et al. (2016) study, which was limited in scope because it showed data based on 1 year only, from just four samples along a 10 m long core, and it used clone libraries with the 16S rRNA gene, which is a limited molecular approach for the characterization of

microbial communities. Here, we present a multi-year analyses of the microbial community structure with closely spaced samples along complete cores using high-throughput DNA sequencing at the same hydrocarbon contaminated site exhibiting transient MS signatures. Our objective was to determine the key microbial populations in zones of elevated magnetic susceptibility and to provide insights into possible microbial-driven MS changes.

MATERIALS AND METHODS

Site Description

This study was conducted at the National Crude Oil Spill Fate and Natural Attenuation Research Site administered by the USGS. Here, a pipeline transporting crude oil broke in 1979 spilling about 1,700,000 L of crude oil. After cleanup efforts were completed in 1980, about 400,000 liters of oil remained in the unsaturated zone on the water table. This oil continues to be a source of groundwater contamination.

The spill resulted in two plumes in two low topographic areas designated as the north and south pools. The north oil pool is the location of the rupture site whereas the south oil pool resulted from the sprayed oil within a small wetland region (**Figure 1A**). The hydrocarbon contamination at the site is characterized by different hydrocarbon phases including a free-fluid phase approximately 0.75 m thick floating on the water table, a dissolved phase in the ground water, and a vapor phase in the unsaturated zone. Seasonal fluctuations of the water table have resulted in a smear zone characterized by residual phase smearing aquifer sediments (Essaid et al., 2011). Our study focuses on cores obtained from contaminated sediments in the free-phase petroleum in the north oil pool (**Figure 1A**).

The geology has been described as ∼20–25 m of moderately calcareous silty sand and outwash glacial deposits, overlying an unknown thickness of clayey till (Bennett et al., 1993). The upper 3 to 6 m are characterized by mostly poorly sorted, interbedded coarse sand, gravel, and silt. Beneath the upper layer, a 15–20 m laminated silt, very fine sand, and clay make up the majority of the lithology and this is underlain by the lower till layer.

Core Retrieval

All five cores from the free-phase oil zone were drilled within 1.9 m of each other and, according to their retrieval year, named C1110, C1215, C1308, C1407, and C1507 (**Figure 1B**). According to the fluctuating water table, these five cores were 8–10 m long and their sections are described in **Supplementary Table 1**. Core 1411 was retrieved from a location in the dissolved phase zone as indicated in **Figure 1A**. Cores were retrieved via percussion drilling using a core barrel containing either a 1″ or 2″ polycarbonate liner pushed through the sediment in a hollow stem auger. For the lowest core section crossing the water table, a sample-freezing drive shoe was used to retain the water from the aquifer by pumping liquid CO_2 to the bottom of the core which allowed the retention of the final section (Trost et al., 2018). A detailed description of the core sections can be found in **Supplementary Table 1**. Core C1110 was shipped on ice to Oklahoma State University (OSU, Stillwater, OK, United States), and stored frozen until MS analysis and sediment sample extraction for microbial analysis. Cores collected in years 2012, 2013, 2014, and 2015 were transported on ice to Western Michigan University, where they were stored at 4°C while the sampling of sediments for DNA isolation occurred in less than 10 days after arrival at the laboratory. Sediment samples were stored at −20°C until DNA isolation. The cores were subsequently shipped on ice to OSU, where they were frozen until MS analysis.

Magnetic Susceptibility (χ) Measurements

Magnetic susceptibility is the degree to which a sediment or mineral can be magnetized when a magnetic field is applied. MS is the ratio between M and H, where M is the magnetization of the material in the magnetic field and H is the field intensity (Blakely, 1995).

$$M = \chi H$$

M and H have the same units (A/m), so $\chi_{[vol]}$ is a dimensionless volume magnetic susceptibility. Magnetization is a certain measure of magnetism (dipole moment) per unit volume. The volume MS of the cores retrieved in 2011 and 2012 was measured with a Bartington MS2 magnetic susceptibility meter (Bartington Instruments, Witney, United Kingdom; operating frequency 4.65 kHz ± 1%; maximum resolution of 2×10^{-6} SI) coupled to a MS2B dual frequency sensor. For cores retrieved in 2014 and 2015, the volume MS values were acquired using the same meter, but it was coupled to a MS2C core scanning sensor, allowing the measurements to be taken from the complete cores that were slid through the sensor.

Gas Concentrations

Concentrations of O_2 + Ar, CO_2, and CH_4 were obtained from vapor well 601G (**Figure 1A**) as described by Mewafy et al. (2011) from the USGS National Water Information System database accessed on 11/7/2020 (U. S. Geological Survey, 2020). Based on limitations of the gas-chromatographic method used, oxygen and argon could not be separated and are plotted together.

Sampling and DNA Extraction

Sediment samples were obtained from holes cut through the side of the polycarbonate core liner. The sampling occurred in an anaerobic chamber (Shel Lab Model BactronEZ, Sheldon Manufacturing, Cornelius, OR, United States) for all years except for 2011. The anaerobic chamber was continuously fed with 90% nitrogen, 5% CO_2 and 5% H_2. Sediment samples were taken along the complete cores from top to bottom in ∼15 cm distances. Sterile spatulas were used to extract the sediments, which were placed aseptically into plastic centrifuge tubes. The sediment samples were then stored at −20°C in order to preserve the DNA until it was extracted. The PowerSoil DNA isolation kit (MO BIO, now Qiagen, Germantown, MD, United States) was used to isolate total DNA as directed in the protocol, but 0.5 g of sediment was substituted for 0.25 g in order to increase the DNA yield for cores obtained in 2011, 2012, and 2014. This method still did not produce enough DNA for analysis in some

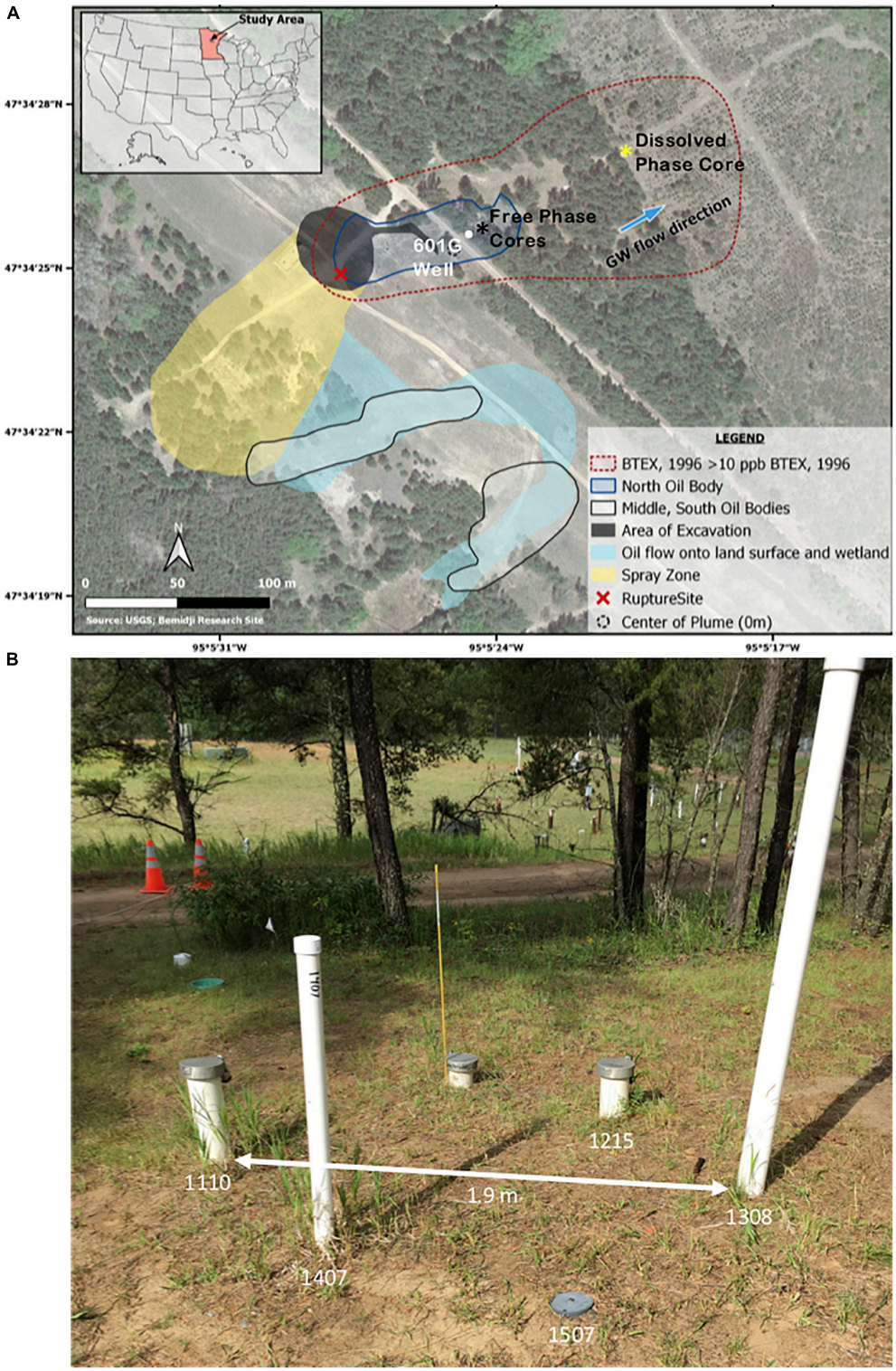

FIGURE 1 | (A) Satellite image from the National Crude Oil Spill Fate and Natural Attenuation Research Site at Bemidji, MN, overlaid with the extent of the free-phase oil and the dissolved plume as well as the location of the well and cores used in this study. The black star indicates the location of the five cores that were collected from the free-phase petroleum zone. The yellow star represents the location of the core that was collected in the dissolved-phase plume. The white dot represents the location of well 601G, which is ~5 m away from the location of the cores. The blue arrow indicates the direction of the ground water (GW) flow. BTEX, benzene, toluene, ethylbenzene, xylene. The image was retrieved from the USGS Bemidji Research Site (https://mn.water.usgs.gov/projects/bemidji/spatial/index.html) and modified. **(B)** Photographic image of the location of the five wells from which the free-phase cores were drilled in five consecutive years. The five wells are not more than 1.9 m apart.

of the samples for those years, so a different method that can extract more DNA from the sediments was used for 2013 and 2015. The method used for the samples obtained in 2013 and 2015 was the DNA extraction method described by Zhou et al. (1996), except that 4 g of sediment was used instead of 5 g due to the size of the centrifuge tubes. Although the use of different extraction methods has been shown to cause some variation in microbial community structure analysis (Guo and Zhang, 2013), we have used both methods with the same samples and show the resulting comparison in section "Comparison of Two Different Extraction Methods." DNA was further purified by the Promega Wizard SV Gel and PCR Cleanup System (Madison, Wisconsin) and then by Princeton Separations Centri-Sep Spin Columns (Freehold, NJ, United States). DNA was eluted in deionized H_2O in a final volume of 25 μl. After isolation, DNA was quantified with a Nanodrop (Thermo Fisher Scientific, Carlsbad, CA, United States) in 2011 and 2012 and with the Qubit Fluorometer 2.0 (Thermo Fisher Scientific, Carlsbad, CA, United States) in 2013–2015. To determine if any contaminating DNA was present in the DNA extraction kits or other reagents, control samples were obtained by following the extraction procedures using all the components without the addition of any sediment.

Sequencing and Statistical Analyses

Total DNA of the samples was sent to the RTSF Genomics Core at Michigan State University (East Lansing, MI, United States) for the construction of 16S rRNA gene libraries and high-throughput DNA sequencing. The libraries were constructed with the primers F515 and R806, targeting the V3/V4 variable regions of the 16S rRNA gene. The Illumina MiSeq platform (Illumina, San Diego, CA, United States) was used for sequencing the libraries by 250 base paired-end sequencing. Sequences were binned and annotated with QIIME. Forward and reverse reads were merged and quality controls were performed with Pandaseq (Masella et al., 2012). If the merged reads consisted of sequences shorter than 247 or longer than 275 base pairs, less than 45 base pairs as the minimum overlap of the forward and reverse read, or had an alignment score of less than 0.9, the read was discarded. Chimeras were identified with identify chimeric_seqs.py and eliminated, then operational taxonomic units (OTUs) were picked with the pick_open_reference_otus.py command using VSEARCH (Rognes et al., 2016) in QIIME (Caporaso et al., 2010). Only OTUs with 2 or more sequences were kept as part of the analysis. The reference set used with QIIME was the "Silva_119_rep_set97.fna" set which used a 97% similarity cutoff and taxonomic identification was completed with the "majority_taxonomy_7_levels.txt" file found in SILVA QIIME release 128. Contaminant OTUs found in the control samples without soil were removed from the core sample data manually in the Excel program (Microsoft Office Suite, Version 15.32).

Accession Numbers

The sequences generated in this study can be found in the Sequence Read Archive (SRA) of the National Center for Biotechnology Information (NCBI) under accession numbers SRR12074793–SRR12074794, SRR12075362–SRR12075368, SRR12076730–SRR12076740, SRR12077129–SRR12077144, SRR12082454–SRR12082467, SRR12082942–SRR12082962, SRR12091569–SRR12091584, and SRR12091932–SRR12091956.

Generation of Graphs and Statistical Analysis

Phyla and UniFrac graphs were generated and statistical analyses were performed with R (R Core Team, 2016), specifically the following R packages: Phyloseq v. 1.32.0 (McMurdie and Holmes, 2013), ggplot2 v. 3.3.2 (Wickham, 2009), grid v. 4.4.0 (Murrell, 2005), cowplot v. 1.1.0 (Wilkie, 2019), vegan v. 2.5.7 (Oksanen et al., 2013), plyr v. 1.8.6 (Wickham, 2011), tidyverse v. 1.3.0 (Wickham et al., 2019), and gridExtra v. 2.3 (Auguie, 2017). The nmds graph was generated with vegan and ggplot2. Predicted functional genes were determined by PICRUSt (Langille et al., 2013). The LEfSe analysis was generated with dada2 v. 1.0.3 (Callahan et al., 2016), microbial (Guo and Gao, 2020) and phyloseq.

RESULTS

Description of Cores

Sediment cores C1110, C1215, C1308, C1407, and C1507 were retrieved from the center of the free-phase oil at the north pool (**Figure 1**). Complete cores were retrieved from the surface at the elevation of ∼433 m down to below the water table, which was at ∼424 m. The units for the elevations are meters above sea level (m.a.s.l.) and pertain to all elevations mentioned in here, but are omitted for readability. The cores in the free-phase oil zone were taken no more than 1.9 m apart from each other to minimize spatial variability (**Figure 1B**). The cores were characterized by five distinct zones based on sediment characteristics from visual inspection and gas data (**Figures 2A,E,I,M** and **Supplementary Table 1**). The first zone was the upper vadose (UV) zone, which was not contaminated by any free-phase or residual oil and consisted of layers of sand or clay. This zone extended down to ∼ 428.5 m, approximately where the carbon dioxide and oxygen concentration graphs cross over in **Figures 2C,G,K**. The second zone, the lower vadose (LV) zone, was characterized by decreasing oxygen and increasing CO_2 and methane concentrations and was part of the unsaturated zone between the upper vadose zone and the smear zone, ending at ∼425.5 m. In the smear zone (SZ), residual phase hydrocarbons adhered to the sand particles above the free-phase oil. The length of the smear zone was dependent on the depth of the water table. The fourth zone, the free-phase oil (FP), consisted of a ∼0.75 m thick layer of free-phase petroleum on top of the water table, which was at approximately 424 m. The saturated (S) zone, with dissolved phase hydrocarbons, was below the free-phase oil zone. The geological description reveals mostly fine-grained sand with clay and silt across the water table.

Magnetic Susceptibility (MS)

Sediments were sampled from the cores, and subjected to MS measurements in the laboratory, augmenting our previous *in situ* measurements that were taken at the Bemidji site

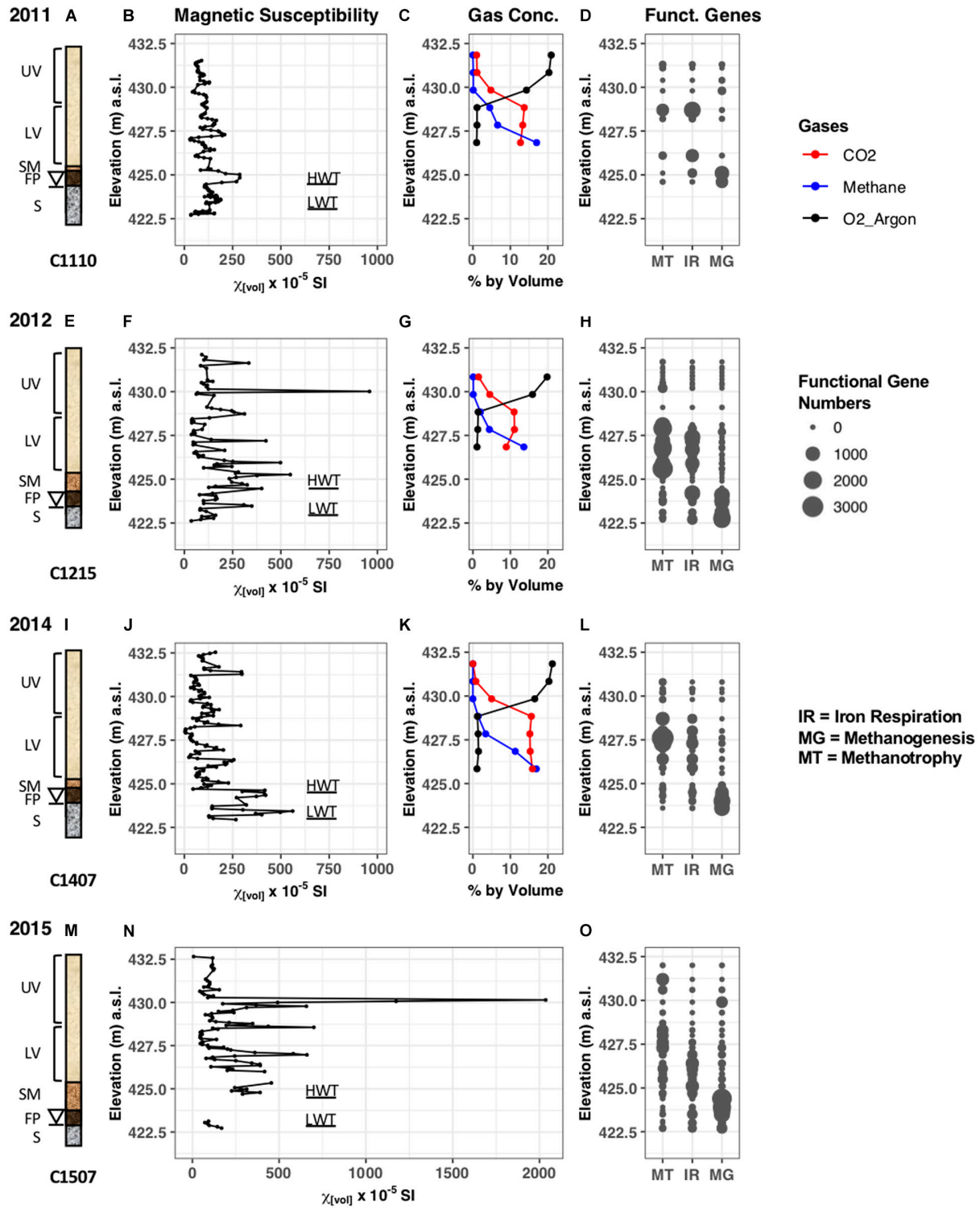

FIGURE 2 | Data collected pertaining to the cores retrieved in years 2011, 2012, 2014, and 2015. **(A,E,I,M)** Schematic drawing of the cores C1110, C1215, C1407, and C1507 retrieved from the north oil pool. The elevations of the smear zone, free-phase product, and saturated zone vary year to year due to the fluctuating water table (denoted by a triangle). UV, upper vadose zone; LV, lower vadose zone; SM, smear zone; FP, free-phase oil zone; S, saturated zone; HWT, high water table; LWT, low water table. **(B,F,J,N)** Magnetic susceptibility of sediments acquired in the years 2011, 2012, 2014, and 2015. **(C,G,K)** Gas concentrations (in % by volume) in well 601G measured in 2011, 2012, and 2014. **(D,H,L,O)** Predicted number of functional genes in the samples identified by PICRUSt. MT, Methanotrophy; IR, Iron respiration; MG, Methanogenesis.

(Atekwana et al., 2014; Lund et al., 2017). For core 1110, volume MS measurements ranged from a low of 29×10^{-5} SI at 427.0 m to a peak of 287×10^{-5} SI at 424.8 m at the water table (**Figure 2B**). In addition, there were several intermediate peaks found with one more pronounced peak in the vadose zone at 427.3 with 209×10^{-5} SI and another one in the saturated zone at 423.6 with a MS value of 188×10^{-5} SI. The MS measurements for core C1215 collected in 2012 varied from a low of 36×10^{-5} SI at 422.6 m to a peak of 959×10^{-5} SI at 430.1 m in the vadose zone (**Figure 2F**). The second largest MS peak occurred in the smear zone at 425.2 m, with a measurement of 549×10^{-5} SI. Several other peaks were found around the water table and in the lower vadose zone with values between 350 and 500×10^{-5} SI. No MS measurements were taken in 2013.

Core C1407 displayed several higher peaks around the water table with values above 350×10^{-5} SI, including the highest peak of 561×10^{-5} SI at 423.4 m (**Figure 2J**). Interestingly, core 1507 collected in 2015 showed an extremely high peak with MS values up to $2{,}000 \times 10^{-5}$ SI in the upper vadose zone (**Figure 2N**), at a similar depth compared to highest MS peak found in the core retrieved in 2012. Several other peaks with MS values above 500×10^{-5} SI occurred in the lower vadose zone. Unfortunately, a core section from around the water table was destroyed during transport and MS could not be measured. The elevated MS values found around the water table and in the free-phase petroleum in the cores from 4 different years are at similar depths that exhibited elevated MS values during the *in situ* measurements at the Bemidji site (Atekwana et al., 2014).

Gas Concentrations

Gas concentrations were measured in years 2011, 2012, and 2014 in well 601G, which is closest (∼5 m) to the core locations in the free-phase petroleum. Based on the limitations of the gas-chromatographic method used, oxygen and argon could not be separated and are therefore plotted together (Earth's atmosphere consists of 20.95% and 0.934% argon). **Figures 2C,G,K** show that oxygen concentrations decreased with increasing depths, while methane concentrations increased in the lower depths in all 3 years. Maximum methane concentrations were measured in 2011 and 2014 with 17% at the lowest depths. The CO_2 concentrations varied between 9 and 16% below 428.8 m. The O_2-CO_2 transition zone was at ∼429.4 m, whereas the O_2-CH_4 transition zone was at ∼428.8 m. The changes in concentration of these gasses indicate that sediments were anoxic below 428.8 m. No gas data were available from well 601G for 2015.

Characterization of Microbial Community Structure

Analysis of Replicates

Sediment samples were collected from the center of the retrieved cores with the spacing of 15 cm along the complete core length and DNA was isolated from these samples. First, we wanted to determine the reliability of our DNA isolation method and performed the DNA isolation and subsequent high-throughput DNA sequencing for core C1407 in duplicates. A UniFrac analysis was performed, which is a phylogenetic method for comparing microbial communities. It shows the relatedness of the microbial communities from each sample in a 2-dimensional space (**Figure 3**). This figure illustrates that (i) the replicate samples clustered very close together, and (ii) that there are three larger groupings which represent the free-phase oil zone (bottom left), the lower (bottom right) and the upper vadose zone (top). The two replicate smear zone samples were spaced somewhat away from the free-phase samples in the direction toward the lower vadose samples (**Figure 3**).

Comparison of Two Different Extraction Methods

During the 5 years of this study, we optimized the DNA extraction techniques. For samples collected in 2011–2013, we used a commercially available kit, while for the soil samples collected in 2014 and 2015, we used a more laborious method, not involving a kit, which was published by Zhou et al. (1996). Some variations are expected through the use of different extraction methods (Guo and Zhang, 2013). Nevertheless, **Supplementary Figure 1** shows that the two different methods applied to the same sediment sample collected from the free-phase oil zone displayed a similar microbial community composition. Deltaproteobacteria were found in similar high abundance with both methods (∼40%), while there seems to be a slight bias toward Actinobacteria in the DNA extracted with the commercial kit (25.1% vs. 14.2%) and a bias toward Euryarchaeota (3.9% vs. 8.5%) and Betaproteobacteria (5.5 % vs. 10.9 %) in the DNA extracted with the more laborious DNA extraction method. Overall, despite these biases, both methods revealed a quite similar microbial community composition (**Supplementary Figure 1**).

Analysis of Microbial Phyla

The abundance of microbial phyla according to depth is shown in **Figure 4** for the samples collected during the five different years. Each zone has a characteristic phyla distribution with little year-to-year variations. In the free-phase oil zone, shown at the bottom of the graphs, Deltaproteobacteria were found in high relative abundance. They were accompanied by methanogenic Euryarchaeota. The smear and lower vadose zone were dominated by Alpha- and Beta-Proteobacteria, representing methanotrophs and iron-reducers, respectively. Highly abundant phyla in the upper vadose zone were common soil bacteria from the Actinobacteria and Acidobacteria phyla (**Figure 4**).

Comparison of Free-Phase Samples With Samples From the Dissolved Phase

A comparison between the microbial communities present in the free-phase oil zone versus those present in a location in the dissolved-phase plume was warranted. Lower MS values were found around the water table in the dissolved-phase plume than in the free-phase oil (Atekwana et al., 2014). It was no problem isolating sufficient microbial DNA quantities for downstream applications from the cores retrieved in the free-phase petroleum zone. It seems that the overabundance of hydrocarbons at the water table resulted in active microbial communities producing sufficient biomass for making our DNA isolations successful throughout the length of the core. Unfortunately, and probably

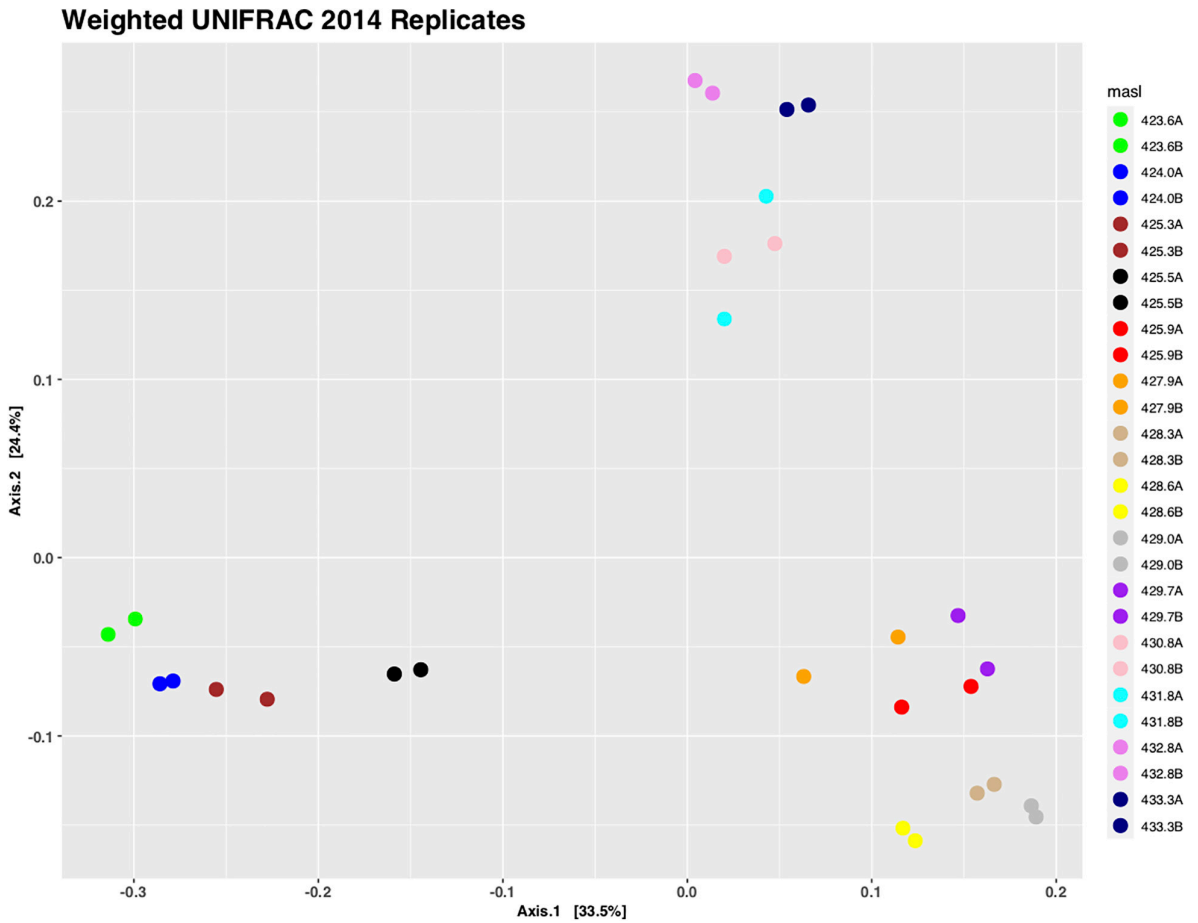

FIGURE 3 | Principal coordinate analysis (PCoA) of weighted UniFrac distances of replicate samples taken from core 1407. Replicate samples are shown in identical colors and sample names are based on the depth they were taken from. Replicates group closely together using PERMANOVA (R^2 = 1, p = 1).

because of the much lower hydrocarbon concentration ∼100 m away from the free-phase oil (**Figure 1A**), there seems to be much less biomass present in the dissolved plume. We were only able to isolate sufficient DNA quantities for reliable DNA sequencing from samples around the water table from the core retrieved in the dissolved phase. A UniFrac analysis shows that the samples from around the water table of the dissolved phase core clustered together on the one side of the diagram, whereas the samples taken from around the water table from free-phase cores clustered on the other side, far away from each other (**Figure 5**). This is an indication that the microbial community composition differs greatly between these two groups of samples. Also, the microbial phyla composition and the top 10 most abundant genera at this site were completely different from the ones found in the free-phase oil zone (**Supplementary Figure 2** and **Supplementary Table 2**).

Analysis of Most Abundant Microbial Genera in the Free-Phase Location

Table 1 shows the results using the linear discriminant analysis (LDA) effect size (LEfSe) method, which identifies the most abundant and characteristic bacterial taxa in different sample groups (Segata et al., 2011). The most abundant and characteristic bacterial genera for a specific sample group receive a high LDA score and are considered to be a "biomarker" for that specific group of samples and are discussed below according to the zonation in the free-phase oil cores.

Free-phase oil zone

The genus found in the free-phase oil zone with the highest LDA score was *Smithella*. Laboratory-grown *Smithella* is capable of propionate oxidation, and it was found to be the most abundant long-chain alkane degrader in methanogenic enrichment cultures (Liu et al., 1999; de Bok et al., 2001; Gray et al., 2011; Cheng et al., 2013; Tan et al., 2014; Wawrik et al., 2016; Qin et al., 2017; Xia et al., 2019; Ji et al., 2020). To metabolize the long-chain alkanes, *Smithella* activates them by fumarate addition and then excretes CO_2 and H_2, which, in turn, are being used by methanogens. The genus with the second highest score found in all samples of the free-phase oil zone was a hydrogenotrophic methanogen, *Methanoregula* (Brauer et al., 2011). Hydrogenotrophic methanogens use CO_2 and H_2 to synthesize methane. *Methanoregula* species have been isolated from acidic peat bogs and from methanogenic sludge used for

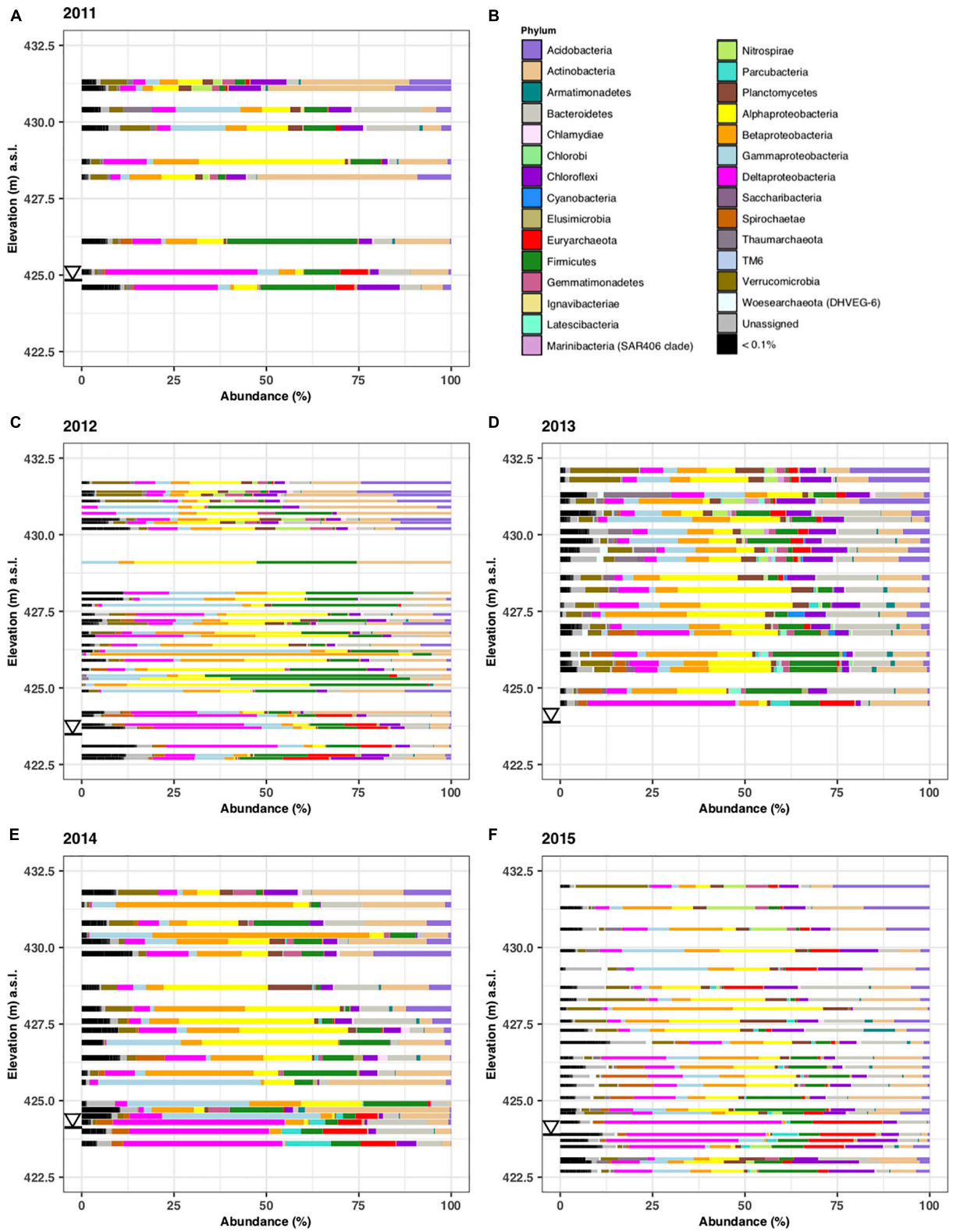

FIGURE 4 | Microbial phyla identified in samples collected along the complete length of sediment cores collected in years 2011–2015. The microbial abundance in % is plotted on the *x*-axis while the elevation from which the core was taken is plotted in meters above surface level (m.a.s.l.) on the *y*-axis. Samples were from core C1110 **(A)**, C1215 **(C)**, C1308 **(D)**, C1407 **(E)**, and C1507 **(F)**. Only phyla that constituted >0.1% are shown by name **(B)**. The triangle denotes the water level in the different years.

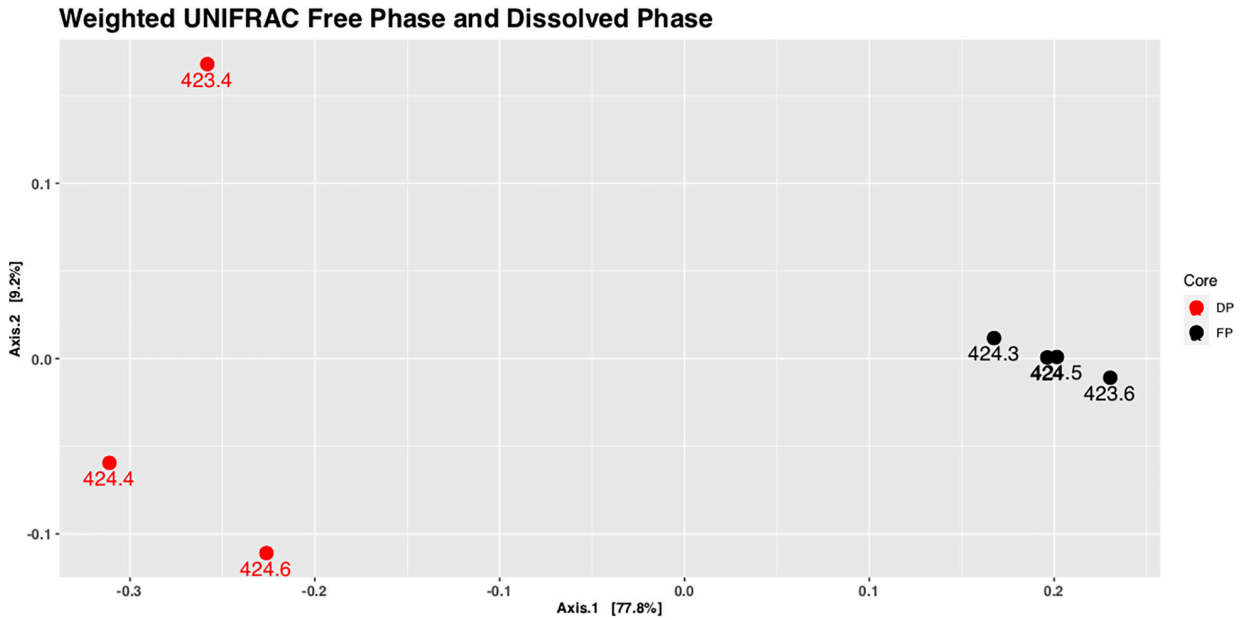

FIGURE 5 | Principal coordinate analysis (PCoA) plot of weighted UniFrac distances of samples taken from the water table in the free-phase oil zone (core 1407; FP, black) and from the water table in the dissolved-phase plume (core 1411; DP, red). The dissolved phase samples group separately from the free-phase oil samples using PERMANOVA (R^2 = 0.767, p = 0.035). The labels for the points denoting the samples from 424.0 to 424.5 m (a.s.l.) of core 1407 overlap.

the treatment of brewery effluents (Brauer et al., 2011; Yashiro et al., 2011). In addition, an unclassified genus of the Candidatus Yanofskybacteria was found to be a biomarker in the free-phase oil samples. This candidate genus belongs to the newly described superphylum Patescibacteria and is a member of the Parcubacteria (formerly OD1), which are prevalent in anoxic groundwater, sediments and aquifers. Parcubacteria are of very small size, have reduced genomes, and seem to depend on other members of the microbial community for obtaining essential metabolites (Brown et al., 2015; Tian et al., 2020). Candidatus Yanofskybacteria have frequently been found to be associated with anoxic carbon transformation and hydrogen generation (Castelle et al., 2015; Solden et al., 2016; Jaffe et al., 2020). Another biomarker in the free-phase oil zone was *Desulfosporosinus.* This spore-forming bacterium has been isolated from gasoline-contaminated aquifers (Robertson et al., 2000) and has been identified as a syntrophic toluene degrader in a methanogenic microbial community (Abu Laban et al., 2015). Another high-scoring microorganism in the free-phase oil zone was *Pelolinea* from the Chloroflexi phylum, which has been shown to be involved in the degradation of phenolic compounds (Chen et al., 2020). All the above-mentioned genera are known to be strict anaerobes.

Smear zone

Uncultured *Coriobacteriaceae*, which belong to the Actinobacteria phylum, had the highest LDA score in the smear zone. These obligate anaerobes are capable of both, fermentation and anaerobic respiration. Lentini et al. (2012) found representatives of uncultured *Coriobacteriaceae* in enrichment cultures with ferrihydrite, goethite and hematite as electron acceptor. *Coriobacteriaceae* have also recently been identified in methanic environments such as terrestrial serpentinizing fluid seeps (Woycheese et al., 2015), deep groundwater (Hernsdorf and Amano, 2017), marine enrichment cultures undergoing benzoate degradation with concurrent iron reduction and methanogenesis (Aromokeye et al., 2020) and at a thermophilic electromethanogenic biocathode (Kobayashi et al., 2017). *Thermincola,* a Gram-positive bacterium of the *Peptococcaceae* family, also exhibited a high score for the smear zone. In an enrichment culture, *Thermincola ferriacetica* was found to be dominant under ferrihydrite-reducing conditions (Kato et al., 2019), and the formation of magnetite was observed when amorphous Fe(III) hydroxide was used as electron acceptor for *T. ferriacetica* (Zavarzina et al., 2007). Magnetite could serve as an alternative electron acceptor for *T. ferriacetica* in these sediments (Zavarzina et al., 2007). Also having a high score in the smear zone was *Paenibacillus,* a facultative anaerobic endospore-former of the Firmicutes phylum. *Paenibacillus* strains have been frequently isolated from soil and they can degrade a variety of aliphatic and aromatic hydrocarbons (Grady et al., 2016). Despite considered being aerobic, the Alphaproteobacterium *Beijerinckia* was also a biomarker of the smear zone, and in addition to its ability to fix atmospheric nitrogen, it is able to oxidize a wide variety of organic compounds, including methane and methanol (Wegner et al., 2020).

Lower vadose zone

The highest LDA scores for the lower vadose zone were assigned to two members of the Betaproteobacteria, *Polaromonas* and an uncultured genus of the *Comamonadaceae*. Strains of *Polaromonas* were initially isolated in Antarctica, but

TABLE 1 | Top genera identified as biomarkers for the four different zones based on Linear Discriminant Analysis (LDA) scores.

Genera	LDA score	*p*-value[a]
Free-phase petroleum		
Smithella	6.08	8.50×10^{-5}
Methanoregula	5.56	6.73×10^{-10}
Candidatus Yanofskybacteria	5.27	3.04×10^{-9}
Desulfosporosinus	5.15	1.63×10^{-8}
Pelolinea	5.00	7.93×10^{-10}
Smear zone		
Coriobacteriaceae uncultured	5.42	4.71×10^{-7}
Thermincola	5.41	2.61×10^{-6}
Paenibacillus	5.39	3.64×10^{-4}
Beijerinckia	5.29	4.48×10^{-8}
Spirochaetaceae uncultured	5.15	3.63×10^{-7}
Lower vadose zone		
Polaromonas	5.19	2.14×10^{-9}
Comamonadaceae uncultured	5.12	2.21×10^{-4}
Geobacter	5.07	1.01×10^{-7}
Methylocystis	4.94	8.52×10^{-12}
Devosia	4.86	6.68×10^{-10}
Rhodopseudomonas	4.78	2.91×10^{-9}
Upper vadose zone		
Actinobacteria MB-A2-108 uncultured	5.20	7.45×10^{-10}
Gaiellales uncultured	5.14	8.52×10^{-8}
Chthoniobacterales DA101 soil group	5.14	1.00×10^{-7}
Gemmatimonadaceae uncultured	5.08	3.47×10^{-8}
Pseudarthrobacter	4.99	1.05×10^{-4}

[a]*p-value based on Kruskal–Wallis rank sum test.*

have now been found in many environments. *Polaromonas* has been reported to be instrumental in the degradation of pollutants, including aliphatic, aromatic, polycyclic and chlorinated hydrocarbons (Mattes et al., 2008). The uncultured member of the *Comamonadaceae* seems to be related to *Rhodoferax*, an anaerobic bacterium that respires short chain fatty acids by iron reduction (Finneran et al., 2003). A well-studied iron-reducing and hydrocarbon-degrading bacterium, *Geobacter,* was also a marker for the lower vadose zone (Lovley et al., 1989). *Geobacter* is known for synthesizing magnetite during the reduction of Fe(III)-oxyhydroxide (Byrne et al., 2015) and magnetite has been shown to stimulate direct electron transfer (DIET) during syntrophic methanogenesis (Kato et al., 2012; Lovley, 2017). Another biomarker for the lower vadose zone was *Methylocystis*. The aerobic, methane-oxidizer *Methylocystis* has been found to be widely distributed in wetlands, peatlands and aquifers. This wide distribution is explained by *Methylocystis*' extended metabolic capability to use acetate or ethanol in the absence of methane and to fix dinitrogen (Han et al., 2018). *Methylocystis* has also been detected in groundwater contaminated with heavy metals including arsenic, displaying genes for As(III) oxidation and As(V) reduction (Shi et al., 2018; Danczak et al., 2019). High LDA scores for the lower vadose zone were also assigned to the Alphaproteobacteria *Devosia* and *Rhodopseudomonas*. *Devosia* species have been isolated from diesel-contaminated soil (Ryu et al., 2008), while *Rhodopseudomonas* is known to be an iron-oxidizer that is able to take up electrons from solid iron and cathodes (Bose et al., 2014).

Upper vadose zone

The two most important biomarkers in the upper vadose zone were members of the Actinobacteria phylum. The first, carrying the designation MB-A2-108, was identified in methane hydrate-bearing, deep marine sediments off the Japanese coast (Reed et al., 2002; Zhang et al., 2016; Curd et al., 2018). The second was an uncultured member of the order Gaiellales. Not much is known about this deep-branching phylogenetic lineage, although one *Gaiella* species has been isolated from a deep mineral water aquifer in Portugal (Albuquerque et al., 2011). Also having a high LDA score in the upper vadose zone was the *Chthoniobacterales* DA101 soil group of the *Verrucomicrobia* phylum, which has been found to be extremely common in many soil samples analyzed with molecular methods (Brewer et al., 2016), as well as uncultured members of the *Gemmatimonadaceae* of the Gemmatimonadetes phylum that are widespread in nature and make up around 2% of soil microbial communities (Zhang et al., 2003). The genus *Pseudarthrobacter* was also indicative of the upper vadose zone. *Pseudarthrobacter* species have been isolated from sewage and were found to be able to degrade chlorophenol (Kim et al., 2008).

Analysis of Microbial Metabolism With PICRUSt

The high-throughput DNA sequencing of the 16S rRNA gene resulted in an overview of the microbial community structure at the different depths of the free-phase cores. From this phylogenetic information, we can estimate the metabolic capabilities of the indigenous microorganisms present with a program called PICRUSt (Phylogenetic Investigation of Communities by Reconstruction of Unobserved States; Langille et al., 2013). This program predicts the predominant metabolic pathways based on marker gene survey data (such as the 16S rRNA gene). Although this program was developed for the analysis of the intestinal microbiome, we extracted three pertinent metabolic pathways: methanogenesis, iron reduction and methanotrophy, which are plotted according to depth in **Figures 2D,H,L,O**. Confirming earlier reports (Bekins et al., 1999; Amos et al., 2005), it is obvious that the free-phase zone is methanic with a majority of methanogenesis genes found below 424.5 m. The majority of the iron reduction genes are present above the methanic zone, from ∼424.5 to 428 m. The majority of the genes that enable microorganisms to oxidize methane were found to overlap with the upper iron reduction zone at ∼426–429 m.

Iron Mineral Analysis

The iron mineral phases were determined for samples from selected depths of core C1407 and compared to the MS (**Supplementary Figure 3**). The highest MS was measured at 423.2 m, which is inside the free-phase oil zone. Coinciding, the highest concentrations of Fe(II) and magnetite were measured

at the same depth. In addition, the FeII/FeIII ratio was the highest at this depth. Reactive and reducible Fe(III) in the form of ferrihydrite and hematite/goethite, respectively, was depleted in the lower depths, but showed higher concentrations between 424.4 and 424.8 m and close to the surface.

Linking Microbial Taxa With Magnetic Susceptibility

Figure 6 displays a diagram of non-metric multidimensional scaling (NMDS) for all samples from years 2011, 2012, 2014, and 2015 together with the 25 most abundant microbial taxa and the MS data as variable (shown as vector). Samples from the free-phase zone from 422.8 to 424.8 m grouped together with the genera *Smithella*, *Methanoregula* and Candidatus Yanofskybacteria and with the MS vector pointing into the direction of that grouping. The arrow length is proportional to the degree of correlation between the ordination and the MS as environmental variable, although the fitting of the vector was not highly significant (p-value of 0.48).

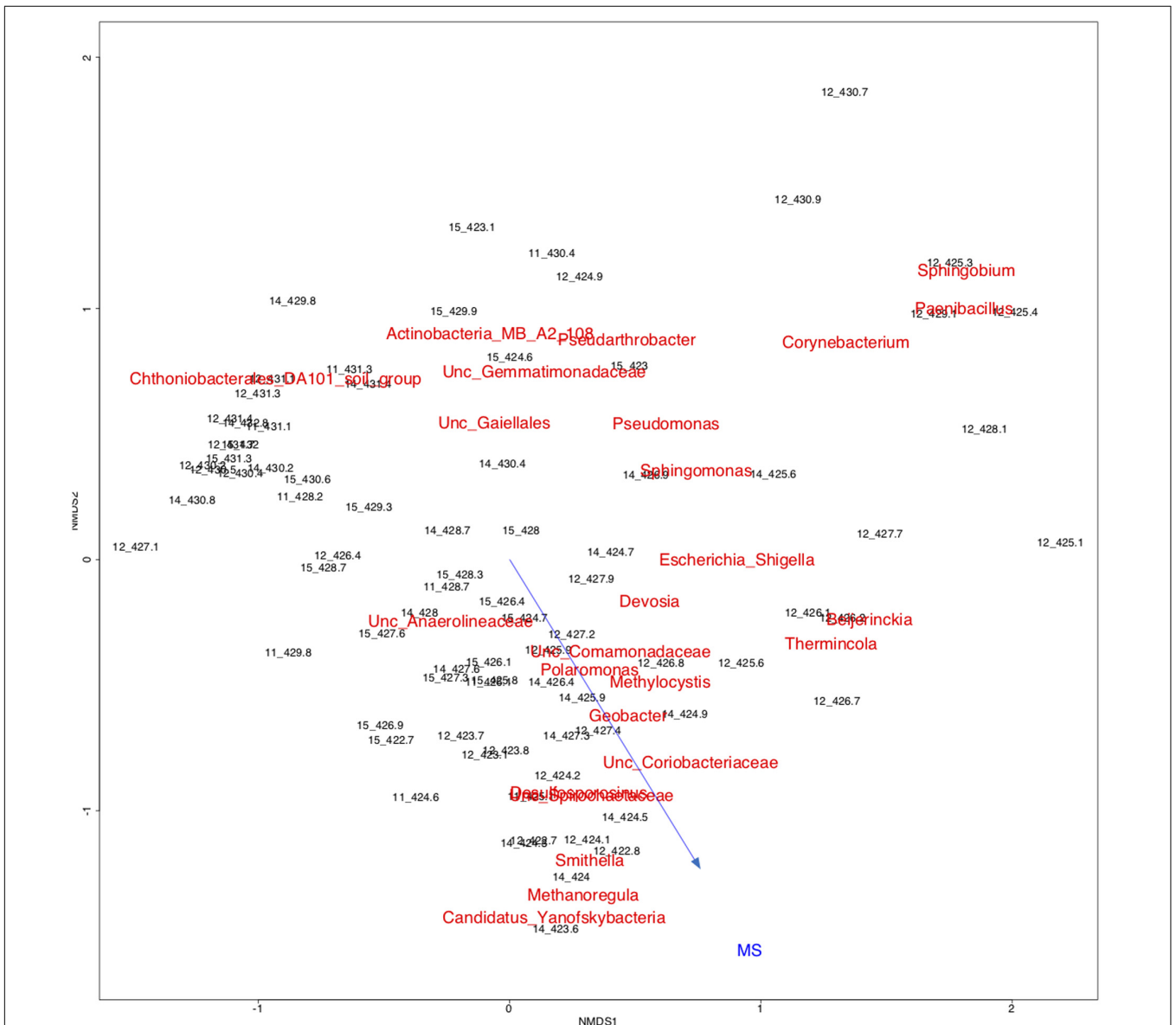

FIGURE 6 | Two-dimensional non-metric multidimensional scaling (NMDS) based on Bray-Curtis dissimilarities showing all samples from the complete lengths of cores collected in 2011, 2012, 2014, and 2015 from the free-phase oil zone, in addition to the top 25 microbial taxa and the magnetic susceptibility (MS) as variable (vector). Samples labeled according to the depths they were collected from are shown in black, while the microbial taxa are shown in red. The names for the two taxa "*Desulfosporosinus*" and "Unc. (= uncultured) *Spirochaetaceae*" overlap. The MS arrow (blue) points into the direction of the samples and taxa from the free-phase oil, showing a correlation between theses samples, microbial taxa and the MS as environmental variable, although with low statistical significance (p = 0.48). Plot Stress = 0.18.

DISCUSSION

Relationship Between Microbial Populations and Magnetic Susceptibility

Our multi-year analysis of the microbial community structure at the aged subsurface hydrocarbon spill site at Bemidji, MN, United States, revealed that a methanogenic microbial community is present in the free-phase petroleum zone. This confirms earlier studies that reported methane emissions at this site (Amos et al., 2005) and a preliminary microbial community analysis based on clone libraries, which showed the presence of methanogenic Archaea (Beaver et al., 2016). The main methane-generating microorganisms belonged to the genus *Methanoregula*. These are hydrogenotrophic methanogens, using hydrogen and carbon dioxide to produce methane. The prominent hydrogen provider at this site seems to be the syntrophic Deltaproteobacterium *Smithella* that was found in all years with an abundance of up to 46% in the free-phase samples. A comprehensive analysis revealed that *Smithella* is widespread at different hydrocarbon spill sites all over the world (Gray et al., 2011) and it has recently been shown that *Smithella* is able to attack long-chain hydrocarbons by fumarate addition and subsequent beta-oxidation (Ji et al., 2020). At the Bemidji site, the free-phase petroleum floats on the water table 9 m below the surface. Above the methanic zone, we found microorganisms that are able to oxidize methane aerobically, mainly belonging to the alphaproteobacterial genus *Methylocystis*. The same zone was also characterized by the presence of iron-reducing bacteria, specifically *Geobacter*. A conceptual model is shown in **Figure 7**.

How can we relate these results with the MS values that were measured at Bemidji? First, we have to mention that the high MS values that were measured in year 2011 around the water table in the free-phase petroleum decreased substantially (∼90%) in the following years when measured down the borehole (Lund et al., 2017). On the other hand, here we report that the elevated MS values measured around the water table in the retrieved cores did not substantially decrease over 5 years when measured in the laboratory (**Figure 2**). The MS values of sediments usually depend on their magnetite content. Magnetite can form biotically, in particular through the action of iron-reducing bacteria. Hansel et al. (2005) proposed a model for magnetite formation under iron reducing conditions when there is >2 mM aqueous Fe(II) in the presence of ferrihydrite. Piepenbrock et al. (2011) reported magnetite formation when the ferrihydrite concentration exceeded 5 mM. These values are comparable to the values that we measured in core 1407 (**Supplementary Figure 3**). It remains enigmatic, however, why the highest MS values were found in the methanic zone around 423/424 m and not in the iron-reducing zone one to two meters above (**Figure 2**). Possible explanations entail (1) a washing out of magnetic minerals during recharge events from the iron-reducing zone above to the methanic zone below or (2) the ability of the methanogens themselves to switch their metabolism from methanogenesis to iron reduction, resulting in the formation of magnetite. This idea is supported by growing evidence in the literature suggesting that iron

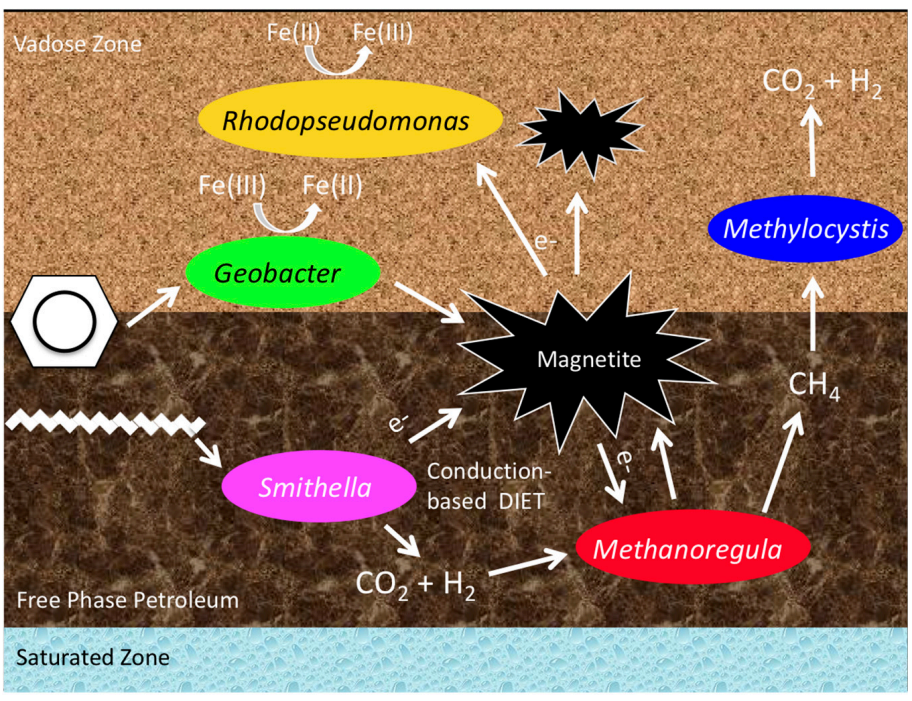

FIGURE 7 | Conceptual model of the predominant bacteria and the metabolic processes in and above the free-phase oil zone.

utilization by methanogens mediates the formation of different iron mineral phases (Sivan et al., 2016; Amiel et al., 2020; Shang et al., 2020). Nevertheless, to support our data further, whole metagenome DNA sequencing or RNA-based methods, such as a transcriptome analysis, are necessary.

The presence of magnetite can even be beneficial for methanogenesis. Magnetite was shown to increase the rate of methane production in laboratory experiments with syntrophic bacteria and methanogenic Archaea, because they are capable of direct interspecies electron transfer (DIET) using conductive minerals like magnetite (Kato et al., 2012; Cruz Viggi et al., 2014; Yamada et al., 2015; Yang et al., 2015). Contributing evidence that electron transfer may be occurring between *Smithella* and *Methanoregula* is that a self-potential anomaly resulting from a biogeobattery was observed at this site (Heenan et al., 2017). In the Heenan et al. (2017) study, self-potential measurements using a vertical array of electrodes showed a dipolar pattern across the water table fluctuation zone associated with a current source. Such biogeobatteries are postulated to occur in the capillary fringe of contaminant plumes. The large gradient in redox potential at the capillary fringe might allow microbes to transfer electrons from one to another through conductive minerals like magnetite or through biological structures such as nanowires or biofilms, operating in a similar manner to fuel cells (Revil et al., 2010). Interestingly, *Methanoregula* has been enriched on the cathode in microbial fuel cells when current was applied (Chen et al., 2016; Zhang and Lu, 2016; Xia et al., 2019), which indicates that it can accept electrons from conductive materials.

Factors contributing to the dissolution of magnetite and therefore the decreasing MS response can be the activities of iron-oxidizing bacteria such as *Rhodopseudomonas,* which was found with a high LDA score in the lower vadose zone. In laboratory experiments, *Rhodopseudomonas* was shown to oxidize magnetite with and without photosynthesis and it was concluded that magnetite can serve as an electron sink or source (Bose et al., 2014; Byrne et al., 2015). To evaluate the fate of magnetite at hydrocarbon contaminated sites, experiments are currently being carried out at the Bemidji site that study the long-term fate of submerged magnetite minerals at the free-phase petroleum location (L. Slater, pers. communication).

An enigma remains concerning the occurrence of large single MS peaks in the upper vadose zone which were measured at 430 m in two of the 4 years (**Figure 2**). These outliers could be due to technical errors; nevertheless, this is unlikely because i) at least in 2015, the high MS was represented by more than one measuring point and ii) it was found at the same depth in two different years.

MS as a Tool

Magnetic susceptibility can be used as a tool to identify hotspots of biodegradation at a single point of time as described by Beaver et al. (2016) or to track changes in microbial activity over the long term as reported by Lund et al. (2017). Peaks in MS found in cores retrieved from contaminated sediments can be used for pinpointing the most important biochemical or microbial samples to take. After core retrieval, the wells left behind can be monitored for MS changes to determine the predominant metabolic processes occurring during natural attenuation or bioremediation of hydrocarbon spills.

Conclusion

The microbiological data presented here are the first that allow a spatial and temporal analysis of this spill site because the sediment cores were retrieved in five consecutive years and the samples were collected along the complete length of the cores. The data for the years 2011–2015 confirm previous research findings that the free-phase oil is being degraded by a consortium consisting of the syntrophic *Smithella* and the methanogenic *Methanoregula*. The smear zone is a transition zone from methanogenesis to iron reduction, with *Thermincola* being the most common iron reducer in this zone. Iron cycling and methanotrophy seem to be the dominant processes in the lower vadose zone where iron reducers such as *Geobacter*, iron oxidizers such as *Rhodopseudomonas*, and the methanotroph *Methylocystis* are present (**Figure 7**). The upper vadose is inhabited by aerobic organisms, mainly belonging to the *Actinobacteria* and *Acidobacteria* phyla (**Figure 2**).

Interestingly, despite the notion that elevated MS values are indicative of higher magnetite concentrations precipitated by the actions of iron-reducing bacterial populations, higher MS values were measured in the methanic free-phase oil zone around the water table and not in the iron-reducing zone above. This finding could be one of the first field evidences that show the metabolic potential of methanogens to switch their metabolism from methanogenesis to iron reduction with concomitant magnetite precipitation. The results presented here provide additional evidence for the role of microbes in environmental magnetism and the magnetic record of terrestrial and marine environments. Further studies are needed in order to determine if changes in MS can be linked to different stages of the bioremediation process.

DATA AVAILABILITY STATEMENT

The datasets presented in this study can be found in online repositories. The names of the repository/repositories and accession number(s) can be found below: https://www.ncbi.nlm.nih.gov/sra, SRR12074793–SRR12074794, https://www.ncbi.nlm.nih.gov/sra, SRR12075362–SRR12075368, https://www.ncbi.nlm.nih.gov/sra, SRR12076730–SRR12076740, https://www.ncbi.nlm.nih.gov/sra, SRR12077129–SRR12077144, https://www.ncbi.nlm.nih.gov/sra, SRR12082454–SRR12082467, https://www.ncbi.nlm.nih.gov/sra, SRR12082942–SRR12082962, https://www.ncbi.nlm.nih.gov/sra, SRR12091569–SRR12091584, and https://www.ncbi.nlm.nih.gov/sra, SRR12091932–SRR12091956.

AUTHOR CONTRIBUTIONS

CB, SR, EA, BB, DN, and LS conceived the study. CB performed the microbiological experiments and analyses. EA, DN, and LS performed the geophysical analysis. CB, SR, and EA wrote the

manuscript. All authors contributed to the article and approved the submitted version.

FUNDING

The authors acknowledge funding from the Chevron Energy Technology (Grant #CW852844) and the National Crude Oil Spill Fate and Natural Attenuation Research Site, a collaborative venture of the United States Geological Survey (USGS), Enbridge Energy, Limited Partnership, the Minnesota Pollution Control Agency and Beltrami County. Any use of trade, product, or firm names in this publication is for descriptive purposes only and does not imply endorsement by the US Government.

ACKNOWLEDGMENTS

We thank Jared Trost and Andrew Berg (USGS) for field support, and Farag Mewafy, Brittany Ford, Sundeep Sharma, and Drs. Allison Enright and Carl Rosier (Oklahoma State University) for their assistance with geophysical data collection. We also acknowledge Dr. Denise Akob and three reviewers for their helpful suggestions which have improved this manuscript.

SUPPLEMENTARY MATERIAL

The Supplementary Material for this article can be found online at: https://www.frontiersin.org/articles/10.3389/feart.2021.598172/full#supplementary-material

REFERENCES

Abu Laban, N., Tan, B., Dao, A., and Foght, J. (2015). Draft genome sequence of uncultivated *Desulfosporosinus* sp. strain Tol-M, obtained by stable isotope probing using [13C6]toluene. *Genome Announc.* 3:e01422-14. doi: 10.1128/genomeA.01422-14

Albuquerque, L., Franca, L., Rainey, F. A., Schumann, P., Nobre, M. F., and da Costa, M. S. (2011). *Gaiella occulta* gen. nov., sp. nov., a novel representative of a deep branching phylogenetic lineage within the class Actinobacteria and proposal of *Gaiellaceae* fam. nov. and Gaiellales ord. nov. *Syst. Appl. Microbiol.* 34, 595–599. doi: 10.1016/j.syapm.2011.07.001

Ameen, N. N., Klueglein, N., Appel, E., Petrovsky, E., Kappler, A., and Leven, C. (2014). Effect of hydrocarbon-contaminated fluctuating groundwater on magnetic properties of shallow sediments. *Stud. Geophys. Geodaet.* 58, 442–460. doi: 10.1007/S11200-014-0407-3

Amiel, N., Shaar, R., and Sivan, O. (2020). The effect of early diagenesis in methanic sediments on sedimentary magnetic properties: case study from the SE mediterranean continental shelf. *Front. Earth Sci.* 8:283. doi: 10.3389/feart.2020.00283

Amos, R. T., Mayer, K. U., Bekins, B. A., Delin, G. N., and Williams, R. L. (2005). Use of dissolved and vapor-phase gases to investigate methanogenic degradation of petroleum hydrocarbon contamination in the subsurface. *Water Resour. Res.* 41:W02001. doi: 10.1029/2004wr003433

Aromokeye, D. A., Oni, O. E., Tebben, J., Yin, X., Richter-Heitmann, T., Wendt, J., et al. (2020). Crystalline iron oxides stimulate methanogenic benzoate degradation in marine sediment-derived enrichment cultures. *ISME J.* doi: 10.1038/s41396-020-00824-7 [Epub ahead of print].

Atekwana, E. A., Mewafy, F. M., Abdel Aal, G., Werkema, D. D., Revil, A., and Slater, L. D. (2014). High-resolution magnetic susceptibility measurements for investigating magnetic mineral formation during microbial mediated iron reduction. *J. Geophys. Res. Biogeo.* 119, 80–94. doi: 10.1002/2013jg002414

Auguie, B. (2017). *"gridExtra: Miscellaneous Functions for "Grid" Graphics"*. R Package Version 2.3.

Beaver, C. L., Williams, A. E., Atekwana, E. A., Mewafy, F. M., Abdel Aal, G., Slater, L. D., et al. (2016). Microbial communities associated with zones of elevated magnetic susceptibility in hydrocarbon-contaminated sediments. *Geomicrobiol. J.* 33, 441–452. doi: 10.1080/01490451.2015.1049676

Bekins, B. A., Godsy, E. M., and Warren, E. (1999). Distribution of microbial physiologic types in an aquifer contaminated by crude oil. *Microb. Ecol.* 37, 263–275. doi: 10.1007/S002489900149

Bennett, P. C., Siegel, D. E., Baedecker, M. J., and Hult, M. F. (1993). Crude-oil in a shallow sand and gravel aquifer .1. Hydrogeology and inorganic geochemistry. *Appl. Geochem.* 8, 529–549. doi: 10.1016/0883-2927(93)90012-6

Blakely, R. J. (1995). *Potential Theory in Gravity and Magnetic Applications*. New York, NY: Cambridge University Press.

Bose, A., Gardel, E. J., Vidoudez, C., Parra, E. A., and Girguis, P. R. (2014). Electron uptake by iron-oxidizing phototrophic bacteria. *Nat. Commun.* 5:3391. doi: 10.1038/ncomms4391

Brauer, S. L., Cadillo-Quiroz, H., Ward, R. J., Yavitt, J. B., and Zinder, S. H. (2011). *Methanoregula boonei* gen. nov., sp. nov., an acidiphilic methanogen isolated from an acidic peat bog. *Int. J. Syst. Evol. Micr.* 61, 45–52. doi: 10.1099/Ijs.0.021782-0

Brewer, T. E., Handley, K. M., Carini, P., Gilbert, J. A., and Fierer, N. (2016). Genome reduction in an abundant and ubiquitous soil bacterium '*Candidatus* Udaeobacter copiosus'. *Nat. Microbiol.* 2:16198. doi: 10.1038/nmicrobiol.2016.198

Brown, C. T., Hug, L. A., Thomas, B. C., Sharon, I., Castelle, C. J., Singh, A., et al. (2015). Unusual biology across a group comprising more than 15% of domain Bacteria. *Nature* 523, 208–211. doi: 10.1038/nature14486

Byrne, J. M., Klueglein, N., Pearce, C., Rosso, K. M., Appel, E., and Kappler, A. (2015). Redox cycling of Fe(II) and Fe(III) in magnetite by Fe-metabolizing bacteria. *Science* 347, 1473–1476. doi: 10.1126/science.aaa4834

Callahan, B. J., McMurdie, P. J., Rosen, M. J., Han, A. W., Johnson, A. J., and Holmes, S. P. (2016). DADA2: High-resolution sample inference from Illumina amplicon data. *Nat. Methods* 13, 581–583. doi: 10.1038/nmeth.3869

Caporaso, J. G., Kuczynski, J., Stombaugh, J., Bittinger, K., Bushman, F. D., Costello, E. K., et al. (2010). QIIME allows analysis of high-throughput community sequencing data. *Nat. Methods* 7, 335–336. doi: 10.1038/nmeth.f.303

Castelle, C. J., Wrighton, K. C., Thomas, B. C., Hug, L. A., Brown, C. T., Wilkins, M. J., et al. (2015). Genomic expansion of domain archaea highlights roles for organisms from new phyla in anaerobic carbon cycling. *Curr. Biol.* 25, 690–701. doi: 10.1016/j.cub.2015.01.014

Chen, H., Hao, S., Chen, Z., Sompong, O. T., Fan, J., Clark, J., et al. (2020). Mesophilic and thermophilic anaerobic digestion of aqueous phase generated from hydrothermal liquefaction of cornstalk: molecular and metabolic insights. *Water Res.* 168:115199. doi: 10.1016/j.watres.2019.115199

Chen, Y., Yu, B., Yin, C., Zhang, C., Dai, X., Yuan, H., et al. (2016). Biostimulation by direct voltage to enhance anaerobic digestion of waste activated sludge. *RSC Adv.* 6, 1581–1588. doi: 10.1039/c5ra24134k

Cheng, L., Ding, C., Li, Q., He, Q., Dai, L. R., and Zhang, H. (2013). DNA-SIP reveals that *Syntrophaceae* play an important role in methanogenic hexadecane degradation. *PLoS One* 8:e66784. doi: 10.1371/journal.pone.0066784

Cruz Viggi, C., Rossetti, S., Fazi, S., Paiano, P., Majone, M., and Aulenta, F. (2014). Magnetite particles triggering a faster and more robust syntrophic pathway of methanogenic propionate degradation. *Environ. Sci. Technol.* 48, 7536–7543. doi: 10.1021/es5016789

Curd, E. E., Martiny, J. B. H., Li, H. Y., and Smith, T. B. (2018). Bacterial diversity is positively correlated with soil heterogeneity. *Ecosphere* 9:e02079. doi: 10.1002/ecs2.2079

Da Silva, A. C., De Vleeschouwer, D., Boulvain, F., Claeys, P., Fagel, N., Humblet, M., et al. (2013). Magnetic susceptibility as a high-resolution correlation tool and as a climatic proxy in Paleozoic rocks – Merits and pitfalls: examples

from the Devonian in Belgium. *Mar. Petrol. Geol.* 46, 173–189. doi: 10.1016/j.marpetgeo.2013.06.012

Danczak, R. E., Johnston, M. D., Kenah, C., Slattery, M., and Wilkins, M. J. (2019). Capability for arsenic mobilization in groundwater is distributed across broad phylogenetic lineages. *PLoS One* 14:e0221694. doi: 10.1371/journal.pone.0221694

de Bok, F. A., Stams, A. J., Dijkema, C., and Boone, D. R. (2001). Pathway of propionate oxidation by a syntrophic culture of *Smithella propionica* and *Methanospirillum hungatei*. *Appl. Environ. Microbiol.* 67, 1800–1804. doi: 10.1128/AEM.67.4.1800-1804.2001

D'Emilio, M., Chianese, D., Coppola, R., Macchiato, M., and Ragosta, M. (2007). Magnetic susceptibility measurements as proxy method to monitor soil pollution: development of experimental protocols for field surveys. *Environ. Monitor. Assess.* 125, 137–146. doi: 10.1007/s10661-006-9246-1

Emmerton, S., Muxworthy, A. R., Sephton, M. A., Aldana, M., Costanzo-Alvarez, V., Bayona, G., et al. (2013). Correlating biodegradation to magnetization in oil bearing sedimentary rocks. *Geochim. Cosmochim. Acta* 112, 146–165. doi: 10.1016/j.gca.2013.03.008

Essaid, H. I., Bekins, B. A., Herkelrath, W. N., and Delin, G. N. (2011). Crude oil at the Bemidji site: 25 years of monitoring, modeling, and understanding. *Ground Water* 49, 706–726. doi: 10.1111/J.1745-6584.2009.00654.X

Finneran, K. T., Johnsen, C. V., and Lovley, D. R. (2003). *Rhodoferax ferrireducens* sp nov., a psychrotolerant, facultatively anaerobic bacterium that oxidizes acetate with the reduction of Fe(III). *Int. J. Syst. Evol. Micr.* 53, 669–673. doi: 10.1099/Ijs.0.02298-0

Grady, E. N., MacDonald, J., Liu, L., Richman, A., and Yuan, Z. C. (2016). Current knowledge and perspectives of *Paenibacillus*: a review. *Microb. Cell Fact.* 15:203. doi: 10.1186/s12934-016-0603-7

Gray, N. D., Sherry, A., Grant, R. J., Rowan, A. K., Hubert, C. R. J., Callbeck, C. M., et al. (2011). The quantitative significance of *Syntrophaceae* and syntrophic partnerships in methanogenic degradation of crude oil alkanes. *Environ. Microbiol.* 13, 2957–2975. doi: 10.1111/J.1462-2920.2011.02570.X

Guo, F., and Zhang, T. (2013). Biases during DNA extraction of activated sludge samples revealed by high throughput sequencing. *Appl. Microbiol. Biotechnol.* 97, 4607–4616. doi: 10.1007/s00253-012-4244-4

Guo, K., and Gao, P. (2020). *Do 16s Data Analysis and Generate Figures. Microbial.* R Package Version 0.0.17.

Guzmán, O., Costanzo-Álvarez, V., Aldana, M., and Díaz, M. (2011). Study of magnetic contrasts applied to hydrocarbon exploration in the Maturín Sub-Basin (eastern Venezuela). *Stud. Geophys. Geodaet.* 55, 359–376. doi: 10.1007/s11200-011-0020-7

Han, D., Dedysh, S. N., and Liesack, W. (2018). Unusual genomic traits suggest *Methylocystis bryophila S285* to be well adapted for life in peatlands. *Genome Biol. Evol.* 10, 623–628. doi: 10.1093/gbe/evy025

Hansel, C. M., Benner, S. G., and Fendorf, S. (2005). Competing Fe(II)-induced mineralization pathways of ferrihydrite. *Environ. Sci. Technol.* 39, 7147–7153. doi: 10.1021/Es050666z

Heenan, J. W., Ntarlagiannis, D., Slater, L. D., Beaver, C. L., Rossbach, S., Revil, A., et al. (2017). Field-scale observations of a transient geobattery resulting from natural attenuation of a crude oil spill. *J. Geophys. Res. Biogeosci.* 122, 918–929. doi: 10.1002/2016jg003596

Hernsdorf, A. W., and Amano, Y. (2017). Potential for microbial H2 and metal transformations associated with novel bacteria and archaea in deep terrestrial subsurface sediments. *ISME J.* 11, 1915–1929. doi: 10.1038/ismej.2017.39

Hoffmann, V., Knab, M., and Appel, E. (1999). Magnetic susceptibility mapping of roadside pollution. *J. Geochem. Explor.* 66, 313–326. doi: 10.1016/S0375-6742(99)00014-X

Jaffe, A. L., Castelle, C. J., Matheus Carnevali, P. B., Gribaldo, S., and Banfield, J. F. (2020). The rise of diversity in metabolic platforms across the Candidate Phyla Radiation. *BMC Biol.* 18:69. doi: 10.1186/s12915-020-00804-5

Ji, J. H., Zhou, L., Mbadinga, S. M., Irfan, M., Liu, Y. F., Pan, P., et al. (2020). Methanogenic biodegradation of C9 to C12n-alkanes initiated by *Smithella* via fumarate addition mechanism. *AMB Exp.* 10:23. doi: 10.1186/s13568-020-0956-5

Kato, S., Hashimoto, K., and Watanabe, K. (2012). Methanogenesis facilitated by electric syntrophy via (semi)conductive iron-oxide minerals. *Environ. Microbiol.* 14, 1646–1654. doi: 10.1111/j.1462-2920.2011.02611.x

Kato, S., Wada, K., Kitagawa, W., Mayumi, D., Ikarashi, M., Sone, T., et al. (2019). Conductive iron oxides promote methanogenic acetate degradation by microbial communities in a high-temperature petroleum reservoir. *Microb. Environ.* 34, 95–98. doi: 10.1264/jsme2.ME18140

Kim, K. K., Lee, K. C., Oh, H. M., Kim, M. J., Eom, M. K., and Lee, J. S. (2008). *Arthrobacter defluvii* sp. nov., 4-chlorophenol-degrading bacteria isolated from sewage. *Int. J. Syst. Evol. Microbiol.* 58, 1916–1921. doi: 10.1099/ijs.0.65550-0

Kobayashi, H., Fu, Q., Maeda, H., and Sato, K. (2017). Draft genome sequence of a novel *Coriobacteriaceae* sp. Strain, EMTCatB1, reconstructed from the metagenome of a thermophilic electromethanogenic biocathode. *Genome Announc.* 5:e00022-17. doi: 10.1128/genomeA.00022-17

Langille, M. G., Zaneveld, J., Caporaso, J. G., McDonald, D., Knights, D., Reyes, J. A., et al. (2013). Predictive functional profiling of microbial communities using 16S rRNA marker gene sequences. *Nat. Biotechnol.* 31, 814–821. doi: 10.1038/nbt.2676

Lentini, C. J., Wankel, S. D., and Hansel, C. M. (2012). Enriched iron(III)-reducing bacterial communities are shaped by carbon substrate and iron oxide mineralogy. *Front. Microbiol.* 3:404. doi: 10.3389/Fmicb.2012.00404

Li, Y., Huang, C., Ngo, H. H., Pang, J., Zha, X., Liu, T., et al. (2019). In situ reconstruction of long-term extreme flooding magnitudes and frequencies based on geological archives. *Sci. Total Environ.* 670, 8–17. doi: 10.1016/j.scitotenv.2019.03.066

Liu, Y. T., Balkwill, D. L., Aldrich, H. C., Drake, G. R., and Boone, D. R. (1999). Characterization of the anaerobic propioate-degrading syntrophs *Smithella propionica* gen. nov., sp. nov. and *Syntrophobacter wolinii*. *Int. J. Syst. Bacteriol.* 49, 545–556. doi: 10.1099/00207713-49-2-545

Lovley, D. R. (2017). Syntrophy goes electric: direct interspecies electron transfer. *Annu. Rev. Microbiol.* 71, 643–664. doi: 10.1146/annurev-micro-030117-020420

Lovley, D. R., Baedecker, M. J., Lonergan, D. J., Cozzarelli, I. M., Phillips, E. J. P., and Siegel, D. I. (1989). Oxidation of aromatic contaminants coupled to microbial iron reduction. *Nature* 339, 297–300. doi: 10.1038/339297a0

Lund, A. L., Slater, L. D., Atekwana, E. A., Ntarlagiannis, D., Cozzarelli, I., and Bekins, B. A. (2017). Evidence of coupled carbon and iron cycling at a hydrocarbon-contaminated site from time lapse magnetic susceptibility. *Environ. Sci. Technol.* 51, 11244–11249. doi: 10.1021/acs.est.7b02155

Masella, A. P., Bartram, A. K., Truszkowski, J. M., Brown, D. G., and Neufeld, J. D. (2012). PANDAseq: paired-end assembler for illumina sequences. *BMC Bioinform.* 13:31. doi: 10.1186/1471-2105-13-31

Mattes, T. E., Alexander, A. K., Richardson, P. M., Munk, A. C., Han, C. S., Stothard, P., et al. (2008). The genome of *Polaromonas* sp. strain JS666: insights into the evolution of a hydrocarbon- and xenobiotic-degrading bacterium, and features of relevance to biotechnology. *Appl. Environ. Microbiol.* 74, 6405–6416. doi: 10.1128/AEM.00197-08

McMurdie, P. J., and Holmes, S. (2013). phyloseq: an R package for reproducible interactive analysis and graphics of microbiome census data. *PLoS One* 8:e61217. doi: 10.1371/journal.pone.0061217

Meckenstock, R. U., Elsner, M., Griebler, C., Lueders, T., Stumpp, C., Aamand, J., et al. (2015). Biodegradation: updating the concepts of control for microbial cleanup in contaminated aquifers. *Environ. Sci. Technol.* 49, 7073–7081. doi: 10.1021/acs.est.5b00715

Mewafy, F. M., Atekwana, E. A., Werkema, D. D., Slater, L. D., Ntarlagiannis, D., Revil, A., et al. (2011). Magnetic susceptibility as a proxy for investigating microbially mediated iron reduction. *Geophys. Res. Lett.* 38:L21402. doi: 10.1029/2011gl049271

Murrell, P. (2005). *R Graphics*. Boca Raton, FL: CRC Press.

Oksanen, J., Blanchet, F. G., Kindt, R., Legendre, P., Minchin, P. R., O'Hara, R. B., et al. (2013). "*Vegan: Community Ecology Package*". R Package Version 2.0-10.

Perez-Perez, A., D'Onofrio, L., Bosch, M., and Zapata, E. (2011). Association between magnetic susceptibilities and hydrocarbon deposits in the Barinas-Apure Basin, Venezuela. *Geophysics* 76:L35. doi: 10.1190/geo2010-0274.1

Piepenbrock, A., Dippon, U., Porsch, K., Appel, E., and Kappler, A. (2011). Dependence of microbial magnetite formation on humic substance and ferrihydrite concentrations. *Geochim. Cosmochim. Acta* 75, 6844–6858. doi: 10.1016/j.gca.2011.09.007

Porsch, K., Dippon, U., Rijal, M. L., Appel, E., and Kappler, A. (2010). In-situ magnetic susceptibility measurements as a tool to follow geomicrobiological transformation of Fe minerals. *Environ. Sci. Technol.* 44, 3846–3852. doi: 10.1021/es903954u

Potter, D. K. (2007). Magnetic susceptibility as a rapid, nondestructive technique for improved petrophysical parameter prediction. *Petrophysics* 48, 191–201.

Potter, D. K., and Ivakhnenko, O. P. (2008). Clay typing – Sensitive quantification and anisotropy in synthetic and natural reservoir samples using low- and high-field magnetic susceptibility for improved petrophysical appraisals. *Petrophysics* 49, 57–66.

Qin, Q. S., Feng, D. S., Liu, P. F., He, Q., Li, X., Liu, A. M., et al. (2017). Metagenomic characterization of *Candidatus* Smithella cisternae Strain M82_1, a syntrophic alkane-degrading bacteria, enriched from the Shengli Oil Field. *Microb. Environ.* 32, 234–243. doi: 10.1264/jsme2.ME17022

R Core Team (2016). *"R: A Language and Environment for Statistical Computing"*. R Version 3.3.2. Vienna: R Foundation for Statistical Computing.

Reed, D. W., Fujita, Y., Delwiche, M. E., Blackwelder, D. B., Sheridan, P. P., Uchida, T., et al. (2002). Microbial communities from methane hydrate-bearing deep marine sediments in a forearc basin. *Appl. Environ. Microbiol.* 68, 3759–3770. doi: 10.1128/aem.68.8.3759-3770.2002

Revil, A., Mendonca, C. A., Atekwana, E. A., Kulessa, B., Hubbard, S. S., and Bohlen, K. J. (2010). Understanding biogeobatteries: where geophysics meets microbiology. *J. Geophys. Res. Biogeosci.* 115:G00G02. doi: 10.1029/2009jg001065

Rijal, M. L., Appel, E., Petrovsky, E., and Blaha, U. (2010). Change of magnetic properties due to fluctuations of hydrocarbon contaminated groundwater in unconsolidated sediments. *Environ. Pollut.* 158, 1756–1762. doi: 10.1016/j.envpol.2009.11.012

Rijal, M. L., Porsch, K., Appel, E., and Kappler, A. (2012). Magnetic signature of hydrocarbon-contaminated soils and sediments at the former oil field Hanigsen, Germany. *Stud. Geophys. Geod.* 56, 889–908. doi: 10.1007/S11200-010-0040-8

Robertson, W. J., Franzmann, P. D., and Mee, B. J. (2000). Spore-forming, *Desulfosporosinus*-like sulphate-reducing bacteria from a shallow aquifer contaminated with gasolene. *J. Appl. Microbiol.* 88, 248–259. doi: 10.1046/j.1365-2672.2000.00957.x

Rognes, T., Flouri, T., Nichols, B., Quince, C., and Mahe, F. (2016). VSEARCH: a versatile open source tool for metagenomics. *PeerJ* 4:e2584. doi: 10.7717/peerj.2584

Rotaru, A. E., Shrestha, P. M., Liu, F., Markovaite, B., Chen, S., Nevin, K. P., et al. (2014). Direct interspecies electron transfer between *Geobacter metallireducens* and *Methanosarcina barkeri*. *Appl. Environ. Microbiol.* 80, 4599–4605. doi: 10.1128/Aem.00895-14

Ryu, S. H., Chung, B. S., Le, N. T., Jang, H. H., Yun, P. Y., Park, W., et al. (2008). *Devosia geojensis* sp. nov., isolated from diesel-contaminated soil in Korea. *Int. J. Syst. Evol. Microbiol.* 58, 633–636. doi: 10.1099/ijs.0.65481-0

Segata, N., Izard, J., Waldron, L., Gevers, D., Miropolsky, L., Garrett, W. S., et al. (2011). Metagenomic biomarker discovery and explanation. *Genome Biol.* 12:R60. doi: 10.1186/gb-2011-12-6-r60

Shang, H., Daye, M., Sivan, O., Borlina, C. S., Tamura, N., Weiss, B. P., et al. (2020). Formation of zerovalent iron in iron-reducing cultures of *Methanosarcina barkeri*. *Environ. Sci. Technol.* 54, 7354–7365. doi: 10.1021/acs.est.0c01595

Shi, L. D., Chen, Y. S., Du, J. J., Hu, Y. Q., Shapleigh, J. P., and Zhao, H. P. (2018). Metagenomic evidence for a *Methylocystis* species capable of bioremediation of diverse heavy metals. *Front. Microbiol.* 9:3297. doi: 10.3389/fmicb.2018.03297

Sivan, O., Shusta, S. S., and Valentine, D. L. (2016). Methanogens rapidly transition from methane production to iron reduction. *Geobiology* 14, 190–203. doi: 10.1111/gbi.12172

Solden, L., Lloyd, K., and Wrighton, K. (2016). The bright side of microbial dark matter: lessons learned from the uncultivated majority. *Curr. Opin. Microbiol.* 31, 217–226. doi: 10.1016/j.mib.2016.04.020

Tan, B., Nesbo, C., and Foght, J. (2014). Re-analysis of omics data indicates *Smithella* may degrade alkanes by addition to fumarate under methanogenic conditions. *ISME J.* 8, 2353–2356. doi: 10.1038/ismej.2014.87

Tian, R., Ning, D., He, Z., Zhang, P., Spencer, S. J., Gao, S., et al. (2020). Small and mighty: adaptation of superphylum *Patescibacteria* to groundwater environment drives their genome simplicity. *Microbiome* 8:51. doi: 10.1186/s40168-020-00825-w

Trost, J. J., Christy, T. M., and Bekins, B. A. (2018). A direct-push freezing core barrel for sampling unconsolidated subsurface sediments and adjacent pore fluids. *Vadose Zone J.* 17:180037. doi: 10.2136/vzj2018.02.0037

U. S. Geological Survey (2020). *National Water Information System Data Available on the World Wide Web (USGS Water Data for the Nation)*. Available online at: https://mn.water.usgs.gov/projects/bemidji/data/WaterQuality/BemidjiQW.zip (accessed June 10, 2012).

Walach, G., Scholger, R., and Cech, B. (2011). Geomagnetic and geoelectric prospection on a roman iron production facility in Huttenberg, Austria (Ferrum Noricum). *Archaeol. Prospect.* 18, 149–158. doi: 10.1002/arp.412

Wawrik, B., Marks, C. R., Davidova, I. A., McInerney, M. J., Pruitt, S., Duncan, K. E., et al. (2016). Methanogenic paraffin degradation proceeds via alkane addition to fumarate by '*Smithel*' spp. mediated by a syntrophic coupling with hydrogenotrophic methanogens. *Environ. Microbiol.* 18, 2604–2619. doi: 10.1111/1462-2920.13374

Wegner, C.-E., Gorniak, L., Riedel, S., Westermann, M., and Küsel, K. (2020). Lanthanide-dependent methylotrophs of the family *Beijerinckiaceae*: physiological and genomic insights. *Appl. Environ. Microbiol.* 86, e1830–e1819. doi: 10.1128/aem.01830-19

Wickham, H. (2009). *ggplot2: Elegant Graphics for Data Analysis*. New York, NY: Springer.

Wickham, H. (2011). The split-apply-combine strategy for data analysis. *J. Statist. Softw.* 40, 1–29.

Wickham, H., Averick, M., Bryan, J., Chang, W., D'Agostino McGowan, L., François, R., et al. (2019). Welcome to the tidyverse. *J. Open Sour. Softw.* 4:1686. doi: 10.21105/joss.01686

Wilkie, C. (2019). *cowplot: Streamlined Plot Theme and Plot Annotations for "ggplot2"* R Package Version 1.0.0. Available online at: https://CRAN.R-project.org/package=cowplot (accessed November 1, 2020).

Woycheese, K. M., Meyer-Dombard, D. R., Cardace, D., Argayosa, A. M., and Arcilla, C. A. (2015). Out of the dark: transitional subsurface-to-surface microbial diversity in a terrestrial serpentinizing seep (Manleluag, Pangasinan, the Philippines). *Front. Microbiol.* 6:44. doi: 10.3389/fmicb.2015.00044

Xia, X., Zhang, J., Song, T., and Lu, Y. (2019). Stimulation of *Smithella*-dominating propionate oxidation in a sediment enrichment by magnetite and carbon nanotubes. *Environ. Microbiol. Rep.* 11, 236–248. doi: 10.1111/1758-2229.12737

Yamada, C., Kato, S., Ueno, Y., Ishii, M., and Igarashi, Y. (2015). Conductive iron oxides accelerate thermophilic methanogenesis from acetate and propionate. *J. Biosci. Bioeng.* 119, 678–682. doi: 10.1016/j.jbiosc.2014.11.001

Yang, Z. M., Shi, X. S., Wang, C. S., Wang, L., and Guo, R. B. (2015). Magnetite nanoparticles facilitate methane production from ethanol via acting as electron acceptors. *Sci. Rep.* 5:16118. doi: 10.1038/srep16118

Yashiro, Y., Sakai, S., Ehara, M., Miyazaki, M., Yamaguchi, T., and Imachi, H. (2011). *Methanoregula formicica* sp. nov., a methane-producing archaeon isolated from methanogenic sludge. *Int. J. Syst. Evol. Microbiol.* 61(Pt 1), 53–59. doi: 10.1099/ijs.0.014811-0

Zavarzina, D. G., Sokolova, T. G., Tourova, T. P., Chernyh, N. A., Kostrikina, N. A., and Bonch-Osmolovskaya, E. A. (2007). *Thermincola ferriacetica* sp nov., a new anaerobic, thermophilic, facultatively chemolithoautotrophic bacterium capable of dissimilatory Fe(III) reduction. *Extremophiles* 11, 1–7. doi: 10.1007/S00792-006-0004-7

Zhang, B. L., Wu, X. K., Zhang, G. S., Li, S. Y., Zhang, W., Chen, X. M., et al. (2016). The diversity and biogeography of the communities of Actinobacteria

in the forelands of glaciers at a continental scale. *Environ. Res. Lett.* 11:054012. doi: 10.1088/1748-9326/11/5/054012

Zhang, H., Sekiguchi, Y., Hanada, S., Hugenholtz, P., Kim, H., Kamagata, Y., et al. (2003). *Gemmatimonas aurantiaca* gen. nov., sp. nov., a gram-negative, aerobic, polyphosphate-accumulating micro-organism, the first cultured representative of the new bacterial phylum Gemmatimonadetes phyl. nov. *Int. J. Syst. Evol. Microbiol.* 53(Pt 4), 1155–1163. doi: 10.1099/ijs.0.02520-0

Zhang, J., and Lu, Y. (2016). Conductive Fe3O4 nanoparticles accelerate syntrophic methane production from butyrate oxidation in two different lake sediments. *Front. Microbiol.* 7:1316. doi: 10.3389/fmicb.2016.01316

Zhang, W., Appel, E., Fang, X., Yan, M., Song, C., and Cao, L. (2012). Paleoclimatic implications of magnetic susceptibility in Late Pliocene–Quaternary sediments from deep drilling core SG-1 in the western Qaidam Basin. *J. Geophys. Res.* 117:B06101. doi: 10.1029/2011JB008949

Zhou, J., Bruns, M. A., and Tiedje, J. M. (1996). DNA recovery from soils of diverse composition. *Appl. Environ. Microbiol.* 62, 316–322. doi: 10.1128/AEM.62.2.316-322.1996

Zhuang, L., Tang, J., Wang, Y., Hu, M., and Zhou, S. (2015). Conductive iron oxide minerals accelerate syntrophic cooperation in methanogenic benzoate degradation. *J. Hazard Mater.* 293, 37–45. doi: 10.1016/j.jhazmat.2015.03.039

Conflict of Interest: The authors declare that this study received funding from Chevron Energy Technology (Grant No. CW852844) and the National Crude Oil Spill Fate and Natural Attenuation Research Site, a collaborative venture of the United States Geological Survey (USGS), Enbridge Energy, Limited Partnership, the Minnesota Pollution Control Agency, and Beltrami County. The funders were not involved in the study design, collection, analysis, interpretation of data, the writing of this article, or the decision to submit it for publication.

frontiers in Earth Science

ORIGINAL RESEARCH
published: 30 April 2021
doi: 10.3389/feart.2021.634482

Magnetic Mineralogy of Speleothems From Tropical-Subtropical Sites of South America

Plinio Jaqueto[1], Ricardo I. F. Trindade[1], Joshua M. Feinberg[2], Janine Carmo[1], Valdir F. Novello[3], Nicolás M. Stríkis[4], Francisco W. Cruz[3], Marília H. Shimizu[5] and Ivo Karmann[3]*

[1] Departamento de Geofísica, Instituto de Astronomia, Geofísica e Ciências Atmosféricas, Universidade de São Paulo (USPmag), São Paulo, Brazil, [2] Department of Earth and Environmental Sciences, Institute for Rock Magnetism, University of Minnesota, Minneapolis, MN, United States, [3] Instituto de Geociências, Universidade de São Paulo, São Paulo, Brazil, [4] Departamento de Geoquímica, Universidade Federal Fluminense, Niterói, Brazil, [5] Center for Weather Forecasting and Climate Studies (CPTEC), National Institute for Space Research (INPE), Cachoeira Paulista, Brazil

Fe-bearing minerals are a tiny fraction of the composition of speleothems. They have their origin in the karst system or are transported from the drainage basin into the cave. Recent studies on the magnetism of speleothems focused on the variations of their magnetic mineralogy in specific time intervals and are usually limited to a single sample. In this study, we describe a database of environmental magnetism parameters built from 22 stalagmites from different caves located in Brazil (South America) at different latitudes, comprising different climates and biomes. The magnetic signal observed in these stalagmites is dominated by low-coercivity minerals (~20 mT) whose magnetic properties resemble those of the magnetite formed in pedogenic environments. Also, a comparison with few samples from soils and the carbonate from cave's walls shows a good agreement of the magnetic properties of speleothems with those of soil samples, reinforcing previous suggestions that in (sub-)tropical regimes, the dominant magnetic phase in speleothems is associated with the soil above the cave. Spearman's rank correlation points to a positive strong correlation between magnetic concentration parameters (mass-normalized magnetic susceptibility, natural remanent magnetization, anhysteretic remanent magnetization, and isothermal remanent magnetization). This implies that ultrafine ferrimagnetic minerals are the dominant phase in these (sub-)tropical karst systems, which extend across a diverse range of biomes. Although the samples are concentrated in the savannah biome (Cerrado) (~70%), comparison with other biomes shows a higher concentration of magnetic minerals in speleothem underlying savannahs and lower concentration in those underlying moist broadleaf forests (Atlantic and Amazon biome) and dry forests (Caatinga). Thus, rainfall, biome, and epikarst dynamics play an important role in the concentration of magnetic minerals in speleothems in (sub-)tropical sites and indicate they can be an important target for paleoenvironmental research in cave systems.

Keywords: environmental magnetism, speleothem magnetism, South America, rock magnetism, karst system, stalagmites

OPEN ACCESS

Edited by:
Leonardo Sagnotti, Istituto Nazionale di Geofisica e Vulcanologia (INGV), Italy

Reviewed by:
Eric Font, University of Coimbra, Portugal
Luca Lanci, University of Urbino Carlo Bo, Italy

****Correspondence:***
Plinio Jaqueto
plinio.jaqueto@iag.usp.br

Specialty section:
This article was submitted to Geomagnetism and Paleomagnetism, a section of the journal Frontiers in Earth Science

Received: *27 November 2020*
Accepted: *06 April 2021*
Published: *30 April 2021*

Citation:
Jaqueto P, Trindade RIF, Feinberg JM, Carmo J, Novello VF, Stríkis NM, Cruz FW, Shimizu MH and Karmann I (2021) Magnetic Mineralogy of Speleothems From Tropical-Subtropical Sites of South America. Front. Earth Sci. 9:634482. doi: 10.3389/feart.2021.634482

INTRODUCTION

Speleothems, together with ice-cores, are among the best continental records used in paleoclimate and paleoenvironment reconstruction thanks to their precise chronology, widespread geographic distribution, and continuous growth. Environmental magnetic studies of speleothems show variations in the magnetic mineral concentrations that correlate with the decadal- to millennial-scale climate fluctuations at regional and/or global scales (**Table 1**; Xie et al., 2013; Bourne et al., 2015; Jaqueto et al., 2016; Zhu et al., 2017; Chen et al., 2019; Regattieri et al., 2019). The magnetic mineral assemblage and the relative concentration of different magnetic phases in speleothems can be interpreted in terms of **Figure 1**: (i) atmospheric processes (rainfall and temperature), (ii) epikarst processes (soil formation, vegetation change, soil pCO_2, and rate of carbonate dissolution), (iii) allochthonous detrital input, including flooding events or wind-blown particles, and (iv) modification of the magnetic mineralogy *in situ*, in the speleothem.

Precipitation is a major factor in speleothem formation. The karst system encompasses dissolution and precipitation regimes related to the carbonate–water interactions (Fairchild et al., 2006). The dissolution phase operates as a cascading system, comprising the atmosphere, the soil ecosystem, the epikarst, and the cave system itself (Fairchild and Baker, 2012). It involves the transformation of carbon dioxide gas [$CO_{2(g)}$] that dissolves into water to form the species [$CO_{2(aq)}$] reacting with water to form carbonic acid (H_2CO_3). This "weak" acid will progressively dissolve the limestone ($CaCO_3$), and this reaction will produce calcium (Ca^{2+}) and bicarbonate (HCO_3^-). At the precipitation phase, in the cave system, degassing of CO_2 will occur (when the solution is in contact with the cave atmosphere), and the secondary carbonate will form ($CaCO_3$), mainly calcite. The kinetics of the degassing reaction during calcite precipitation usually lasts from minutes to hours (Dreybrodt et al., 1997; Dreybrodt, 1999; Dreybrodt and Scholz, 2011) and favors the acquisition of detrital remanent magnetization. Furthermore, the absence of postdepositional perturbation, like bioturbation or

TABLE 1 | Speleothem magnetism studies and their respective resolution and interpretation.

Study	Location	Climatology	Cave	Sample	Timespan	Average sample resolution	Magnetic parameter	Comparison	Interpretation
Xie et al., 2013	China	Monsoonal, warm-wet summer and a cool-dry winter	Heshang Cave	HS4	0.15 ka–7.10 ka (6.94 ka)	74 years	ARM/SIRM	Peatlands Hopanoids	Heavy rainfall resulted in the enhanced transport of coarse magnetic particles to the cave
Zhu et al., 2017	China	Eastern Asian and Indian monsoon systems	Heshang Cave	HS4	0.15 ka–7.10 ka (6.94 ka)	74 years	IRMsoft_flux	δ13C, Peatlands Hopanoids, ENSO variability, stalagmite BA03 – δ18O, and core V21-30 – δ18O foraminifera	Flux of soil-derived magnetic minerals correlate with rainfall amount and intensity
Bourne et al., 2015	United States	Humid, temperate climate, and well-developed, midlatitude seasonality	Buckeye Creek Cave	BCC-010	58.71 ka–125.21 ka (66.49 ka)	2015 years	IRMsoft, SIRM, IRMhard, S-ratio, IRM0.3T	δ13C, δ18O, Antarctic ice core CO_2, and Vostok ice core CO_2	Changes in magnetite concentration as reflecting variations in local pedogenic processes, controlled by changes in regional precipitation
Jaqueto et al., 2016	Brazil	South America Summer Monsoon with 90% of this amount falling	Pau D'Alho Cave	ALHO06	1891 CE–535 CE (1.35 ka)	40 years	NRM, ARM, SIRM, HIRM, IRM_soft, S-ratio, ARM/SIRM	δ13C and δ18O	Concentration of magnetic minerals in the stalagmite is governed by soil erosion above the cave
Chen et al., 2019	China	Subtropical monsoon climate, more than 65% rainfall falls during the monsoon season	Tangnei Cave	TN-1	77.9 ka to 82.3 ka (3.04 ka)	15 years	Ms and Hc	δ13C, δ18O, and solar variability	Magnetic property in speleothems is interpreted to be related to regional precipitation
Regattieri et al., 2019	Italy	Alpine climate, with precipitation correlated with southern Europe	Rio Martino Cave	RMD1	0.4 ka to 9.7 ka (9.3 ka)	60 years	Magnetic susceptibility	δ13C, δ18O, growth rate, and lake level	Magnetic susceptibility concentration and carbon stable isotope ratio related to soil stability and pedogenesis

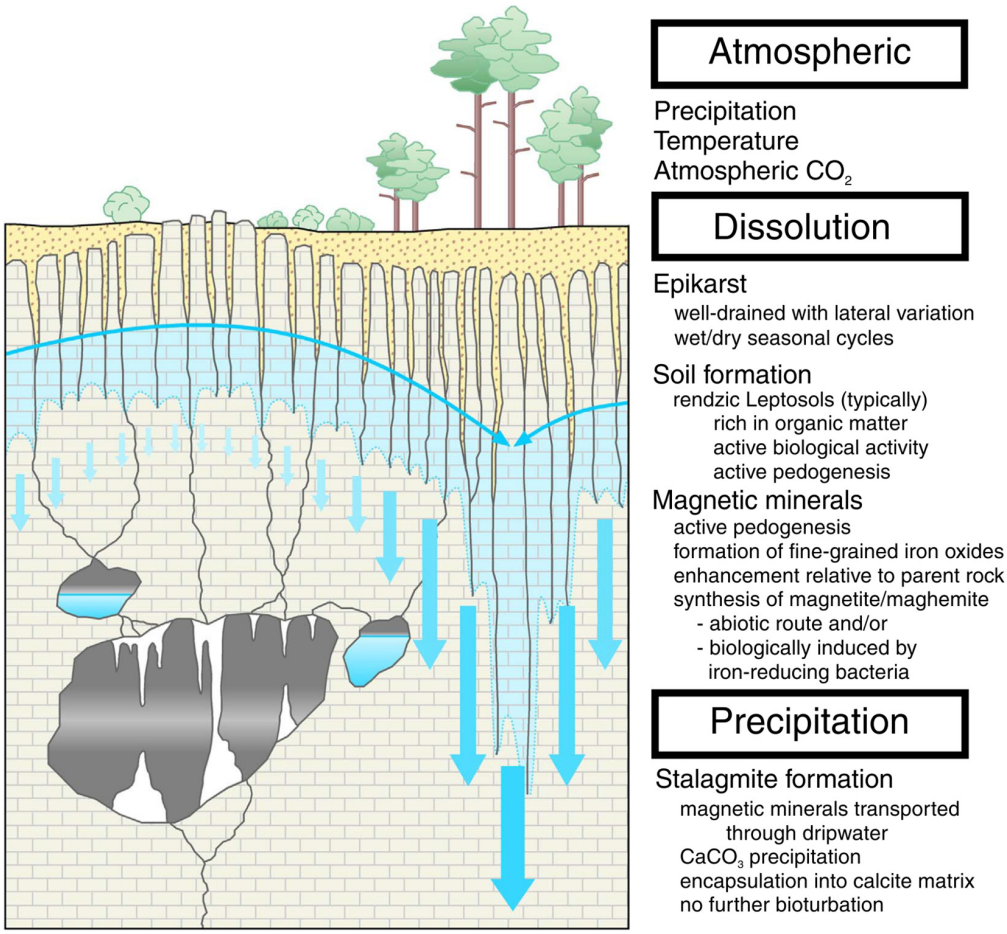

FIGURE 1 | Schematic description of the karst vadose zone (Hartmann and Baker, 2017), with processes that are related to the speleothem magnetism.

compaction, helps conserve the magnetic remanence and allows the speleothem to retain reliable, directional, and paleointensity data (Lascu et al., 2016; Trindade et al., 2018; Zanella et al., 2018).

Soils play an important role in speleothem formation since the microbial activity of the soil and root respiration are the main factors controlling the pCO_2 in the solution, which in turn will drive carbonate dissolution (epikarst). In karst environments, soils are generally classified as Rendzina soils [Leptosols developed in carbonates (Jordanova, 2017)]. They develop over 10 to 100 years with a thin humic (A) horizon, overlying an incipient illuvial (B) horizon or the bedrock itself, and are often well drained with good aeration and a brown-to-black soil color (Jordanova, 2017). The combination of well-drained soil together with a large amount of organic and enhanced biological activity will promote an active pedogenesis producing fine-grained pedogenic iron oxides (SP/SSD magnetite fraction) with the magnetic enhancement of the soil relative to the host carbonate (**Figure 1**). So, the synthesis of pedogenic magnetite/maghemite via an abiotic route or via iron-reducing bacteria will be controlled by the characteristics of the biome and by the wetting and drying cycles in the soil (Jaqueto et al., 2016; Maxbauer et al., 2016a; Jordanova, 2017).

Transport of small-sized detrital particles derived from the soil into the cave system will occur through diffusive infiltration (**Figure 1**) along the fissures of the rock. These particles will be incorporated into the speleothem after reaching the top of the stalagmite by drip water (Bosch and White, 2004; Font et al., 2014; Bourne et al., 2015; Jaqueto et al., 2016; Zhu et al., 2017; Regattieri et al., 2019; Fu et al., 2021). Alternatively, detrital particles may reach the speleothems from sinking streams and from detrital material stored in the conduit system, or may result from flooded surface steams and episodic storm flows (Bosch and White, 2004; Feinberg et al., 2020). Also, detrital input close to cave entrances can be derived from wind-blown material (pollen and dust) (Fairchild et al., 2006). Finally, authigenic formation cannot be ruled out in some cases with the formation of goethite needles and biogenic magnetite at the precipitation site (Perkins, 1996; Strauss et al., 2013).

Most studies dealing with the environmental magnetism of speleothems interpret the variations in magnetic mineral concentration as a proxy for paleoprecipitation (**Table 1**). For example, Xie et al. (2013); Bourne et al. (2015), and Zhu et al. (2017) show a millennial-scale correlation between magnetic parameters and proxies for paleoprecipitation in

China and the southwest United States. Chen et al. (2019) used saturation magnetization (Ms) to track rainfall variation during MIS5a/4 transition, and the power spectrum of Ms showed that solar activity plays an important role in precipitation variation in southern China. More recently, Regattieri et al. (2019) linked climate proxies (with stable oxygen and carbon isotope) soil stability and evolution (magnetic parameters), and land-use on a Holocene speleothem from northern Italy.

In tropical sites, Jaqueto et al. (2016) suggested an inverse correlation at the multidecadal scale between paleoprecipitation and magnetic mineral concentration in a speleothem from western Brazil. In their model, the concentration of magnetic minerals in the stalagmite was governed by soil erosion and vegetation cover. A period of less rainfall (compared to the average) would be associated with less stable soils, resulting in higher fluxes of magnetic minerals into karst systems. Conversely, wetter periods would be associated with denser vegetation that inhibits the flux of the detritic material of the soil into the cave. In this case, the relation between paleoprecipitation and magnetic mineral concentration is not a direct one and depends on the soil dynamics and the vegetation cover in addition to the regional climate.

In the present study, we will explore the variations of magnetic mineralogy through different biomes in South America through a large speleothem magnetism database covering a wide range of latitudes (4°S to 24°S). Also, we present two detailed case studies where the magnetic signal of the speleothems is compared to the soil above the cave and the host carbonate to constraint the source of magnetic minerals inside the speleothems.

REGIONAL SETTING

The central part of South America is dominated by warm and humid conditions, where the South America Summer Monsoon (SASM) is responsible for 70% of the rainfall from November to February (Garreaud et al., 2009; Campos et al., 2019). Present-day interannual climate variability is controlled by the El-Niño Southern Oscillation associated with the warmer conditions and rainfall below average on the northern part and wetter conditions on the southeastern part. Decadal and interdecadal variability is also present and is forced by the Pacific Decadal Oscillation with smaller amplitudes (Garreaud et al., 2009), while the paleoclimate reconstitution of the SASM based in $\delta^{18}O$ of the speleothems showed strong centennial variability linked to solar cycles (Novello et al., 2016).

The biomes at each karst system have different biodiversities like plant structure (trees vs. grasses), leaf type (broad vs. needles), plant spacing (forest vs. savannah), and climate that controls the organism type. Four main biomes are present in the main karst areas in Brazil (**Figure 2**; Ribeiro et al., 1983; Whitmore and Prance, 1987; Olson et al., 2001):

(1) Amazon biome (moist broadleaf forest), located in the north and northwestern part of Brazil, is characterized by low variability in temperature with a higher precipitation amount between 1,800 and 2,200 mm/year. Its ecoregion is classified as Neotropical, with high biodiversity; forest composition is dominated by evergreen trees with a dense high canopy; and the transition on its border is characterized by less dense understory.
(2) Cerrado biome (savannah), located in the Central part of Brazil, is characterized by seasonal rainfall, with a dry period during winter and a humid period in summer with average precipitation between 1,000 and 1,500 mm/year. Its ecoregion is classified as Neotropical, and it has a border with other biomes (Amazon, Atlantic, and Caatinga). The vegetation has characteristics of nutrient-poor, deep, and well-drained soils. Forest composition varies from an open field to a tall closed forest, which gives a distinctive biota feature in a mosaic fashion.
(3) Caatinga biome (dry forest), located in the northeastern part of Brazil, is characterized by a hot and dry climate with a precipitation amount between 700 and 750 mm/year (6–11 dry months). Its ecoregion is classified as Neotropical, and forest composition is considered heterogeneous, sparse, and diverse, ranging from low shrubby to tall caatinga forest.
(4) Atlantic biome (moist broadleaf forest), located in the southwestern part of Brazil along the southern coast, is characterized by high levels of rainfall between 1,600 and 1,800 mm/year. Its ecoregion is classified as Neotropical, with outstanding biodiversity in endemism. Forest ranges from coastal plains to the highest mountains, creating a vegetational gradient from shrubs to montane forests.

MATERIALS AND METHODS

South American caves occur over a wide range of latitudes, and the speleothems within them act as climate archives extending back hundreds of millennia (Cruz et al., 2005). The choice of selected caves for this study was based on the availability of speleothems held at the Instituto de Geociências from Universidade de São Paulo and also the aim to sample different biomes (**Figure 2** and **Supplementary Figure 1**). In general, four specimens of each stalagmite were prepared with ∼7.5 mm of diameter and ∼10 mm of height (**Supplementary Figures 2–5**) (specimens do not have a radiometric age control). The resulting speleothem database (**Figure 2**) consists of 139 specimens (**Supplementary Table 1**), where 90 specimens were prepared from 22 different speleothems, 34 specimens from soil samples from the epikarst of 4 caves, and 15 specimens from the host carbonate of two different caves. In two specific sites (pink squares, **Figure 2**), Jaraguá Cave (21.09°S, 56.58°W) and Lapa dos Anjos (15.44°S, 44.40°W), the samples consist of the stalagmite, soil, and carbonate.

ROCK MAGNETIC PARAMETERS

Rock magnetism techniques are commonly used in environmental studies aiming to understand three different

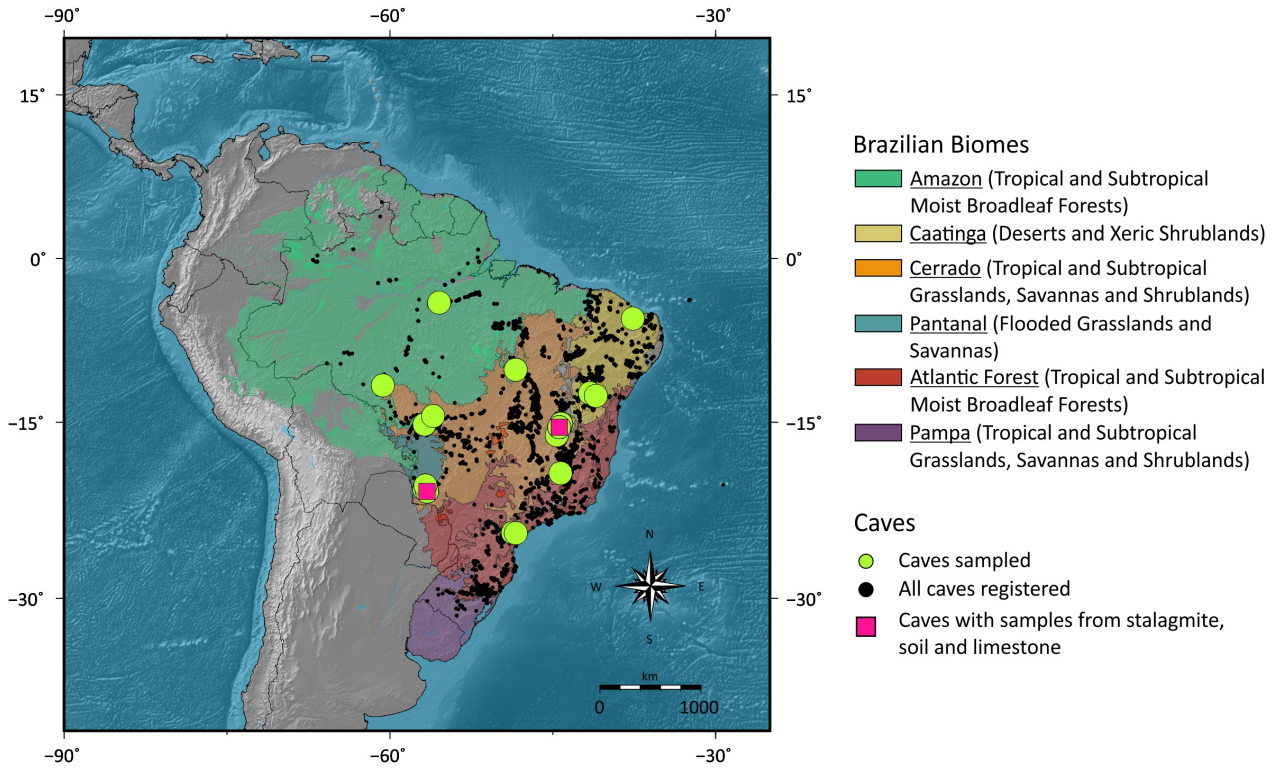

FIGURE 2 | Map of South America, with Brazilian caves (black dots), the speleothems sampled (green circles), and the caves with samples from a stalagmite, soil, and carbonate (pink squares) for rock magnetic characterization in different biomes (Cerrado, Caatinga, Amazon, Atlantic Forest, Pantanal, and Pampa) (Olson et al., 2001).

parameters: composition, concentration, and granulometry (Evans and Heller, 2003). Magnetic concentration parameters include mass-normalized values of magnetic susceptibility (χ), natural remanent magnetization (NRM), anhysteretic remanent magnetization (ARM), and isothermal remanent magnetization (IRM). Although they are referred to be concentration dependent, each of these parameters has different segments of grain size distribution and magnetic mineralogy in a sample. Magnetic susceptibility is the induced magnetization created by a small applied field, and in case of speleothems, it is influenced by ferromagnetic minerals, diamagnetic carbonates, and paramagnetic minerals from clays and silts. NRM is the total natural remanence held by low-coercivity minerals [10 s of mT by (titano)-magnetite/maghemite] as well as by high-coercivity minerals (100 s to 1,000 s of mT by hematite and goethite). Laboratory-induced remanences are useful for tracking a variety of other characteristics. ARM is the magnetization acquired during the application of a small DC field superimposed over an alternating field (AF) demagnetization step. ARM activates only those grains whose coercivities are less than the peak field reached during the AF step and that usually possess lower coercivity minerals such as magnetite and maghemite. IRM is the magnetization acquired after the application of a strong DC-pulsed field. Depending on the strength of the pulsed field, IRMs may include the saturation remanence of all low-coercivity minerals and portions of the hematite grain size distribution (which typically requires field up to ∼5 T to saturate). Goethite has a coercivity of >57 T (Rochette et al., 2005), and therefore, its remanence is not included in an IRM. Generally, IRM is interpreted as an indicator of magnetic mineral concentration. The ratio of ARM to IRM is often used as a granulometric tool, where higher ratios suggest a higher fraction of fine-grained, low-coercivity minerals capable of carrying a stable remanence (Maher, 2011). Another grain-size-dependent parameter is the median destructive field of ARM and IRM demagnetization curves, where higher values suggest smaller average grain sizes (Maher, 2011).

The S-ratio is a parameter used to quantify the fraction of an IRM that is held by low-coercivity minerals. Bloemendal et al. (1992) defined the S-ratio as:

$$Sratio = \frac{1}{2}\left(\frac{IRM_{@1T} - IRM_{@0.3T}}{IRM_{@1T}}\right)$$

where values close to 1 indicate that minerals with coercivities <300 mT dominate the remanence, while lower values suggest increasing contributions from higher coercivity minerals. Also, the remanence held by the high-coercivity fraction is termed as the "hard-isothermal remanent magnetization" (HIRM) and is calculated by multiplying the complement of the S-ratio by the IRM_{1T} value (Maxbauer et al., 2016a).

Methods

Rock Magnetism Concentration Parameters

Rock magnetic measurements were performed on bulk specimens. Measurements of magnetic susceptibility (χ), NRM, ARM, and IRM were conducted in a magnetically shielded room with an ambient noise field less than 500 nT at the Laboratório de Paleomagnetismo at the Universidade de São Paulo (USPMag).

The magnetic susceptibility of each specimen was measured 10 times at low frequency (F1: 976 Hz) in a Kappabridge MFK1 by AGICO Ltd., United Kingdom. Remanence measurements were carried out using a 2G Enterprises superconducting rock magnetometer (RAPID) (noise level $<5 \times 10^{-12}$ Am^2). The IRM consisted of applying two different fields using a pulse magnetizer by 2G enterprise (model 2660). The pulse-field was applied along the *Z*-axis for all specimens in fields of 1,000 mT and a back-field of −300 mT. At least two measurements were carried out in the RAPID magnetometer at each step.

Unmixing of Magnetic Remanence

Analyses of the coercivity distribution are regularly applied in environmental magnetism studies to identify the different magnetic populations in natural sediments (Heslop, 2015; Roberts et al., 2019). The protocol for measuring ARM (incorporated into the RAPID system) was to apply a direct DC field of 0.03 mT superposed by an alternating field of 300 mT in the *Z*-axial coil at least two times, followed by a 300 mT demagnetization field in the quartz tube, and then an alternating field with 76 steps was performed, following a detailed stepwise demagnetization procedure (Egli, 2004a). The demagnetization of IRM was done in two of the four specimens for each stalagmite and followed the same steps as the ARM demagnetization (76 steps). Soil IRM intensities were close to the upper limit of the superconducting rock magnetometer ($>10^{-5}$ Am^2) causing higher standard deviations in the magnetization readings. For this reason, for these samples, we used the back-field IRM curves obtained in a vibrating sample magnetometer (VSM) by Princeton Measurements Corporation (model 3900) at the Institute for Rock Magnetism at the University of Minnesota. To comprehend the magnetic subpopulations and their differences in the varying latitudes and biomes, the skewed generalized Gaussian (SGG) functions were analyzed using the software MAX UnMix (Maxbauer et al., 2016b).

RESULTS

Rock Magnetism Concentration Parameters

Magnetic susceptibility was used to understand the contribution of different types of magnetic carriers in the karst system. The specimens were mass normalized, rather than volume normalized, to avoid issues arising from varying porosities. Speleothems and carbonates show similar low magnetic susceptibility values (**Figure 3**). These low values are due to the diamagnetic contribution from the calcite matrix and their low concentration of ferromagnetic material. The reference value of

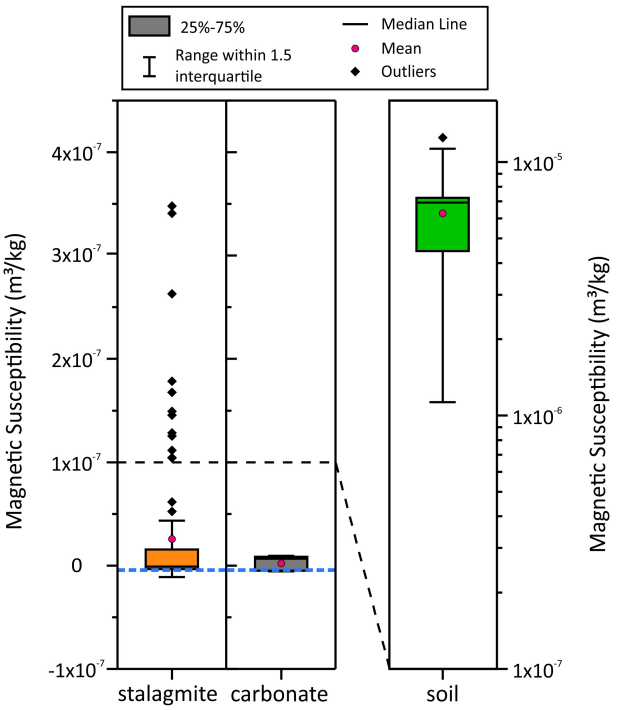

FIGURE 3 | Box plot of magnetic susceptibility results from stalagmite (orange), carbonate (gray), and soil (green); blue dashed line represents the pure calcite value (Schmidt et al., 2006).

susceptibility for pure calcite is -4.46×10^{-9} m^3/kg (Schmidt et al., 2006). The median value found for the stalagmites is $-2.00 \times 10^{-9} \pm 6.78 \times 10^{-8}$ m^3/kg, pointing to the calcite matrix. The median value for the carbonates is $6.71 \times 10^{-9} \pm 6.48 \times 10^{-9}$ m^3/kg. The soil has a magnetic susceptibility median value of $6.92 \times 10^{-6} \pm 3.12 \times 10^{-6}$ mł/kg, which is three to four orders of magnitude higher than that of calcite and carbonate (**Supplementary Table 1**).

The NRM, ARM, and IRM of all samples are shown in **Figure 4**. These results also indicate the contrast between the soil and the speleothems and the host carbonate, with lower median values for stalagmites NRM_{stal}: $1.10 \times 10^{-7} \pm 1.48 \times 10^{-5}$ Am^2/kg; ARM_{stal}: $1.61 \times 10^{-7} \pm 2.21 \times 10^{-5}$ Am^2/kg; IRM_{stal}: $7.48 \times 10^{-6} \pm 3.50 \times 10^{-4}$ Am^2/kg, a similar value for the carbonates NRM_{carb}: $1.60 \times 10^{-7} \pm 1.45 \times 10^{-7}$ Am^2/kg; ARM_{carb}: $3.07 \times 10^{-7} \pm 3.97 \times 10^{-7}$ Am^2/kg; IRM_{carb}: $2.93 \times 10^{-5} \pm 3.14 \times 10^{-5}$ Am^2/kg, and values of two to four orders of magnitude higher in the soil, with median values of NRM_{soil}: $1.22 \times 10^{-5} \pm 5.88 \times 10^{-5}$ Am^2/kg; ARM_{soil}: $2.11 \times 10^{-3} \pm 8.46 \times 10^{-4}$ Am^2/kg; IRM_{soil}: $2.52 \times 10^{-2} \pm 8.96 \times 10^{-3}$ Am^2/kg.

S-Ratio and HIRM

The distributions of S-ratio (**Figure 5**) show a distinctive grouping behavior when compared to the concentration parameters. Soil and speleothems show a predominance

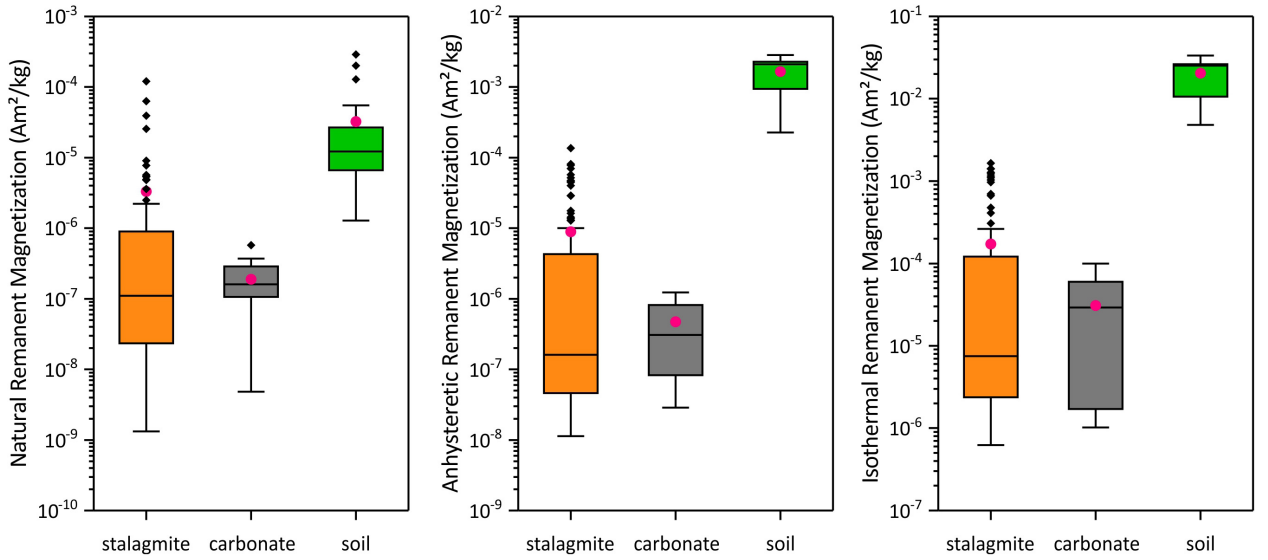

FIGURE 4 | Box plot of remanent magnetization of stalagmites (orange), carbonates (gray), and soil (green), for natural remanent magnetization (NRM), anhysteretic remanent magnetization (ARM), and isothermal remanent magnetization (IRM).

of low-coercivity phases (stalagmite with median S-ratio: 0.97 ± 0.07; soil with median S-ratio: 0.99 ± 0.01) and a high-coercivity contribution being more prominent in the carbonate (median S-ratio: 0.70 ± 0.15). The HIRM, that is, the concentration of high-coercivity minerals, shows that these minerals are present with median values for stalagmites $7.0 \times 10^{-6} \pm 1.9 \times 10^{-5}$ Am^2/kg, carbonates $1.0 \times 10^{-5} \pm 1.1 \times 10^{-5}$ Am^2/kg, and soil $2.7 \times 10^{-4} \pm 1.6 \times 10^{-4}$ Am^2/kg (**Figure 5**). Although for soil the values are higher in content than carbonate and speleothems, they only represent ∼1% of the total IRM@1T, whereas, for carbonates and stalagmites, they represent 30% and 3%, respectively, of the total IRM@1T.

Median Destructive Field of ARM and IRM

Demagnetization curves from stalagmites, carbonates, and soil indicate the presence of a low-coercivity magnetic phase in all specimens. Results from ARM have higher noise for stalagmites and carbonate due to the low-magnetization values close to the magnetometer noise level (5×10^{-12} Am^2), where only 63% of the stalagmite specimens could be analyzed. The IRM demagnetization curves also show the presence of a low-coercivity magnetic phase in all stalagmites and soil samples (**Supplementary Figure 6**). Conversely, the carbonates present higher coercivities.

Unmixing of the demagnetization curves of ARM and IRM was done using the MAX UnMix software (Maxbauer et al., 2016b), except when the noise dominates the signal. Only one component was fit for the whole dataset. Stalagmite and soil have similarly low values in coercivity (**Figure 6**) (stalagmite: MDF_{ARM}: 18.8 ± 1.1 mT; MDF_{IRM}: 20.3 ± 1.0 mT, soil: MDF_{ARM}: 17.7 ± 1.0 mT; MDF_{IRM}: 14.8 ± 1.0) and dispersion (stalagmite, DP_{ARM}: 0.29 ± 0.02; DP_{IRM}: 0.39 ± 0.02; soil: DP_{ARM}: 0.28 ± 0.01; DP_{IRM}: 0.37 ± 0.01). The carbonate has median values of MDF_{ARM}: 37.6 ± 1.1 mT; MDF_{IRM}: 32.2 ± 1.1 mT; DP_{ARM}: 0.37 ± 0.04; DP_{IRM}: 0.49 ± 0.03. The results obtained of the median coercivity from both ARM and IRM measurements (**Figures 6**, **7**) indicate that the magnetic signal of stalagmites is similar to that of the respective soil and contrasts with that of the host carbonate.

All speleothems irrespective of their location have coercivity values close to the detrital and pedogenic (plus extracellular) magnetite fields shown in **Figure 7**. The biplot of magnetic properties K_{ARM}/IRM by the median destructive field of ARM (MDF_{ARM}) also shows an agreement with fingerprint components: detrital pedogenic, detrital, detrital and extracellular magnetite, and pedogenic (DP, D, D+EX, and PD) (Egli, 2004b), supporting the soil-derived origin of the recorded magnetic signal. The results for carbonate data are not in agreement with the magnetic behavior of the speleothems and soil and are instead related to the magnetic mineral assemblage associated with their Neoproterozoic origin. Previous studies in stalagmites also found the same detrital/pedogenic magnetic component (Bourne et al., 2015; Jaqueto et al., 2016; Zhu et al., 2017), but they used median destructive field (ARM and IRM) and dispersion parameters instead of K_{ARM}/IRM. The K_{ARM}/IRM parameter was preferred instead of the dispersion parameter that does not have a clear physical meaning (Egli, 2004b).

Two Case Studies: Jaraguá and Lapa Dos Anjos Caves

Two sites containing stalagmite, carbonate, and soil samples were chosen to refine this analysis. Lapa dos Anjos cave (15.44°S, 44.40°W) and Jaraguá cave (21.09°S, 56.58°W) are both

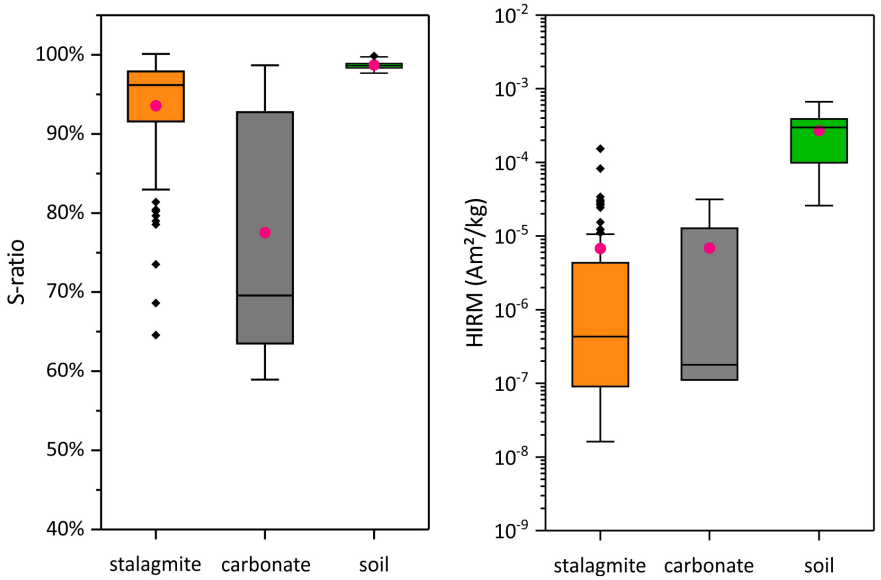

FIGURE 5 | Environmental magnetic parameters showing the fraction of remanence held by grains with coercivities <300 mT (S-ratio) and the remanence held by high-coercivity minerals (HIRM) for stalagmites (orange), carbonates (gray), and soil (green).

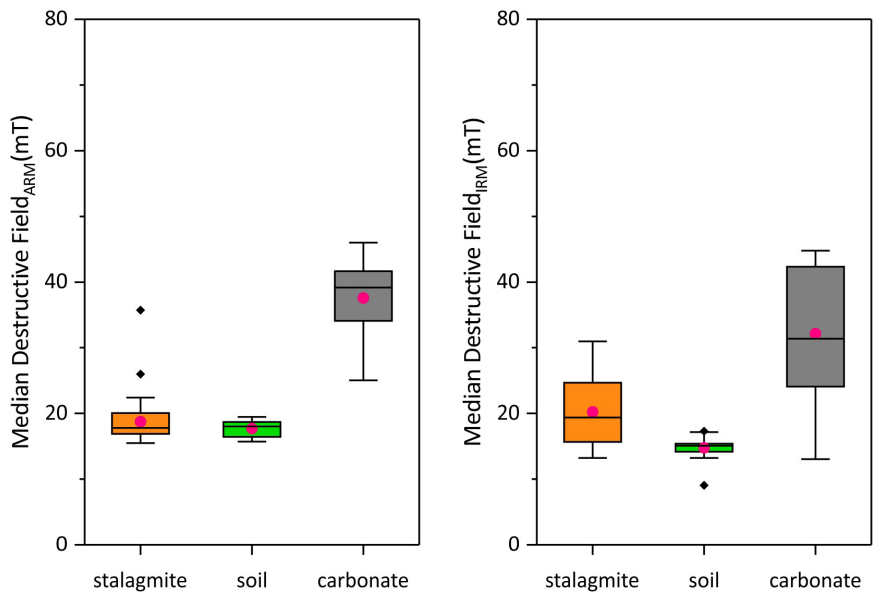

FIGURE 6 | Magnetic coercivity results from the adjustment of skewed generalized Gaussian (SGG) functions from the detailed demagnetization curves of ARM and IRM for stalagmites (orange), soil (green), and carbonates (gray).

located in the Cerrado biome. The average annual precipitation from 1979 to 2016 is 993.3 and 1402.7 mm/year, respectively (**Supplementary Figure 1**, Cerrado East#2 and Cerrado West #2). Both sites show a similar mean temperature of 23.0°C.

Stalagmites from both caves are considered "clean" (without "dirty" layers) (**Supplementary Figure 2**) and their median IRM values are 1.58×10^{-6} Am^2/kg (Lapa dos Anjos) and 3.20×10^{-6} Am^2/kg (Jaraguá cave) (**Figure 8**). Their host carbonates correspond to the Neoproterozoic formations of Sete Lagoas (Lapa dos Anjos) and Bocaina (Jaraguá cave), and their median IRM values are 5.06×10^{-5} Am^2/kg and 1.71×10^{-6} Am^2/kg, respectively. The soil has median IRM values of 2.59×10^{-2} Am^2/kg and 2.96×10^{-2} Am^2/kg, respectively. Stalagmites and soil at both sites show high S-ratios consistent with magnetic mineral assemblages dominated by low-coercivity phases, with median values of 0.98 and 0.99 for Lapa dos Anjos cave and 0.97 and 0.99 for Jaraguá cave, respectively (**Figure 8**). By comparison, the carbonates at each site show

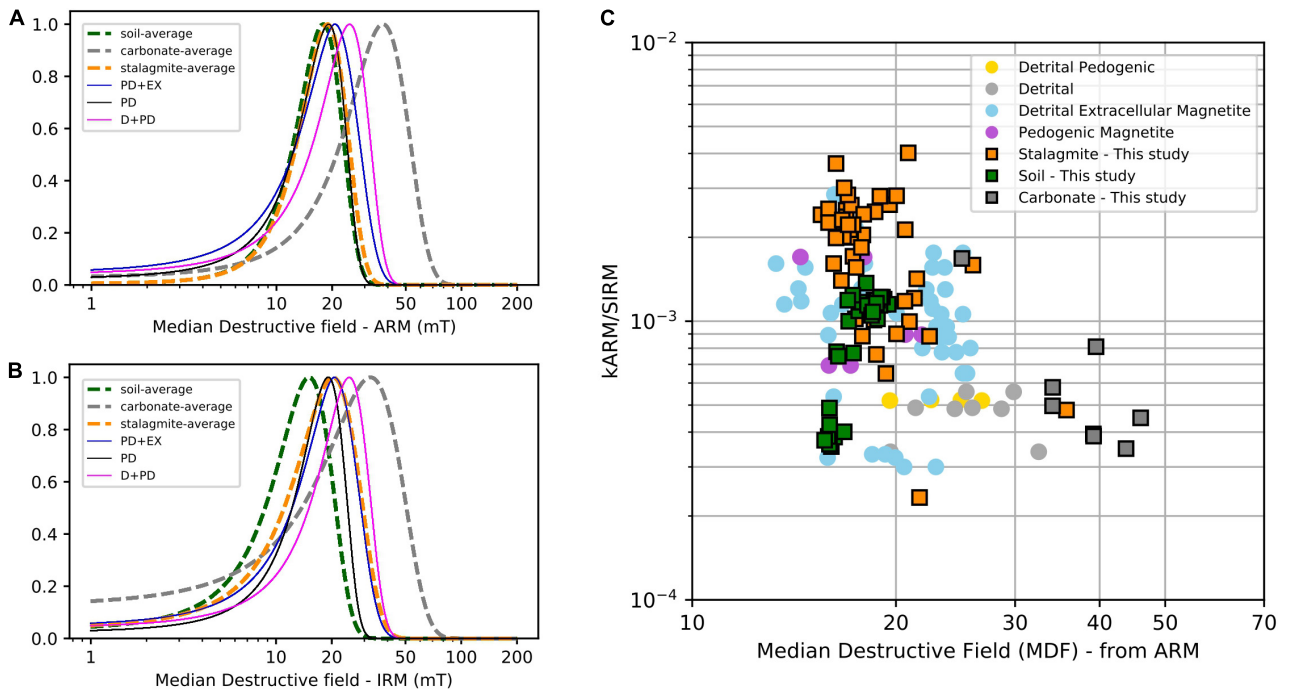

FIGURE 7 | (A) Average coercivity distribution of anhysteretic remanent magnetization (ARM) and **(B)** isothermal remanent magnetization (IRM) of stalagmite (dashed orange), soil (dashed green), and carbonate (dashed gray) obtained from skewed generalized Gaussian (SGG) function (Max UnMix). Reference values of pedogenic + extracellular magnetite (PD+EX) (blue), pedogenic (PD) (black), and detrital + pedogenic (pink) retrieved from the average values of ARM analysis by Egli (2004b). **(C)** Biplot of K_{ARM}/IRM and median destructive field (MDF) of ARM from stalagmites (orange squares), soil (green squares), and carbonate (gray squares). Magnetic properties taken from Egli (2004b) represent detrital pedogenic (yellow), detrital (light gray circles), detrital extracellular magnetite (light blue circles), and pedogenic magnetite (purple circles).

greater remanence contributions from high-coercivity minerals with S-ratios at Lapa dos Anjos of 0.64 and Jaraguá cave of 0.93.

The IRM demagnetization curves for stalagmites and soil yield lower median destructive fields, again showing the important role of lower coercivity minerals. The median MDF values for Lapa dos Anjos cave are 23.9 ± 3.1 mT and 15.1 ± 4.0 mT for stalagmites and soil, and for Jaraguá cave, the median MDF values are 19.7 ± 3.2 mT and 15.7 ± 1.3 mT. In contrast, the carbonate bedrocks for Lapa dos Anjos and Jaraguá caves have median MDF values of 43.4 ± 2.1 mT and 24.2 ± 5.9 mT, respectively (**Figure 8**). The coercivity values for stalagmite and soil from both caves have their magnetic properties in the same cluster as detrital, detrital pedogenic, and detrital extracellular magnetite (**Figure 7**). These results indicate that the dominant magnetic minerals in tropical stalagmites are mainly derived from overlying soils. Although magnetic minerals from host carbonate may be present, overall they have a low contribution to the magnetic signal.

MAGNETIC PARAMETERS AND BIOMES

Spearman's Rank Correlation

To compare the results obtained within the database, we calculated the Spearman's rank correlation coefficients for 54 stalagmites specimens where IRM demagnetization was performed. The following magnetic properties (see section "Rock Magnetic Parameters") were considered in the analysis: concentration parameters (magnetic susceptibility, NRM, ARM, and IRM), composition parameter (S-ratio), and granulometry parameters (χ_{ARM}/SIRM and MDF_{IRM}) (**Figure 9**). Spearman's correlation is recommended to avoid a linear relationship since most magnetic parameters have non-Gaussian distributions (Hu et al., 2019).

In the speleothems, a strong correlation (>0.84) is found among the magnetic concentration parameters (susceptibility, NRM, ARM, and IRM) (**Figure 9**). This result supports the idea that the different magnetic concentration parameters in **Table 1** are essentially recording the same signal, with a predominance of ultrafine magnetite/maghemite in (sub-)tropical karst system. The strong correlation found using diverse rock magnetic parameters that respond differently to concentration, granulometry, types of magnetization, and magnetic mineralogy (see section "Rock Magnetic Parameters") shows that previous interpretations of the pedogenic origin of magnetic grains prevail tropical in karst systems and can be used to interpret local soil dynamics and rainfall regimes (Jaqueto et al., 2016; Fu et al., 2021).

The proportion of low-coercivity minerals indicated by S-ratio have a weak correlation coefficient (0.16–0.25) with magnetic concentration parameters. Antiferromagnetic minerals have been previously reported in stalagmites, mainly goethite and hematite

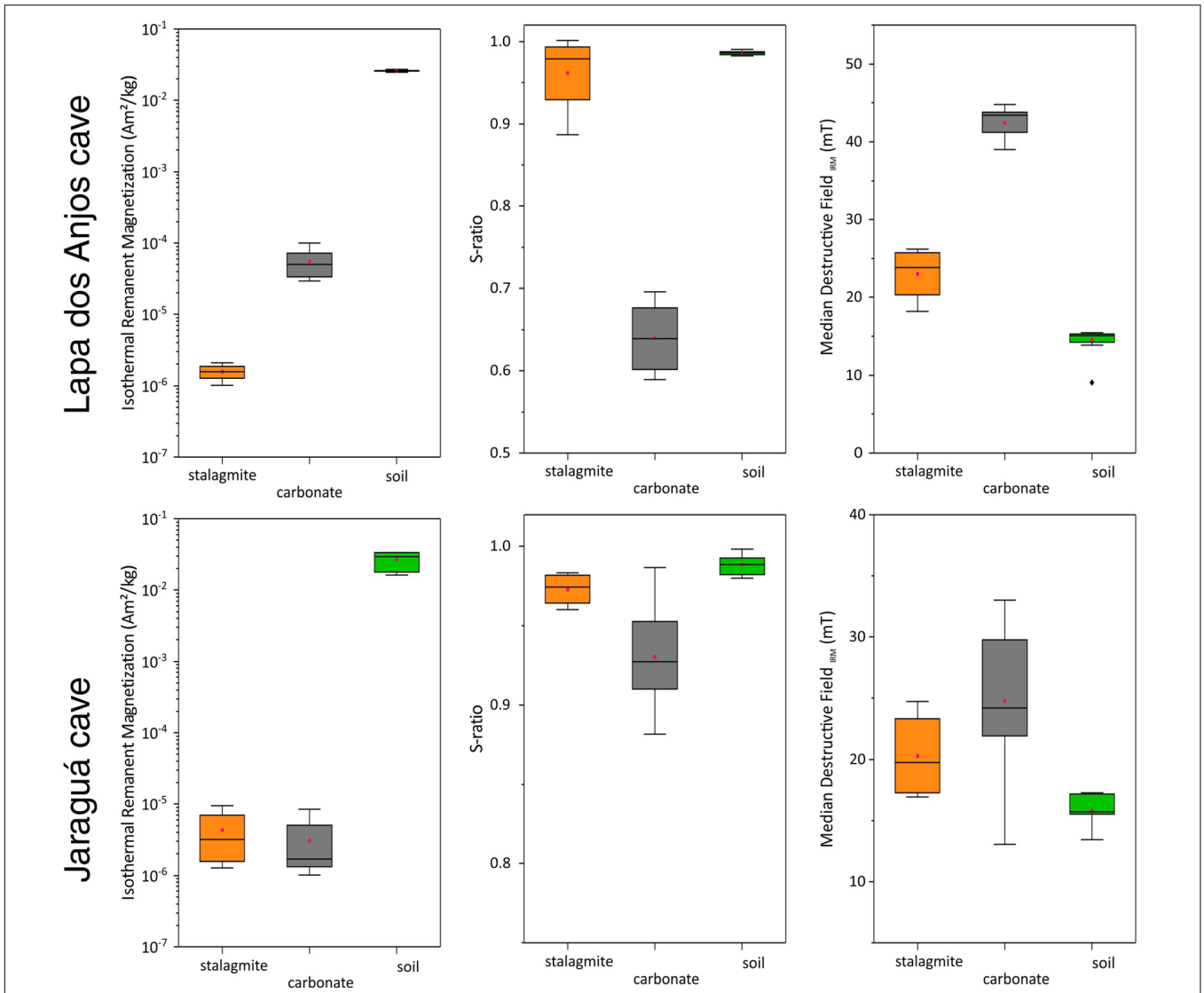

FIGURE 8 | Magnetic properties of the caves: Lapa dos Anjos (upper) and Jaraguá (bottom). (*First column*) Isothermal remanence magnetization (IRM) after a pulse-field of 1T. (*Second column*) S-ratio shows the presence of the low-coercivity phase. (*Third column*) Median destructive field from IRM demagnetization. The box-plot are referred to stalagmites (orange), soil (green), and carbonates (gray).

(Lascu and Feinberg, 2011; Strauss et al., 2013; Font et al., 2014); this positive weak correlation with S-ratio could indicate that the concentration parameters favor the input of low-coercivity minerals (magnetite and maghemite), and the changes observed in concentration parameters can be associated with a detrital concentration in drip water, instead of changes in mineralogy. So, changes in mineralogy tracked by S-ratio that correlate with magnetic concentration parameters would mean more complex dynamics in the karst system with changes of the dominant magnetic mineral phase, which is not found in (sub-)tropical regimes.

Coercivity parameters (MDF_{IRM}) have a strong negative correlation (0.71–0.78) with magnetic concentration parameters (**Figure 9**). This could indicate a better selection of magnetic mineral grain size and/or changes in soil oxidation reaction (Ge et al., 2014). This is also evidenced by a negative moderate correlation (−0.41) with S-ratio, where a high coercivity could mean the presence of weathering (carbonate), detrital flood grains, and hematite (stable "old" soils). Granulometry parameter (χ_{ARM}/SIRM) has a moderate negative correlation with MDF_{IRM} (−0.65) and could be related to magnetic interaction between grains (Egli and Lowrie, 2002).

The Influence of Biomes on Magnetic Mineral Formation

Biomes are defined by climate, leaf structure, leaf type, and plant spacing (Fairchild and Baker, 2012). In karst systems, the most common soils are Rendzina soils, with a characteristic of few centimeters and with relatively permeable bedrock, which

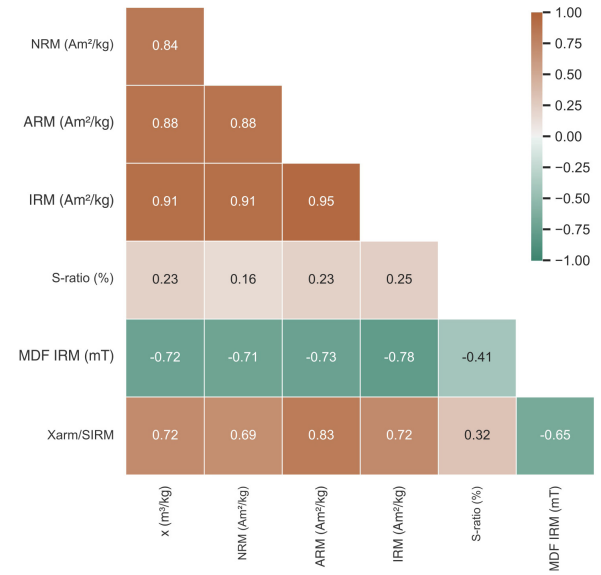

FIGURE 9 | Spearman's rank correlation of magnetic properties of speleothems [susceptibility, natural remanent magnetization (NRM), anhysteretic remanent magnetization (ARM), isothermal remanent magnetization (IRM), S-ratio, median coercivity field of IRM, and susceptibility of ARM by IRM].

allows the free drainage of soil profiles and anaerobic conditions. So, we grouped the samples by their biomes (**Figure 2** and **Supplementary Figure 1**) (Olson et al., 2001), compared with a magnetic concentration parameter (IRM) and coercivity to test for any correlation with different biomes (**Figure 10**). We chose these parameters based on the correlation between concentration parameters and coercivity due to their similarity with soil values.

The results from IRM grouped by biome (**Figure 10**) show a lower concentration in the Amazon, Atlantic, and Caatinga biome, and higher concentrations and higher dispersions for the Cerrado biome. The coercivity values show a higher value for Amazon, Atlantic, and Caatinga biomes and lower values for Cerrado. Interestingly, these results are exactly consistent with the soil study of Maxbauer et al. (2017), which examined the magnetic properties of modern soils as a function of grassland (savannah) and forest biomes in mid-latitude Minnesota. The coherence observed between speleothem coercivity and IRM with the biomes may simply be a further expression of the close relationship between pedogenic processes at the surface and incorporation of pedogenic minerals into underlying karst features. Thus, in tropical settings such as Brazil, the magnetic mineral assemblages in speleothem may best be interpreted within the context of pedogenic processes.

- Cerrado biome (savannah shrubland): High concentration of magnetic minerals (median IRM of 1.40×10^{-4} Am^2/kg) and low coercivity (median MDF_{IRM} ~18.4 mT) suggest a greater flux of magnetic minerals from the epikarst than other biomes.
- Caatinga (dry forest): Higher coercivity (median MDF_{IRM} ~24.4 mT) observed may be indicative of maghemitization (partial oxidation of magnetite) (Ozdemir and Dunlop, 2010) due to fewer dry/wet cycles, thereby inhibiting magnetic enhancement. Lower magnetic mineral concentrations are observed (median IRM of $\sim 7.17 \times 10^{-6}$ Am^2/kg).
- Amazon and Atlantic biomes (moist broadleaf forest): Lower IRM values (median IRM of $\sim 4.28 \times 10^{-6}$ Am^2/kg and $\sim 5.05 \times 10^{-6}$ Am^2/kg, respectively) compared to Cerrado and higher coercivity values (median MDF_{IRM} ~27.7 mT and 23.9 mT, respectively) are observed. Two processes may explain this behavior: Enhanced maghemitization may increase the coercivity, while the prevalence of waterlogged soils and the concomitant dissolution of magnetic minerals could lower their

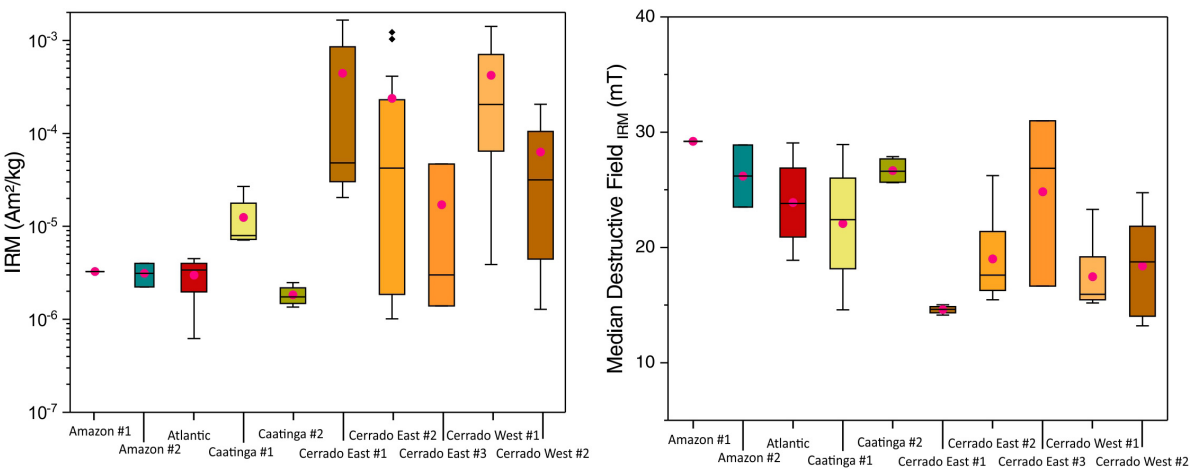

FIGURE 10 | Magnetic properties of the stalagmites organized by their respective biomes. (Left) Isothermal remanent magnetization and biomes. (Right) Median destructive field adjusted from IRM demagnetization curve and its values by each biome. Amazon biome (green), Atlantic biome (red), Caatinga biome (yellow), and Cerrado biome (orange).

concentration and diminish the transport of magnetic minerals to the cave system.

SUMMARY AND CONCLUSION

This study presents a database of stalagmite magnetic properties, including parameters related to magnetic mineral composition and concentration and grain size. In two instances, we compared these values to those of the overlying soil and host carbonate. These results expand our knowledge of speleothem magnetic properties in tropical-subtropical regimes far beyond what could be achieved through the examination of one or more speleothems from a single cave. Additionally, this database provides robust evidence that the main magnetic component in Brazilian stalagmites is derived from soils overlying karst systems and that processes affecting pedogenic enhancement are reflected in these speleothems. The presence of low-coercivity magnetic minerals is pervasive across different latitudes and biomes. Median destruction field values from the demagnetization of IRMs show similarities between stalagmites and soil, whereas host carbonates showed consistently higher values. The fraction of remanence held by low-coercivity magnetic minerals as observed via the S-ratio ($>90\%$) also shows this relationship.

Statistical analysis of stalagmite magnetic properties using Spearman's correlation shows a high correlation among rock magnetism concentration parameters (susceptibility, NRM, ARM, and IRM). Thus, although different parameters have been reported in the literature, they are essentially recording the same phenomena within (sub-) tropical zones. The weak correlation between magnetic concentration values with coercivity values shows that changes in mineralogy are not the main control in the karst system.

When compared within the four different biomes, the Cerrado biomes have a high concentration of magnetic minerals with coercivity values $\sim$18.4 mT, whereas Caatinga, Amazon, and Atlantic biomes have a lower concentration of magnetic minerals and higher coercivity values of 24.4, 27.7, and 23.9 mT, respectively. This result is consistent with known trends in pedogenic processes and provides further evidence for the important role of pedogenic magnetite in Brazilian speleothems.

Future research on the fine-scale magnetic processes in karst systems would benefit from in-depth studies of soil profiles, constraining the physical and microbiological properties and periodically monitoring underlying caves, as is often done for oxygen and carbon isotope studies. This approach would allow researchers to explore how the flux of magnetic particles into cave environments varies with time and season across multiple biomes.

DATA AVAILABILITY STATEMENT

The original contributions presented in the study are included in the article/**Supplementary Material**, further inquiries can be directed to the corresponding author/s.

AUTHOR CONTRIBUTIONS

PJ, RT, JMF, VN, NS, FC, and IK conceived and planned the experiments. PJ performed the measurements. PJ, RT, JMF, JC, VN, and NS performed the analysis, drafted the manuscript, and designed the figures. MS and NS helped in climate series data and interpretation. FC and IK supervised the project. All authors contributed to the article and approved the submitted version.

FUNDING

This work was supported by the São Paulo Research Foundation (grant numbers: 2016/24870-2, 2016/15807-5, 2017/50085-3, 2018/15774-5, and 2019/06709-8) and the National Council for Scientific and Technological Development (CNPq) (grant numbers: 423573/2018-7 and 308769/2018-0 to NS). This work was also supported by the Serrapilheira Institute (grant number: Serra-1812-27990). This work was funded by National Science Foundation grant EAR-2044535 and US-Israel Binational Science Foundation grant #2016402 to JMF. IRM was supported by the US National Science Foundation.

ACKNOWLEDGMENTS

We are grateful to Instituto Brasileiro do Meio Ambiente e dos Recursos Naturais Renováveis for providing permission to collect stalagmite samples. We are also very thankful for the constructive comments of the reviewers and editor.

SUPPLEMENTARY MATERIAL

The Supplementary Material for this article can be found online at: https://www.frontiersin.org/articles/10.3389/feart.2021.634482/full#supplementary-material

REFERENCES

Bloemendal, J., King, J. W., Hall, F. R., and Doh, S. J. (1992). Rock magnetism of late Neogene and Pleistocene deep-sea sediments-relationship to sediment source, diagenetic processes, and sediment lithology. *J. Geophys. Res. Solid Earth* 97, 4361–4375. doi: 10.1029/91jb03068

Bosch, R. F., and White, W. B. (2004). *Lithofacies and Transport of Clastic Sediments in Karstic Aquifers*. Boston, MA: Springer, 1–22.

Bourne, M. D., Feinberg, J. M., Strauss, B. E., Hardt, B., Cheng, H., Rowe, H. D., et al. (2015). Long-term changes in precipitation recorded by magnetic minerals in speleothems. *Geology* 43, 595–598. doi: 10.1130/g36695.1

Campos, J., Cruz, F. W., Ambrizzi, T., Deininger, M., Vuille, M., Novello, V. F., et al. (2019). Coherent south american monsoon variability during the last millennium revealed through high-resolution proxy records. *Geophys. Res. Lett.* 46, 8261–8270. doi: 10.1029/2019gl082513

Chen, Q., Zhang, T. W., Wang, Y. T., Zhao, J. X., Feng, Y. X., Liao, W., et al. (2019). Magnetism signals in a stalagmite from Southern China and Reconstruction of paleorainfall during the interglacial-glacial transition. *Geophys. Res. Lett.* 46, 6918–6925. doi: 10.1029/2019gl082204

Cruz, F. W., Burns, S. J., Karmann, I., Sharp, W. D., Vuille, M., Cardoso, A. O., et al. (2005). Insolation-driven changes in atmospheric circulation over the past 116,000 years in subtropical Brazil. *Nature* 434, 63–66.

Dreybrodt, W. (1999). Chemical kinetics, speleothem growth and climate. *Boreas* 28, 347–356. doi: 10.1080/03009489942073

Dreybrodt, W., Eisenlohr, L., Madry, B., and Ringer, S. (1997). Precipitation kinetics of calcite in the system CaCO3-H2O-CO2: the conversion to CO2 by the slow process H++HCO3−>CO2+H2O as a rate limiting step. *Geochim. Cosmochim. Acta* 61, 3897–3904. doi: 10.1016/s0016-7037(97)00201-9

Dreybrodt, W., and Scholz, D. (2011). Climatic dependence of stable carbon and oxygen isotope signals recorded in speleothems: from soil water to speleothem calcite. *Geochim. Cosmochim. Acta* 75, 734–752. doi: 10.1016/j.gca.2010.11.002

Egli, R. (2004a). Characterization of individual rock magnetic components by analysis of remanence curves, 1. Unmixing natural sediments. *Studia Geophys. Geodaetica* 48, 391–446. doi: 10.1023/b:sgeg.0000020839.45304.6d

Egli, R. (2004b). Characterization of individual rock magnetic components by analysis of remanence curves. 2. Fundamental properties of coercivity distributions. *Phys. Chem. Earth* 29, 851–867. doi: 10.1016/s1474-7065(04)00129-9

Egli, R., and Lowrie, W. (2002). Anhysteretic remanent magnetization of fine magnetic particles. *J. Geophys. Res. Solid Earth* 107, 21.

Evans, M., and Heller, F. (2003). *Environmental Magnetism: Principles and Applications of Enviromagnetics*. Amsterdam: Elsevier.

Fairchild, I. J., and Baker, A. (2012). *Speleothem Science : From Process to Past Environments*. Hoboken, NJ: Wiley.

Fairchild, I. J., Smith, C. L., Baker, A., Fuller, L., Spotl, C., Mattey, D., et al. (2006). Modification and preservation of environmental signals in speleothems. *Earth Sci. Rev.* 75, 105–153. doi: 10.1016/j.earscirev.2005.08.003

Feinberg, J. M., Lascu, I., Lima, E. A., Weiss, B. P., Dorale, J. A., Alexander, E. C., et al. (2020). Magnetic detection of paleoflood layers in stalagmites and implications for historical land use changes. *Earth Planet. Sci. Lett.* 530:115946. doi: 10.1016/j.epsl.2019.115946

Font, E., Veiga-Pires, C., Pozo, M., Carvallo, C., Neto, A. C. D., Camps, P., et al. (2014). Magnetic fingerprint of southern Portuguese speleothems and implications for paleomagnetism and environmental magnetism. *J. Geophys. Res. Solid Earth* 119, 7993–8020. doi: 10.1002/2014jb011381

Fu, R. R., Hess, K., Jaqueto, P., Novello, V. F., Kukla, T., Trindade, R. I. F., et al. (2021). High-resolution environmental magnetism using the quantum diamond microscope (QDM): application to a tropical speleothem. *Front. Earth Sci.* 8:674.

Garreaud, R. D., Vuille, M., Compagnucci, R., and Marengo, J. (2009). Present-day South American climate. *Palaeogeogr. Palaeoclimatol. Palaeoecol.* 281, 180–195. doi: 10.1016/j.palaeo.2007.10.032

Ge, K. P., Williams, W., Liu, Q. S., and Yu, Y. (2014). Effects of the core-shell structure on the magnetic properties of partially oxidized magnetite grains: experimental and micromagnetic investigations. *Geochem. Geophys. Geosyst.* 15, 2021–2038. doi: 10.1002/2014gc005265

Hartmann, A., and Baker, A. (2017). Modelling karst vadose zone hydrology and its relevance for paleoclimate reconstruction. *Earth Sci. Rev.* 172, 178–192. doi: 10.1016/j.earscirev.2017.08.001

Heslop, D. (2015). Numerical strategies for magnetic mineral unmixing. *Earth Sci. Rev.* 150, 256–284. doi: 10.1016/j.earscirev.2015.07.007

Hu, P., Heslop, D., Viscarra Rossel, R. A., Roberts, A. P., and Zhao, X. (2019). Continental-scale magnetic properties of surficial Australian soils. *Earth Sci. Rev.* 203:103028. doi: 10.1016/j.earscirev.2019.103028

Jaqueto, P., Trindade, R. I. F., Hartmann, G. A., Novello, V. F., Cruz, F. W., Karmann, I., et al. (2016). Linking speleothem and soil magnetism in the Pau d'Alho cave (central South America). *J. Geophys. Res. Solid Earth* 121, 7024–7039. doi: 10.1002/2016jb013541

Jordanova, N. (2017). *Soil Magnetism: Applications in Pedology, Environmental Science and Agriculture*. Cambridge, MA: Academic Press, 1–445.

Lascu, I., and Feinberg, J. M. (2011). Speleothem magnetism. *Quat. Sci. Rev.* 30, 3306–3320. doi: 10.1016/j.quascirev.2011.08.004

Lascu, I., Feinberg, J. M., Dorale, J. A., Cheng, H., and Edwards, R. L. (2016). Age of the Laschamp excursion determined by U-Th dating of a speleothem geomagnetic record from North America. *Geology* 44, 139–142. doi: 10.1130/g37490.1

Maher, B. A. (2011). The magnetic properties of Quaternary aeolian dusts and sediments, and their palaeoclimatic significance. *Aeolian Res.* 3, 87–144. doi: 10.1016/j.aeolia.2011.01.005

Maxbauer, D. P., Feinberg, J. M., and Fox, D. L. (2016a). Magnetic mineral assemblages in gills and paleosols as the basis for paleoprecipitation proxies: a review of magnetic methods and challenges. *Earth Sci. Rev.* 155, 28–48. doi: 10.1016/j.earscirev.2016.01.014

Maxbauer, D. P., Feinberg, J. M., and Fox, D. L. (2016b). MAX UnMix: a web application for unmixing magnetic coercivity distributions. *Comput. Geosci.* 95, 140–145. doi: 10.1016/j.cageo.2016.07.009

Maxbauer, D. P., Feinberg, J. M., Fox, D. L., and Nater, E. A. (2017). Response of pedogenic magnetite to changing vegetation in soils developed under uniform climate, topography, and parent material. *Sci. Rep.* 7:10.

Novello, V. F., Vuille, M., Cruz, F. W., Strkís, N. M., de Paula, M. S., Edwards, R. L., et al. (2016). Centennial-scale solar forcing of the South American Monsoon System recorded in stalagmites. *Sci. Rep.* 6:24762. doi: 10.1038/srep24762

Olson, D. M., Dinerstein, E., Wikramanayake, E. D., Burgess, N. D., Powell, G. V. N., Underwood, E. C., et al. (2001). Terrestrial ecoregions of the worlds: a new map of life on Earth. *Bioscience* 51, 933–938. doi: 10.1641/0006-3568(2001)051[0933:teotwa]2.0.co;2

Ozdemir, O., and Dunlop, D. J. (2010). Hallmarks of maghemitization in low-temperature remanence cycling of partially oxidized magnetite nanoparticles. *J. Geophys. Res. Solid Earth* 115:B02101.

Perkins, A. M. (1996). Observations under electron microscopy of magnetic minerals extracted from speleothems. *Earth Planet. Sci. Lett.* 139, 281–289. doi: 10.1016/0012-821x(96)00013-1

Regattieri, E., Zanchetta, G., Isola, I., Zanella, E., Drysdale, R. N., Hellstrom, J. C., et al. (2019). Holocene Critical Zone dynamics in an Alpine catchment inferred from a speleothem multiproxy record: disentangling climate and human influences. *Sci. Rep.* 9:17829.

Ribeiro, J., Sano, S., Macedo, J., and da Silva, J. (1983). *Os Principais Tipos Fisionômicos da Região Dos Cerrados*, Vol. 21. Planaltina: Boletim de Pesquisa, EMBRAPA/CPAC.

Roberts, A. P., Hu, P. X., Harrison, R. J., Heslop, D., Muxworthy, A. R., Oda, H., et al. (2019). Domain state diagnosis in rock magnetism: evaluation of potential alternatives to the day diagram. *J. Geophys. Res. Solid Earth* 124, 5286–5314. doi: 10.1029/2018jb017049

Rochette, P., Mathe, P. E., Esteban, L., Rakoto, H., Bouchez, J. L., Liu, Q. S., et al. (2005). Non-saturation of the defect moment of goethite and fine-grained hematite up to 57 Teslas. *Geophys. Res. Lett.* 32: L22309.

Schmidt, V., Gunther, D., and Hirt, A. M. (2006). Magnetic anisotropy of calcite at room-temperature. *Tectonophysics* 418, 63–73. doi: 10.1016/j.tecto.2005.12.019

Strauss, B. E., Strehlau, J. H., Lascu, I., Dorale, J. A., Penn, R. L., and Feinberg, J. M. (2013). The origin of magnetic remanence in stalagmites: observations from electron microscopy and rock magnetism. *Geochem. Geophys. Geosyst.* 14, 5006–5025. doi: 10.1002/2013gc004950

Trindade, R. I. F., Jaqueto, P., Terra-Nova, F., Brandt, D., Hartmann, G. A., Feinberg, J. M., et al. (2018). Speleothem record of geomagnetic South Atlantic Anomaly recurrence. *Proc. Natl. Acad. Sci. U.S.A.* 115, 13198–13203. doi: 10.1073/pnas.1809197115

Whitmore, T. C., and Prance, G. T. (1987). *Biogeography and Quaternary History in Tropical America*. Oxford: Clarendon Press.

Xie, S. C., Evershed, R. P., Huang, X. Y., Zhu, Z. M., Pancost, R. D., Meyers, P. A., et al. (2013). Concordant monsoon-driven postglacial hydrological changes in

peat and stalagmite records and their impacts on prehistoric cultures in central China. *Geology* 41, 827–830. doi: 10.1130/g34318.1

Zanella, E., Tema, E., Lanci, L., Regattieri, E., Isola, I., Hellstrom, J. C., et al. (2018). A 10,000 yr record of high-resolution paleosecular variation from a flowstone of Rio Martino Cave, Northwestern Alps, Italy. *Earth Planet. Sci. Lett.* 485, 32–42. doi: 10.1016/j.epsl.2017.12.047

Zhu, Z. M., Feinberg, J. M., Xie, S. C., Bourne, M. D., Huang, C. J., Hu, C. Y., et al. (2017). Holocene ENSO-related cyclic storms recorded by magnetic minerals in speleothems of central China. *Proc. Natl. Acad. Sci. U.S.A.* 114, 852–857. doi: 10.1073/pnas.1610930114

Conflict of Interest: The authors declare that the research was conducted in the absence of any commercial or financial relationships that could be construed as a potential conflict of interest.

Advantages of publishing in Frontiers

OPEN ACCESS
Articles are free to read for greatest visibility and readership

FAST PUBLICATION
Around 90 days from submission to decision

HIGH QUALITY PEER-REVIEW
Rigorous, collaborative, and constructive peer-review

TRANSPARENT PEER-REVIEW
Editors and reviewers acknowledged by name on published articles

Frontiers
Avenue du Tribunal-Fédéral 34
1005 Lausanne | Switzerland

Visit us: www.frontiersin.org
Contact us: frontiersin.org/about/contact

REPRODUCIBILITY OF RESEARCH
Support open data and methods to enhance research reproducibility

DIGITAL PUBLISHING
Articles designed for optimal readership across devices

FOLLOW US
@frontiersin

IMPACT METRICS
Advanced article metrics track visibility across digital media

EXTENSIVE PROMOTION
Marketing and promotion of impactful research

LOOP RESEARCH NETWORK
Our network increases your article's readership